Monsoonal Precipitation in a Model Hierarchy: Impact of Continental Geometry and Global Warming

Thesis by
Katrina Lynn Hui

In Partial Fulfillment of the Requirements for the
Degree of
Environmental Science and Engineering

CALIFORNIA INSTITUTE OF TECHNOLOGY
Pasadena, California

2022
Defended March 14, 2022

Katrina Lynn Hui
ORCID: 0000-0003-0325-8800

ACKNOWLEDGEMENTS

This thesis would not be possible without the love, support, and guidance of my family, advisors, and friends.

I want to start with thanking my advisor Simona Bordoni. Over the years, she has been a wonderful advisor and role model. From the beginning, she spent lots of time meeting with me, and continued to do so even eventually from nine time zones away. Her guidance and our discussions helped me develop my curiosity and love for the tropics and I will always be grateful for her encouragement and advice in both research and life. She supported me to attend conferences and summer schools, where I learned so much and made great friends, initially in the field, and now for life. I will always cherish the time she hosted me with her family in Italy and we could discuss research, food, and soccer all at once. I really enjoy working with her and am lucky to have her as an advisor and friend.

I also want to thank my committee members, Tapio Schneider, Andy Thompson, and Hui Su. Their support has encouraged me through the difficult times of my PhD. Especially since my advisor moved, they have been so welcoming and generous, inviting me to participate in their group meetings, retreats, and events. I especially want to thank Tapio for advising my second project my first year and always helping me with any applications. I really enjoyed working together on research and as your TA.

Thank you to all the fellow ESE and GPS students I've had the pleasure to share time with over the years. I want to thank Giuliana for being an amazing friend since day one. You have always been there with me through all the fun and stressful times. I also thank the other older students in Simona, Tapio, and Andy's groups, Hso-Hsuan, Sally, Xiaozhou, and Zach. First as my TAs, then eventually office mates and colleagues, I'm thankful for your helpful and fun interactions and am proud I got to be a part of 226.

I am very fortunate to have entered the department with a great cohort, Stacy, Vasilije, Ollie, Steve, and Nicole. I want to thank them for making what could have been a stressful first year so much fun. I also want to thank the younger ESE students who always keep things interesting. I especially want to thank Costa. From doing 12.800 problem sets in our dorm, to nights out in Hollywood, I want to thank you for years of friendship. When I was finding a new direction in undergrad, your

friendship was invaluable and I am grateful we ended up in the same department again.

Along the way, I have also received support from many helpful postdocs and scientists. Thank you Spencer, Zhaoyi, Lenka, Colleen, Yair, and Anna for interesting and helpful discussions. I especially want to thank Kyle for helping me set up and run the PyCLES model for my first year project with Tapio and always being available to help me understand cloud dynamics, as confusing as they can be sometimes.

I also want to thank my friend Jane, with whom I am grateful to share many wonderful summer school and conference memories together and who introduced me to many friends in the field.

Besides the people in my department, I want to thank the many friends I have made at Caltech. My time here would not have been the same without you. I thank my girls from Ninita for all the brunch memories. I want to thank Jeremy for many shared laughs. I thank Alessio, Steve, and Leo, for all the surfing, beach, and camping adventures over the years. Thank you also to Will for introducing me to techno and Kayleigh and Dalila for the all the fun times out in LA. I especially want to thank Sarah for her friendship over the years. She is always supporting and encouraging me.

I am extremely lucky to have met Olmo during our time at Caltech. The past couple years have been a wonderful adventure together. I thank you for many things, for your humor, your energy, your patience. But most of all, I thank you for always believing in me and encouraging me to be and do my best.

Most importantly, I want to thank my parents. I thank my dad for always being my cheerleader and getting excited about all my endeavours. His excitement and support inspire me to keep striving for my goals everyday. Finally, I want to thank my mom. She is the best mom and role model anyone could ask for. She instilled in me a confidence and belief in myself that I can do whatever I put my mind to, and for that I am forever grateful. It has been a special journey to do my PhD in your field, and I am so grateful that we can share this special bond. Thank you for your constant support and encouragement through all the times, high and low. Thank you for inspiring me everyday.

ABSTRACT

Monsoon systems around the world vary in their onset timing and precipitation spatial extent, suggesting that continental geometry could play an important role in differentiating between different monsoons systems. Since over half the world's population is dependent on monsoonal precipitation, it is of crucial importance to understand what controls the strength, seasonal evolution, and spatial extent of the tropical circulation and its associated precipitation and how they will evolve in a warmer climate. Recent studies suggest that individual monsoon regions will respond differently to climate change, highlighting the potential influence continental geometry may have on the current and future monsoon. In this thesis, we study the response of monsoonal precipitation, in its precipitation intensity, pattern, and onset timing, to idealized continent and climate change using a model hierarchy. By progressively building up complexity, we can gain insight from the idealized cases to determine responsible mechanisms in the responses to warming found in individual monsoon regions within the full general circulation models (GCMs).

First, we study the influence of continental geometry on the timing and spatial distribution of monsoonal precipitation under our current climate using an idealized aquaplanet model run with different zonally symmetric configurations of Northern Hemispheric land. We show that having continent extending to the tropical latitudes is necessary to generate monsoons that feature a rapid migration of the convergence zone over the continent, similar to observed monsoons. Without these regions, the tropical circulation is not able to rapidly transition into an angular momentum conserving monsoon regime. Next, we focus only on the effect of climate warming on the monsoon by using a set of idealized aquaplanet simulations with uniform mixed-layer depth, run with different atmospheric longwave optical depths to simulate a large range of both colder and warmer climates than the current climate. We show that as the climate warms, during the spring the atmospheric energy storage increases, which compensates the thermal forcing and allows for the tropical circulation transitions to be delayed, resulting in a delay in monsoon onset. Furthermore, we find that in extremely warm climates, the compensating effect of the energy storage is limited due to complex changes in the surface temperature seasonality. As a result, eventually the monsoon onset delay with warming saturates. These results highlight the important role the surface, both in its physical conditions and energy balance, has on setting the monsoon.

PUBLISHED CONTENT AND CONTRIBUTIONS

Hui, K. L., & Bordoni, S. (2022). *Response of monsoon onset timing to greenhouse warming in an idealized GCM* [preprint].
Both authors participated in the conception of the project and the writing of the manuscript. Simona Bordoni ran the idealized simulations and Katrina Hui conducted the analysis of the model output.

Hui, K. L., & Bordoni, S. (2021). Response of monsoon rainfall to changes in the latitude of the equatorward coastline of a zonally symmetric continent. *Journal of the Atmospheric Sciences*, *78*(5), 1429–1444. https://doi.org/10.1175/JAS-D-20-0110.1.
Both authors participated in the conception of the project and the writing of the manuscript. Katrina Hui ran the idealized simulations and conducted the analysis of the model output.

Geen, R., Bordoni, S., Battisti, D. S., & Hui, K. L. (2020). Monsoons, ITCZs, and the concept of the global monsoon [e2020RG000700 10.1029/2020RG000700]. *Reviews of Geophysics*, *58*(4), e2020RG000700. https://doi.org/https://doi.org/10.1029/2020RG000700.
Katrina Hui ran the aquaplanet simulations including idealized continent using the Caltech Flexible Modeling System GCM and provided figures for the section of the review paper covering monsoons within idealized GCMs.

TABLE OF CONTENTS

Acknowledgements . . . iii
Abstract . . . v
Published Content and Contributions . . . vi
Table of Contents . . . vi
List of Illustrations . . . viii
List of Tables . . . xv
Chapter I: Introduction . . . 1
1.1 Motivation . . . 1
1.2 Approach . . . 6
1.3 Science Questions . . . 8
1.4 Thesis Outline . . . 9
Chapter II: Response of Monsoon Rainfall to Changes in the Latitude of the Equatorward Coastline of a Zonally Symmetric Continent . . . 11
2.1 Abstract . . . 11
2.2 Introduction . . . 11
2.3 Methods and Tools . . . 14
2.4 Seasonal Cycle . . . 17
2.5 Role of Dynamics . . . 24
2.6 Discussion . . . 36
2.7 Conclusion . . . 38
2.8 Acknowledgements . . . 39
Chapter III: Response of Monsoon Onset Timing to Greenhouse Warming in an Idealized GCM . . . 40
3.1 Abstract . . . 40
3.2 Introduction . . . 40
3.3 Methods and Tools . . . 45
3.4 Seasonal Cycle . . . 52
3.5 Energetic Framework Perspective . . . 67
3.6 Discussion and Conclusion . . . 81
Chapter IV: Conclusion . . . 87
4.1 Thesis Summary and Concluding Remarks . . . 87
4.2 Motivation for Future Work . . . 90
Bibliography . . . 97

LIST OF ILLUSTRATIONS

Number *Page*

1.1 Annual mean precipitation calculated from GPCP monthly long-term mean precipitation from 1981−2010 (color). Various monsoon systems around the world (stipple) where, using only regions with local mean summer (May-September) precipitation exceeding local mean winter (November-March) precipitation by at least 2.5 mm per day, the local summer precipitation exceeds 55% of annual total. 2

1.2 GPCP daily precipitation seasonal cycle, with climatological mean taken over 1997−2012 and zonal mean taken over from top to bottom: a) the South Asian Monsoon (60°E − 100°E), b) the North American Monsoon (180°W − 60°W), and c) North African Monsoon (30°W − 60°E). Precipitation contour interval: 1 mm day^{-1}. The black plus signs indicate the monsoon onset, calculated as the time when the precipitation averaged from 10°N to 30°N exceeds its annual mean. . 4

1.3 Taken from Fig. 2 in Dwyer et al. (2014): The CMIP5 RCP8.5 multimodel mean change (2080-99) minus (1980-99) for: d) amplitude change and f) phase delay in the annual cycle of precipitation. Any location where the first harmonic makes up less than 50% of the total variance for precipitation is not shaded. Additionally, only grid points that have at least an annual mean precipitation of 1 mm day^{-1} are shaded. 5

2.1 Model setup: (a) schematic of continental configuration for the 10° simulation, where land and ocean have a mixed layer depths of 0.2 m and 20 m respectively, and (b) the ocean Q flux distributions for each simulation. 15

2.2 Seasonal cycles from simulations with southern boundaries of land at 0°, 10°, 20°, 30°, and 40° and the all-ocean aquaplanet. Color contours indicate precipitation (contour interval 2 mm day^{-1}). Magenta contours indicate near-surface MSE taken at $\sigma = 0.887$ (contour interval 8×10^3 J kg^{-1}). The equator is marked in a solid horizontal black line and the southern boundary of land in each simulation is shown in a dotted horizontal black line. The dashed vertical lines mark June 21 and September 11, used in the analysis for Figs. 2.6, 2.7, and 2.8. The black x's indicate monsoon onset as calculated in Zhou and Xie (2018), while the black plus signs and the black circles indicate monsoon onset and retreat as calculated in Walker and Bordoni (2016). 18

2.3 Cumulative moisture flux convergence mean (10°N–30°N), normalized by the minimum for each simulation, from which the monsoon onset and retreat indices are calculated as in Walker and Bordoni (2016). Resulting monsoon onset (dashed) and retreat (dotted) indices are listed in Table 2.2. 20

2.4 Seasonal cycle of the lower-level mass streamfunction and zonal wind from simulations with southern boundaries of land at 0°, 10°, 20°, 30°, and 40° and the all-ocean aquaplanet. Color contours indicate lower-level ($\sigma = 0.887$) zonal wind (contour interval 2 m s^{-1}). Black contours mark the lower-level mass streamfunction Ψ_{low} (counterclockwise in solid, clockwise in dashed with contour interval $40{\times}10^9$ kg s^{-1}, zero contour in bold). The equator, southern boundary of the continent, and June 21 and September 11 are marked as in Fig. 2.2. 21

2.5 Solsiticial (NH summer in filled circles and SH summer in open circles) ITCZ position (red), near-surface MSE maximum (blue), EFE (green), and first-order estimate of EFE from BS14 (purple) for all simulations. Note the discontinuities in the x axis. 24

2.6 (Top) Total streamfunction Ψ in black (counterclockwise in solid, clockwise in dashed with contour interval 20×10^9 kg s^{-1}) and angular momentum contours in magenta (contour interval $\Omega a^2/15$) and (bottom) precipitation (blue) and near-surface ($\sigma = 0.887$) MSE distribution (red) from the 10° simulation. 26

2.7 Same as in Fig. 2.6 from the 30° simulation. 27

2.8 Decomposition of the total streamfunction Ψ into eddy Ψ_e (left column) and mean Ψ_m (right column) momentum flux components from simulations with southern boundaries of land at 10° (a, b) and 30° (c, d) at June 21 (top) and September 11 (bottom). Ψ_e and Ψ_m are in black contours (counterclockwise in solid, clockwise in dashed with contour interval 20×10^9 kg s^{-1}). The eddy momentum flux divergence is shown in color contours (contour interval 4×10^{-6} m s^{-2}) and is calculated as $-\nabla \cdot (\overline{p}_s \overline{u'v'}^{\sigma} \cos\phi)/\overline{p}_s$, where $\overline{p}_s$ is the zonal and temporal mean surface pressure, $\overline{(\cdot)}^{\sigma}$ is a surface pressure-weighted zonal and temporal mean along sigma surfaces, and $(\cdot)'$ indicates deviations from the mean. The NH and SH maxima in both Ψ_e and Ψ_m are given in 10^9 kg s^{-1} and marked by the arrows. 29

2.9 Seasonal cycle of the terms in the upper-level ($\sigma = 0.195$) zonal momentum budget in Eq. (3.3): (a) zonal mean Coriolis term $f\overline{v}$, (b) mean flow advection $-(\overline{v}\partial\overline{u}/\partial y + \overline{\omega}\partial\overline{u}/\partial p)$, and (c) transient eddy momentum flux convergence $-(\partial\overline{u'v'}/\partial y + \partial\overline{u'\omega'}/\partial p)$ from the 10° simulation with contour interval 1.5×10^{-5} m s^{-2}, and same terms: (d), (e), and (f), respectively, from the 30° simulation with contour interval 0.5×10^{-5} m s^{-2}. Vertical dashed lines mark June 21 and September 11 and the horizontal dotted line represents the continent southern coastline. 31

2.10 Seasonal cycles of upper-level ($\sigma = 0.195$) zonal wind u_{up} (contour interval 7 m s^{-1}) from the (a) 10° and (b) 30° simulations. Vertical dashed lines mark June 21 and September 11 and the horizontal dotted line represents the continent southern coastline. 32

2.11 Seasonal cycle and decomposition of terms in the vorticity budget in Eq. (2.7) from the 10° simulation at $\sigma = 0.195$: (a) $-\mathbf{u} \cdot \nabla(\overline{\zeta} + f)$ (contour interval 0.06 day^{-2}), (b) $\partial(\overline{\zeta} + f)/\partial y$ (contour interval 0.1×10^{-10} m^{-1} s^{-1}), (c) $\overline{v}$ (contour interval 0.6 m s^{-1}), (d) $-(\overline{\zeta}+f)\nabla\cdot\overline{\mathbf{u}}$ (contour interval 0.06 day^{-2}), (e) $\nabla \cdot \overline{\mathbf{u}}$ (contour interval 0.04 day^{-1}), and (f) $\overline{\zeta} + f$ (contour interval 0.2 day^{-1}). Vertical dashed lines mark June 21 and September 11 and the horizontal dotted line represents the continent southern coastline. 33

2.12 As in Fig. 2.11, but from the 30° simulation and contour intervals: a) 0.03 day^{-2}, b) 0.1×10^{-10} m^{-1} s^{-1}, c) 0.3 m s^{-1}, d) 0.03 day^{-2}, e) 0.02 day^{-1}, and f) 0.2 day^{-1}. 35

2.13 Total vorticity tendency (sum of the vortex stretching and horizontal advection tendencies from Figs. 2.11 and 2.12, contour interval 0.06 day^{-2}). 36

3.1 Panel a) contains the scatter plot of global annual mean daily precipitation rate (P) versus global annual mean surface temperature (T_s) from all eight simulated climates. Panel b) shows the scatter plot of the percentage change in global mean precipitation versus the global mean change in surface temperature. The dashed line reveals the linear fit of ΔP to ΔT, which increase at a rate of 2.5% K^{-1}. Panel c) contains the scatter plot of absolute maximum streamfunction (Ψ_{max} in kg s^{-1}) versus the global annual mean surface temperature (T_s in K). 47

3.2 The seasonal cycles of precipitation from the coldest (top left) to warmest (bottom right) simulated climates are shown in the blue contours (contour interval: 0.25 mm day^{-1} ($\alpha \leq 0.5$) and 1.0 mm day^{-1} ($\alpha \geq 1.0$)). The magenta line tracks the precipitation weighted centroid following Eq. (3.2) with $n = 5$. Along the time axis, the monsoon onset and retreat indices calculated following the WB16 method using the CMFC are marked with plus signs and open circles, respectively. 53

3.3 Solstitial NH summer mean ITCZ position (red), near-surface MSE maximum (blue), and precipitation weighted centroid from Adam et al. (2016)a (purple) versus the global annual mean surface temperature from each simulation. 54

3.4 The seasonal cycles of the near-surface ($\sigma = 0.9633$) temperature gradient (K per degree latitude) from the coldest (top left) to warmest (bottom right) simulated climates are shown in the color contours (contour interval: 0.1 K per degree latitude). The magenta line tracks the latitude of the absolute maximum in precipitation that we associate with the moisture flux convergence driven by the large-scale overturning circulation. The green line tracks the latitude of the local maximum in precipitation between 10°S and 10°N, which we associate with boundary layer dynamics. Both lines have been smoothed by calculating the moving mean over a sliding window of five pentads centered around the current pentad. The onset and retreat indices are marked, as in Fig. 3.2. 56

3.5 Three-pentad mean distributions of precipitation centered around May 1, June 1, July 1, August 1, and September 1 (top to bottom) from the climates with $\alpha = 0.2$ (blue, left y-axis), 1.0, and 4.0 (orange solid and dotted, respectively, right y-axis). 57

3.6 The mass streamfunction in black (counterclockwise in solid, clockwise in dashed; contour interval: 30×10^9 kg s^{-1}) and angular momentum contours in magenta (contour interval: $\Omega a^2/30$) from the climates with $\alpha = 0.2$ (left column), 1.0 (middle column), and 4.0 (right column). Each plot contains the three-pentad mean distributions centered around first day of each month from May to September (shown in chronological order from top to bottom row). 58

3.7 Cumulative moisture flux convergence (CMFC) mean and cumulative net precipitation $(P - E)$ (CPME) mean (10°N–30°N), normalized by the minimum for each simulation, from which the monsoon onset and retreat indices are calculated as in Walker and Bordoni (2016). Resulting monsoon onset and retreat indices (vertical lines) are listed in Table 3.2. 60

3.8 Seasonal cycle of the lower-level mass streamfunction and zonal wind from the coldest (top left) to warmest (bottom right) simulated climates. Color contours indicate lower-level ($\sigma = 0.887$) zonal wind (contour interval: 2 m s^{-1}). Black contours mark the lower-level mass streamfunction Ψ_{low} (counterclockwise in solid, clockwise in dashed with contour interval 40×10^9 kg s^{-1}, zero contour in bold). Onset and retreat are marked, as in Fig. 3.2. 62

3.9 Seasonal cycle of the terms in the upper-level (height chosen at vertical level with maximum southward meridional wind) zonal momentum budget in Eq. (3.3): zonal mean Coriolis term $f\overline{v}$ (left column), mean flow advection $-(\overline{v}\partial\overline{u}/\partial y + \overline{\omega}\partial\overline{u}/\partial p)$ (middle column), and transient eddy momentum flux convergence $-(\partial\overline{u'v'}/\partial y + \partial\overline{u'\omega'}/\partial p)$ (right column) from the $\alpha = 0.2$, 1.0, and 4.0 simulations (top to bottom rows, respectively) with contour interval 0.2×10^{-5} m s^{-2} ($\alpha = 0.2$), 0.5×10^{-5} m s^{-2} ($\alpha = 1.0$), and 0.8×10^{-5} m s^{-2} ($\alpha = 4.0$). Note that values from each climate are plotted on different color ranges due to the large differences in magnitudes between the simulations. 65

3.10 Seasonal cycle of the upper-level (same as in Fig. 3.9) zonal wind u from the α = 0.2, 1.0, and 4.0 simulations (top to bottom) with contour interval 2 m s^{-1} (α = 0.2), 3 m s^{-1} (α = 1.0), and 5 m s^{-1} (α = 4.0). Note each plot shows a different color range due to the large differences in magnitudes between the simulations. The positive values from the α = 4.0 climate are saturated to show more detail. 66

3.11 Seasonal cycle of the NH tropical mean (10°N - 30°N) of the terms in the MSE budget: F_{net} (top), the mean component of the energy flux divergence $\partial\langle\overline{vh}\rangle/\partial y$ (middle), and the energy storage $\partial\langle\mathscr{E}\rangle/\partial t$ (bottom) from all the simulated climates. 68

3.12 Seasonal cycles of the tropical mean terms in the MSE budget from the α = 0.2 (top), α = 1.0 (middle), and α = 4.0 (bottom) climates. F_{net} (purple) is balanced by the sum of the mean energy flux divergence (blue), the eddy energy flux divergence (red), the energy storage (green), and the remaining residual term (gray). On the right y-axis, precipitation (pink) is plotted to highlight the relative timing of all the seasonal changes. Note different y-axis ranges are used to show more detail within each climate. 70

3.13 The changes relative to the current climate in the interseasonal differences (April minus July) of the terms of the atmospheric energy budget equation (Eq. (3.4)). 72

3.14 The changes relative to the current climate in the interseasonal differences (as in Fig. 3.13) of the latent energy tendency component of the MSE tendency plotted in Fig. 3.13. 74

3.15 The April (left column) and July (right column) monthly mean changes relative to the current climate in latent energy storage. The change in latent energy tendency $\Delta\frac{\partial\langle L_v q\rangle}{\partial t}$ calculated directly from the model output (top row) and calculated as the RHS of the linear approximation in Eq. (3.5) (middle row). The surface temperature tendency $\frac{\partial T_s}{\partial t}$ from each climate used to calculate the linear approximation (bottom row). 75

3.16 The seasonal cycles of the tropical mean a) latent energy storage $\partial\langle L_v q\rangle/\partial t$, b) latent energy storage normalized by the maximum of each curve to show more detail, and c) surface temperature tendency $\partial T_s/\partial t$. 78

3.17 The seasonal cycles of the tropical mean ocean energy storage O_s (a) and the terms in the surface energy budget (Eq. (3.6)): shortwave flux to the surface (b), longwave flux out of the surface (c), surface latent heat flux out of the surface (d), surface sensible heat flux out of the surface (e), and ocean Q flux (f). Note the different y-axis ranges of each plot. 79

3.18 The anomalous streamfunctions during the first pentad of each month from May to September (top to bottom) from comparing the current climate to the $\alpha = 0.5$ climate (left column) and comparing the $\alpha = 2.0$ climate to the current climate (right column). The same contour styles and interval are used as in Fig. 3.6. 83

4.1 Schematic summarizing the two main theoretical frameworks the analyses of this thesis centers around. 89

4.2 Seasonal cycles from simulations with southern boundary of land at 10° (marked by the dotted line). Color contours indicate precipitation (contour interval: 1.5 mm day^{-1}). The maximum in precipitation (green) and low-level ($\sigma = 0.887$) MSE (magenta) are marked. Both lines have been smoothed by calculating the moving mean over a sliding window of five pentads centered around the current pentad. The black plus signs and the black circles indicate monsoon onset and retreat as calculated in Walker and Bordoni (2016) and shown in Table 4.1. 93

4.3 Seasonal cycles, as in Fig. 4.2, for simulations with southern boundary of land at 30° (marked by the dotted line). 93

4.4 A comparison of the calculated monsoon onset (filled circles) and retreat (open circles) within the South Asian monsoon region from eight models from the CMIP6 archive and MERRA-2 (black) observations. The onset and retreat are calculated using the same metric based on the cumulative moisture flux convergence (WB16). The CMIP6 results include results from 15 historical years (2000-2014) (blue) and 15 future years from the SSP5-8.5 scenario (2086-2100) (red). 95

LIST OF TABLES

Number *Page*

1.1 Important metrics calculated from the observed South Asian (SAM), North American (NAM), and North African (NAF) monsoon regions from GPCP daily precipitation data (1997-2012), shown in Fig. 1.2. . . 3

2.1 Q flux amplitudes and widths used for each simulation. 16

2.2 Dates of monsoon onset and retreat, as calculated in Walker and Bordoni (2016) 19

3.1 Atmospheric optical depth multiplication factor abs used for each simulation, and resulting global annual mean surface temperatures (T_s) and precipitation amounts (P). 46

3.2 Dates of monsoon onset and retreat calculated with the WB16 method using the cumulative MFC (CMFC), and similarly with the cumulative net precipitation (cumulative ($P - E$), CPME). 59

4.1 Simulations run combining the effects of idealized continent and climate change. The onset and retreat metrics following WB16 are listed. 92

4.2 The calculated shifts in monsoon onset, retreat, and season length between 15 future years from the SSP5-8.5 warming scenario and 15 historical years (2000-2014) from eight models from the CMIP6 archive. 95

Chapter 1

INTRODUCTION

1.1 Motivation

Monsoons are seasonal transitions of the large-scale tropical circulation that are coupled to the tropical precipitation and bring abundant summertime rainfall to regions that experience otherwise arid winters. At least half of the world's population relies on water from the monsoons, therefore these circulations have large impacts on economics, food security, health, and migration. As continental-scale circulations, monsoons determine the environmental conditions of regions in Asia, Africa, and the low-latitude Americas throughout the year. With such large socio-economic impacts, improving understanding of important aspects of the monsoon, such as the monsoonal precipitation pattern, intensity, and onset timing, is crucial.

Studies over the past two decades have revolutionized our understanding of monsoons as intimately tied to the tropical overturning circulation and the intertropical convergence zone (ITCZ), where the tropical precipitation maximum is located. Monsoons are now widely considered a manifestation of the seasonal transitions of the Hadley circulation. These large-scale circulations work to export energy away from their ascending branches and are energetically driven (e.g., Biasutti et al., 2018), meaning they respond to the insolation seasonal cycle. As a result, they have large-scale seasonal excursions into the summer hemisphere subtropical continents and project strongly onto the global zonal mean (e.g., Walker, 2017; Walker & Bordoni, 2016). Key to this improved understanding has been the use of idealized aquaplanet general circulation models (GCMs). These models helped develop fundamental understanding of the dynamics (e.g., Held & Hou, 1980; Lindzen & Hou, 1988; Plumb & Hou, 1992; Privé & Plumb, 2007a) and energetics (e.g., Chou & Neelin, 2004; Kang et al., 2009; Kang et al., 2008; Neelin, 2007; Neelin & Held, 1987) that govern the large-scale tropical overturning circulation. Recently, by including a seasonal cycle of insolation with no surface asymmetries, Bordoni and Schneider (2008) and Schneider and Bordoni (2008) were able to generate simulated monsoons, even in the absence of land-sea contrast long thought to be a critical element of monsoon climate. Using the AM budget, this work developed theory to explain the rapid monsoon onset based on dynamical arguments com-

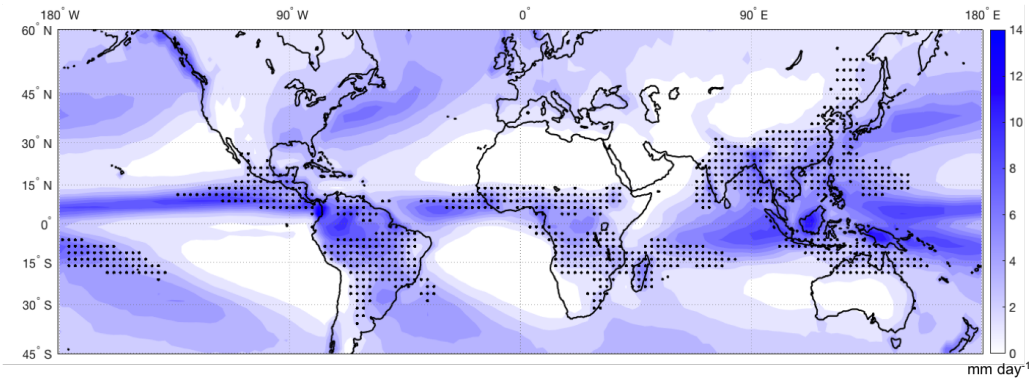

Figure 1.1: Annual mean precipitation calculated from GPCP monthly long-term mean precipitation from 1981−2010 (color). Various monsoon systems around the world (stipple) where, using only regions with local mean summer (May-September) precipitation exceeding local mean winter (November-March) precipitation by at least 2.5 mm per day, the local summer precipitation exceeds 55% of annual total.

bined with expectations from convection quasi-equilibrium, independent of surface inhomogeneities.

While recent work suggests that land-sea contrast is not necessary to generate monsoons (Bordoni & Schneider, 2008), there is no doubt that the land-sea distribution influences observed monsoons in important ways. All regional monsoons are characterized by rainfall largely confined in the warm season, with accompanying circulation changes. However, each monsoon can differ in its strength, extent, and onset timing depending on factors such as topography and continental geometry (Chou et al., 2001). Using Global Precipitation Climatology Project (GPCP) Version 2.3 monthly long-term mean precipitation observations from 1981-2010 (Adler et al., 2003), Fig. 1.1 shows the annual mean precipitation, and marks the regions where the local summertime precipitation exceeds 55% of the annual total, or otherwise recognized as the various monsoon regions around the globe. Within the annual mean precipitation, the most striking feature is the main band of tropical precipitation, which marks the annual mean ITCZ, where moisture is converged by the annual mean tropical overturning circulation. The influence of tropical continent on the annual mean ITCZ is immediately obvious. While the ITCZ position and width are relatively consistent over ocean, over different land regions, the ITCZ is able to extend further poleward. These regions match well the location of the monsoon regions, where the summertime precipitation makes up the majority of the annual total (stipple). Between the various monsoon regions, striking differences in the precipitation intensity and poleward extent can also be observed. For example,

Table 1.1: Important metrics calculated from the observed South Asian (SAM), North American (NAM), and North African (NAF) monsoon regions from GPCP daily precipitation data (1997-2012), shown in Fig. 1.2.

Monsoon Metrics				
Region	Longitude	Onset	JJA ITCZ	DJF ITCZ
SAM	10°E-100°E	16 May	17.7°	-5.9°
NAM	180°W-60°W	7 Jun	7.9°	-11.2°
NAF	30°W-60°E	1 Jun	8.3°	-18.4°

the Asian monsoon systems have the strongest precipitation intensity and poleward extent while the North American monsoon region is much smaller.

Fig. 1.2 shows a closer look at the seasonal cycles of precipitation averaged in longitude over the different monsoon regions in the Northern Hemisphere (NH). Here, we use the GPCP Version 1.2 daily data from 1997-2012 to examine more closely differences in the timing of the seasonal transitions in different monsoon regions (Huffman et al., 2016). A monsoon onset metric is calculated based on when the NH tropical mean (10°N to 30°N) precipitation exceeds the annual mean, and used for comparison. The onset of the South Asian monsoon (SAM, Fig. 1.2a), the largest-scale of Earth's monsoons, appears as a rapid and dramatic rearrangement of the precipitation patterns, with the main convergence zone shifting rapidly from the near-equatorial ocean into the subtropical continent. Another striking feature is the asymmetry between a rapid onset and a much more gradual retreat. While also featuring somewhat rapid onsets, the North American (NAM) (Fig. 1.2b) and North African (NAF) (Fig. 1.2c) monsoon regions, do not feature the same poleward extension of the monsoonal rains and the same degree of asymmetry between a rapid onset and a more gradual retreat. Table 1.1 quantifies these observations and compares the calculated onset timing and solsticial mean ITCZs between the different monsoon regions. The SAM features the earliest monsoon onset at May 16, compared to the more gradual and delayed onsets of June 7 and June 16 in the NAM and NAF regions, respectively. The rapid monsoon onset in the SAM is also accompanied by a larger NH summer mean (June, July, and August – JJA) ITCZ poleward excursion, extending to 17.7°N. The poleward excursions of the NAM and NAF regions are comparably small, only reaching 7.9°N and 8.3°N, respectively. These observations clearly demonstrate the important influence continental geometry may have on setting key characteristics of the monsoon and motivates us to

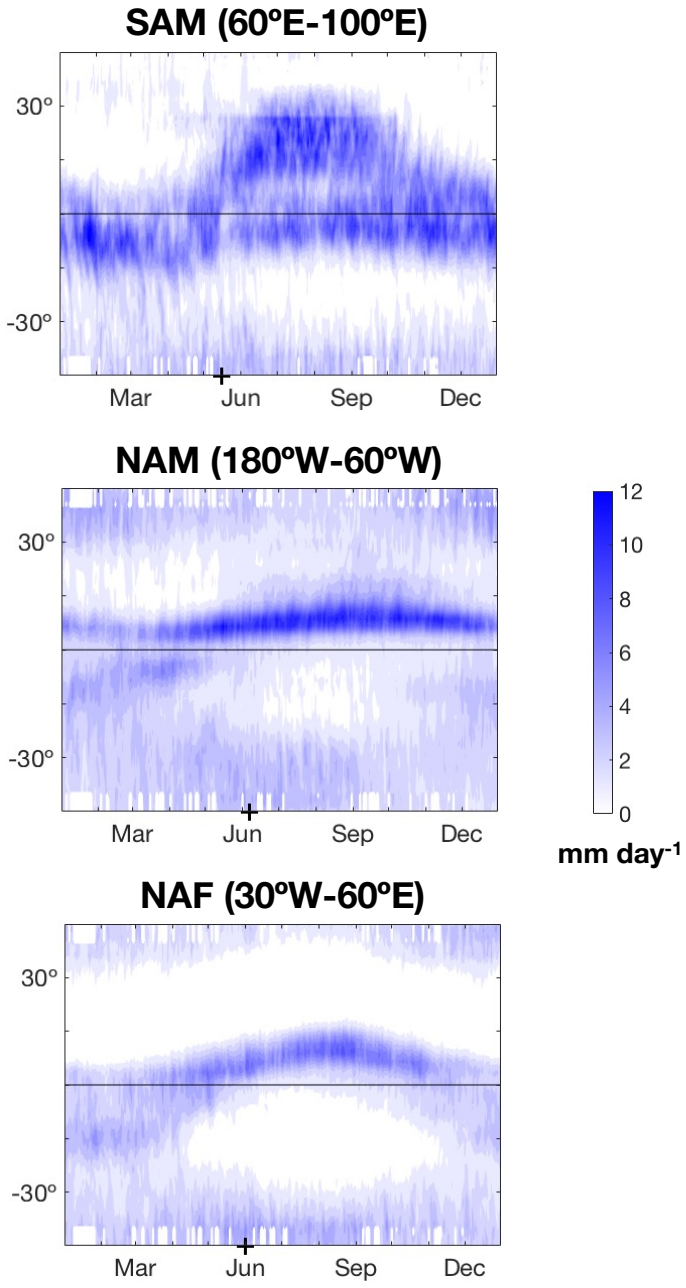

Figure 1.2: GPCP daily precipitation seasonal cycle, with climatological mean taken over 1997–2012 and zonal mean taken over from top to bottom: a) the South Asian Monsoon ($60°E$ – 100°E), b) the North American Monsoon ($180°W$ – 60°W), and c) North African Monsoon ($30°W$ – 60°E). Precipitation contour interval: 1 mm day^{-1}. The black plus signs indicate the monsoon onset, calculated as the time when the precipitation averaged from 10°N to 30°N exceeds its annual mean.

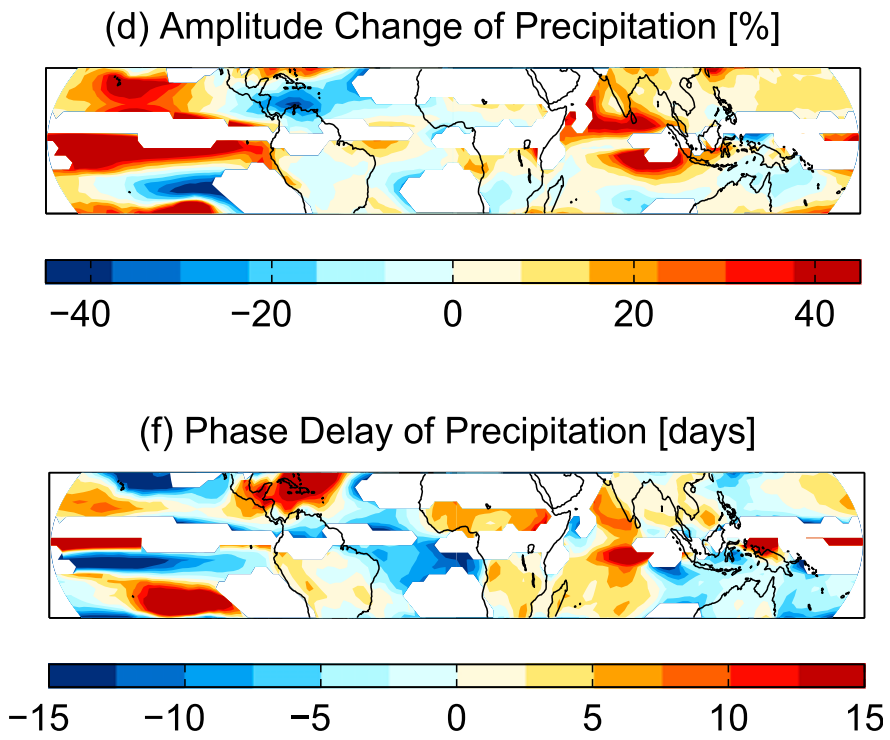

Figure 1.3: Taken from Fig. 2 in Dwyer et al. (2014): The CMIP5 RCP8.5 multimodel mean change (2080-99) minus (1980-99) for: d) amplitude change and f) phase delay in the annual cycle of precipitation. Any location where the first harmonic makes up less than 50% of the total variance for precipitation is not shaded. Additionally, only grid points that have at least an annual mean precipitation of 1 mm day^{-1} are shaded.

investigate the leading-order effects.

Within recent climate change studies, both in observations and comprehensive models, some tropical global zonal mean changes are widely agreed upon. As the climate warms, the global zonal mean tropical precipitation will increase (e.g., Chou & Lan, 2012; Chou et al., 2007; Chou & Neelin, 2004; Geng et al., 2020; Held & Soden, 2006; Huang et al., 2013; Kitoh et al., 2013; Lan et al., 2019; Su et al., 2017; Wang et al., 2014; S.-P. Xie et al., 2010) and the zonal mean Hadley circulation will weaken (e.g., Held & Soden, 2006; Lu et al., 2007; Seidel & Randel, 2007; Staten et al., 2018). Additionally, GCMs within the Coupled Model Intercomparison Project Phase 5 (CMIP5) and Phase 6 (CMIP6) archives robustly project a delay in the timing of monsoon onset with warming (Biasutti & Sobel, 2009; Dwyer et al., 2014; Song et al., 2018; Song et al., 2021). However, once the global zonal asymmetry is broken, the monsoonal response to climate change paints a different

picture. Using CMIP5 models forced with increased greenhouse gases, Dwyer et al. (2014) performed an annual mode analysis of the seasonal cycle of precipitation to look for trends in the amplitude and phase (Fig. 1.3). Their results showed that different tropical regions are predicted to respond to climate warming differently, in both the amplitude and phase of the annual cycle of precipitation. For example, the NAM region is expected to experience a drying and delaying of monsoon onset with warming, whereas the SAM region may experience an increase in precipitation with delayed onset. Seth et al. (2013) also showed that within CMIP5 models, different monsoon regions may experience different changes in the precipitation amount and onset timing, proposing the differing responses may be due to differing response of surface latent heat flux over land and over ocean. Song et al., 2021 analyzed CMIP5 and CMIP6 simulations and found robust onset delay averaged over the tropical land but regionally, the signals are most noticeable over the Sahel and South Asian monsoon regions. These studies emphasize the potential for continental geometry to not only determine the monsoons in our current climate, but also their responses to future climate change.

1.2 Approach

Experimental Design

This thesis aims to explore the potential influence continental geometry and climate change can have on the monsoon onset timing and precipitation spatial distribution. In the real world, many factors, such as topography, land surface conditions, aerosols, etc., can also influence the monsoon and make determining responsible mechanisms difficult. Recent studies have shown that approaches in which complexity is increased progressively can help develop understanding of fundamental dynamics in the absence of other complicating but poorly understood factors (Collins et al., 2018; Jeevanjee et al., 2017). For this reason, we choose to investigate these influences using an idealized aquaplanet GCM. In this way, we can employ a model hierarchy, where model complexity is built up step by step, to look at the influences of continental geometry and climate warming, first separately and eventually combined.

The first part of this work focuses on just the effect of continent under the current climate. We focus only on the leading-order effect of the heat capacity difference between land and ocean and run a set of idealized aquaplanet simulations, where land and ocean only vary by the mixed-layer depth (MLD). Using different configurations of zonally-symmetric NH land where the land extends to the North Pole and the

latitude of the southern coastal boundary is varied, we explore the role of hemispheric asymmetry in the surface thermal inertia on the spatial poleward extent and rapidity in onset timing of the monsoonal precipitation. Although similar approaches have been taken in models with more realistic physics (e.g., Chou et al., 2001; Dirmeyer, 1998; S. Xie & Saiki, 1999), here we attempt to fill the gap between idealized aquaplanet GCMs and comprehensive models.

The second part of this work focuses only on the effect of a warming climate on the monsoon. Using the same idealized aquaplanet model, we run a set of simulations covering a wide range of both colder and warmer climates than the current climate. We vary the climate by only varying the atmospheric longwave optical depth, to mimic climate changes due to greenhouse gases. A uniform MLD then is used in all the simulations to ensure the changes we see are only attributable to climate changes. We study the changes in the monsoonal precipitation, both in the spatial pattern and onset timing, but with an emphasis on the changes in the latter, as there is still a need for a unified perspective to connect various proposed mechanisms (Biasutti & Sobel, 2009; Dwyer et al., 2014; Song et al., 2018).

Our goals from these two parts are to learn what are the leading-order effects of continent and climate warming individually, to inform us on future analysis of monsoon changes when the two effects are combined.

Theoretical Frameworks

Throughout the thesis, our analysis will be centered around the use of two main theoretical frameworks – 1) the angular momentum (AM) budget and 2) the energetic framework. These frameworks are useful guides for us to link the atmospheric dynamics to the energetics by linking the large-scale tropical circulation to the MSE budget and precipitation. Chapters 2 and 3 review the two theoretical frameworks in more detail, but here we provide a general explanation of the fundamental concepts and motivation for using these frameworks.

The AM budget helps us distinguish two different dynamical flow regimes, one where the tropical circulation is tied to the strength of the extratropical eddies, and the other, a monsoon regime, where the Hadley circulation becomes more angular momentum conserving (AMC) and is more energetically direct. We will use this framework to study the seasonal cycle of the tropical circulation, and analyze changes in the switch between the two dynamical regimes to identify monsoon onset and study changes in the onset timing and transition rapidity.

To study shifts in the position of the ITCZ and the coupled tropical circulation, we use the energetic framework. Substantial work in the past decade has linked changes in the ITCZ position with changes in the atmospheric energy budget (Biasutti et al., 2018; Bischoff & Schneider, 2014; Boos & Korty, 2016a; Frierson et al., 2013; Kang et al., 2008; Schneider et al., 2014). This framework connects the region of maximum moist static energy (MSE) flux divergence to the region of maximum net energy input (NEI) into the atmospheric column. Energy divergence is mainly performed in the upper branches of the Hadley circulation, since higher MSE is maintained in the upper atmosphere. As a result, the region of maximum NEI is collocated with the ascending branch of the Hadley circulation. As a region of intense ascent of hot moist tropical air, the ITCZ is embedded within the ascending branch. We will use the powerful MSE budget framework to connect changes in the vertically-integrated atmospheric energy budget to circulation and precipitation changes.

1.3 Science Questions

As introduced above, the goal of this work is to understand how both continent and climate change will affect the monsoon onset timing and spatial distribution of precipitation. We want to use our understanding of the AM budget and energetic framework to address the following questions:

- How does the inclusion of NH land influence the spatial distribution of the monsoonal precipitation and the rapidity of the onset? Does varying the hemispheric asymmetry in surface thermal inertia affect the circulation and coupled precipitation annual cycles?
- How does the monsoon onset timing and spatial distribution of precipitation evolve under a warming climate? Between a wide range of colder and warmer climates, what are the main differences in the MSE budget and the AM budget that account for these changes?
- Following the energetic framework that links the maximum in NEI into the atmospheric column to the region of maximum energy flux divergence and precipitation, can we relate the climate state to the spatial distribution and seasonal evolution of the NEI into the atmospheric column? How may the seasonal migration of the ITCZ be linked to seasonal dependencies of the MSE budget?

- We interpret the monsoon onset as a dynamical transition from one regime, where the eddy momentum fluxes have influence on the strength of the Hadley circulation, to a more closely AMC monsoon regime, where the tropical meridional overturning circulation decouples from the eddy momentum flux divergence (EMFD) and becomes thermally direct and can respond quicker to thermal forcing. How will this dynamical regime transition change under various climates? How will the timing and speed of the transition be affected? Can we develop a theory to link the climate state to the relative importance of nonlinear momentum advection by the mean circulation versus the EMFD?

- Both the AM budget and the energetic framework have been useful tools to study the spatial distribution and seasonal evolution of tropical precipitation (Biasutti et al., 2018). Are both frameworks able to explain the response of monsoon precipitation to hemispheric asymmetric continent and global warming to provide complementary views from dynamical and energetic perspectives? Does one framework provide stronger constraints than the other under certain conditions?

1.4 Thesis Outline

This thesis follows the work of our two main studies that investigate the influence of continent and climate change on the monsoonal precipitation. Chapter 2 reviews our study of the influence of zonally-symmetric NH land on the monsoonal precipitation under the current climate. We describe interesting changes in the seasonal cycles of the precipitation, MSE, and circulation that we observe between the different simulated continental configurations. We also apply the AM budget to analyze the dynamical flow regime transition associated with monsoon onset and show that having regions of tropical land are necessary to generate rapid monsoonal circulation transitions. In the absence of these regions, the circulation transitions are delayed and smoother, and altogether do not resemble observed monsoons. In Chapter 3, we describe our work focusing solely on the effects of a warming climate. We discover monsoon onset delays with warming in our simulations, even in the absence of land-sea contrast. We find further evidence of the onset delay with warming by looking at the changes in the dynamical regime transition from a regime heavily influenced by extratropical eddies to the AMC monsoon regime. Using the MSE budget framework, we relate changes in the seasonal cycle of atmospheric energy storage to observed changes in the onset timing. Chapter 4 provides an overarching summary of the two studies. We also present some preliminary results from our

new idealized aquaplanet GCM simulations combining the effects of continent and climate change and some analysis of the SAM region within CMIP6, and reflect on how our previous studies can inform us on these analyses.

Chapter 2

RESPONSE OF MONSOON RAINFALL TO CHANGES IN THE LATITUDE OF THE EQUATORWARD COASTLINE OF A ZONALLY SYMMETRIC CONTINENT

Hui, K. L., & Bordoni, S. (2021). Response of monsoon rainfall to changes in the latitude of the equatorward coastline of a zonally symmetric continent. *Journal of the Atmospheric Sciences*, *78*(5), 1429–1444. https://doi.org/10.1175/JAS-D-20-0110.1.

2.1 Abstract

Recent studies have shown that the rapid onset of the monsoon can be interpreted as a switch in the tropical circulation, which can occur even in the absence of land-sea contrast, from a dynamical regime controlled by eddy momentum fluxes to a monsoon regime more directly controlled by energetic constraints. Here we investigate how one aspect of continental geometry, that is the position of the equatorward coastal boundary, influences such transitions. Experiments are conducted with an aquaplanet model with a slab ocean, in which different zonally symmetric continents are prescribed in the Northern Hemisphere poleward from southern boundaries at various latitudes, with "land" having a mixed layer depth two orders of magnitude smaller than ocean. For continents extending to tropical latitudes, the simulated monsoon features a rapid migration of the convergence zone over the continent, similar to what is seen in observed monsoons. For continents with more poleward southern boundaries, the main precipitation zone remains over the ocean, moving gradually into the summer hemisphere. We show that the absence of land at tropical latitudes prevents the rapid displacement into the subtropics of the maximum in lower-level moist static energy and, with it, the establishment of an overturning circulation with a subtropical convergence zone that can transition rapidly into an angular momentum conserving monsoon regime.

2.2 Introduction

The monsoon is a prominent climatological phenomenon of the summertime circulation that dominates the annual cycle over much of the tropics and subtropics. It brings abundant rainfall to regions that feature otherwise very arid winters, so

its onset, strength, and variability have large socioeconomic impacts. All regional monsoons are characterized by rainfall largely confined to the warm season, with accompanying circulation changes.

In disagreement with traditional views of monsoons as large-scale sea breeze circulations, understanding has recently emerged and led to novel consideration of these systems as intimately tied to the tropical overturning circulation and associated Intertropical Convergence Zone (ITCZ). In fact, monsoons are now widely viewed as broad, cross-equatorial Hadley circulations that are energetically direct and export energy away from their ascending branches (e.g., Biasutti et al., 2018) and that project strongly on the global zonal mean (e.g., Walker, 2017; Walker & Bordoni, 2016). According to this emerging view, monsoons are a manifestation of the seasonal excursion of the ITCZ into the summer hemisphere subtropical continents. In this respect, theories that have been developed for the understanding of the Hadley cell and its response to perturbations by different forcings and on different timescales might be applicable, at least to some extent, to the understanding of monsoons.

Key to this advanced understanding have been theoretical constraints on tropical overturning circulations dictated by large-scale budgets of angular momentum (AM) (e.g., Held & Hou, 1980; Lindzen & Hou, 1988; Plumb & Hou, 1992; Privé & Plumb, 2007a) and energy (e.g., Chou & Neelin, 2004; Kang et al., 2009; Kang et al., 2008; Neelin, 2007; Neelin & Held, 1987) and highly idealized modeling studies, including aquaplanets. For instance, in simulations with idealized general circulation models (GCM) with a seasonal cycle and no zonal asymmetries, Schneider and Bordoni (2008) and Bordoni and Schneider (2008) showed that the rapid onset of the monsoon might be interpreted as a switch between a dynamical regime where the tropical circulation strength is controlled by eddy momentum fluxes (C. Walker & Schneider, 2006) and a monsoon regime where the circulation approaches AM conservation and its strength is more directly controlled by energetic constraints, which causes the monsoonal cross-equatorial cell to grow rapidly in strength and poleward extent. This switch can happen even in the absence of surface inhomogeneities, provided that the lower boundary has low enough thermal inertia. The sensitivity of the transition rate and latitudinal extent to year length, lower boundary thermal inertia, and rotation rate was more recently explored by Geen et al. (2018, 2019). Additionally, Geen et al. (2018) provide a complimentary view to the AM budget by focusing on the vorticity budget and finding that this transition can also be thought of as a rapid reduction in the upper-level absolute vorticity within the tropical circulation due to

positive horizontal advection and negative vortex stretching tendencies.

AM conservation by a circulation in the monsoon regime, together with thermal wind balance, requires that the circulation boundary be located in a region of zero vertical wind shear, where free tropospheric temperatures maximize (Lindzen & Hou, 1988). For a moist atmosphere in convective quasi-equilibrium (CQE), in which convection maintains a moist adiabatic temperature profile and upper-tropospheric temperatures covary with the subcloud moist static energy (MSE) (e.g., Emanuel et al., 1994), the circulation boundary will have to be colocated with the maximum in lower-level MSE (e.g., Emanuel, 1995; Privé & Plumb, 2007a). In other words, dynamical constraints from AM conservation together with thermodynamic constraints imposed by convection yield a strong coupling between the circulation and the distribution of lower-level MSE. While not prognostic, given that the circulation itself influences the MSE distribution, the resulting relationship has proved very powerful in allowing for a mechanistic understanding of how factors such as land geometry, orography, albedo, and ocean fluxes impact the monsoonal rainfall through their impact on the MSE distribution. For instance, it has led to a reinterpretation of the role of topography in the South Asian monsoon: long considered necessary to drive a strong monsoon through elevated heating (Flohn, 1957), topography is now recognized as a mechanical insulator, preventing mixing between cold and dry extratropical air and the moist and warm monsoonal air (Boos & Kuang, 2010; Molnar et al., 2010).

An alternative framework that has also allowed for significant progress in the understanding of the zonally averaged Hadley cell and the ITCZ has been based on the atmospheric energy budget, which interprets the ITCZ response as part of the meridional energy fluxes necessary to restore energy balance to a given perturbation (Bischoff & Schneider, 2014; Kang et al., 2008). While the extension of this framework to zonally asymmetric circulations, such as monsoons, remains an area of active research (e.g., Adam et al., 2016; Boos & Korty, 2016b), constraints that apply to the zonal mean could also prove useful to regional monsoons (e.g., Schneider et al., 2014). See Hill (2019) for a review of merits of and outstanding challenges in energy-based theories of monsoons.

In this work, we aim to understand how simple aspects of continental geometry influence the fundamental dynamics of monsoonal circulations building on more idealized work. As argued by recent studies (Collins et al., 2018; Jeevanjee et al., 2017), approaches in which complexity is increased progressively allow for

understanding of fundamental dynamics in the absence of other complicating but poorly understood factors. Although uniform mixed layer depth (MLD) aquaplanet studies have provided great understanding of how MLD may affect the monsoon dynamical transition rate (Bordoni & Schneider, 2008; Geen et al., 2018, 2019), in this work we take a step towards realism by introducing meridional asymmetry in the lower boundary. Expanding on the work of Laraia (2015), who introduced a zonally symmetric continent in the Northern Hemisphere (NH) with a southern boundary at 10°N in an aquaplanet GCM with idealized physics, we run the same model with five different zonally symmetric configurations of NH land that extends poleward from southern boundaries at various latitudes to vary the hemispheric asymmetry in thermal inertia. Similar approaches were taken in models with more realistic physics (e.g., Chou et al., 2001; Dirmeyer, 1998; S. Xie & Saiki, 1999). Here we attempt to fill the gap between idealized aquaplanet GCMs and comprehensive models. This approach was recently taken by Zhou and Xie (2018), who used a GCM similar to the one used here to study the effects of land albedo, continental extent, and soil moisture on the monsoon through their influence on near-surface equivalent potential temperature (and hence MSE). Relevant to this study is the finding that the monsoon weakens significantly as the equatorward coastal boundary is displaced poleward. Similar goals also motivated the Tropical Rain belts with an Annual cycle and a Continent Model Intercomparison Project (TRACMIP, Voigt et al. 2016). What distinguishes our work from these previous studies is the use of just one model to study the response of both monsoon onset timing and spatial distribution to systematic changes in one aspect of continental configuration (position of the equatorward coastal boundary) and the dynamical perspective provided by analyses of associated changes in the AM and vorticity budgets. Section 2.3 describes the idealized GCM and simulations used in this study, as well as the monsoon onset indices. Section 2.4 focuses on the seasonal cycle of precipitation in the different experiments, while Section 2.5 interprets these results using dynamical constraints from the AM and the vorticity budgets. Discussion and conclusions follow in Sections 2.6 and 2.7, respectively.

2.3 Methods and Tools

Idealized GCM

A moist idealized aquaplanet GCM based on the Geophysical Fluid Dynamics Laboratory (GFDL) Flexible Modeling System (Frierson et al., 2006; O'Gorman & Schneider, 2008) is used, which solves the primitive equations of motion on a

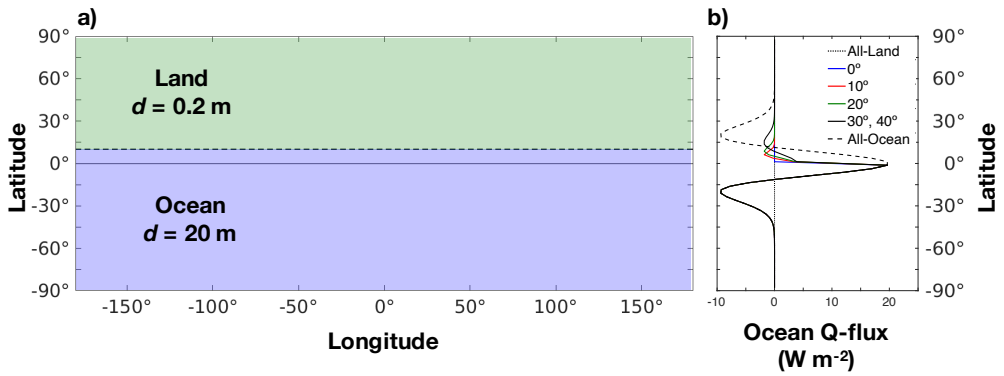

Figure 2.1: Model setup: (a) schematic of continental configuration for the 10° simulation, where land and ocean have a mixed layer depths of 0.2 m and 20 m respectively, and (b) the ocean Q flux distributions for each simulation.

sphere with the Earth's radius.

The lower boundary of the model consists of a slab ocean, with sea surface temperatures (T_s) evolving according to the surface energy budget:

$$c\rho d\frac{\partial T_s}{\partial t} = O_s = S^s - L^s - LH - SH - \nabla \cdot F_0, \tag{2.1}$$

with ocean heat storage O_s on the left hand side, with water specific heat c, density ρ, and MLD d, being balanced by radiative and turbulent energy fluxes into the surface (with net incoming shortwave flux S^s, net outgoing longwave flux L^s, outgoing sensible and latent heat fluxes, respectively SH and LH) and any energy flux convergence by ocean currents ($-\nabla \cdot F_0$, also known as Q flux). Land and ocean only differ in the corresponding MLD d, which we choose as 0.2 m for land and 20 m for ocean. A two-stream grey radiation scheme is used where the optical depth is prescribed. While a diurnal cycle is not included, the GCM is forced by a seasonal cycle of insolation with a 360-day Julian year, using realistic Earth-like values of obliquity and solar constant of 23.5° and 1360 W m^{-2} respectively, but zero eccentricity. The GCM includes an active hydrological cycle, where precipitation can form by either large-scale condensation or convection following a simplified Betts-Miller convection scheme as in Frierson (2007). Since precipitation is assumed to fall out immediately, there is no liquid water or ice in the atmosphere, hence no clouds. To compensate for the lack of clouds, we use a spatially-uniform surface albedo of $\alpha = 0.38$. With these simplifications, this GCM does not account for important climate feedbacks such as surface albedo, cloud, or radiative water vapor feedbacks, but nonetheless well resolves tropical and extratropical circulations,

Table 2.1: Q flux amplitudes and widths used for each simulation.

Q flux Parameters				
Simulation	Q_{NH}	ϕ_{NH}	Q_{SH}	ϕ_{SH}
Land	0	16°	0	16°
0°	0	5°	20	16°
10°	4	5°	20	16°
20°	4	7°	20	16°
30°	4	12°	20	16°
40°	4	12°	20	16°
Ocean	20	16°	20	16°

their mutual interactions, and their impact on the hydrological cycle.

For this study, we perform five simulations with an idealized continent. The model is run with fully saturated NH land ($d = 0.2$ m) that extends poleward from southern boundaries at 0°, 10°, 20°, 30°, and 40° (Fig. 2.1a), with ocean MLD $d = 20$ m. Two uniform MLD aquaplanet simulations were also run: one with all land ($d = 0.2$ m everywhere) and one with all ocean ($d = 20$ m everywhere), to which we will refer to as the all-land and the all-ocean cases, respectively. For each simulation, the ocean energy transport is prescribed through the ocean Q flux term in Eq. (2.1) following the zonally symmetric and time-invariant form in Merlis et al. (2013b):

$$\nabla \cdot F_o(\phi) = \begin{cases} Q_{NH} \frac{1}{\cos\phi}\left(1 - \frac{2\phi^2}{{\phi_{NH}}^2}\right) \exp\left(\frac{-\phi^2}{{\phi_{NH}}^2}\right), & \text{if } \phi > 0 \\ Q_{SH} \frac{1}{\cos\phi}\left(1 - \frac{2\phi^2}{{\phi_{SH}}^2}\right) \exp\left(\frac{-\phi^2}{{\phi_{SH}}^2}\right), & \text{if } \phi < 0. \end{cases} \tag{2.2}$$

In the all-ocean simulation, we used $Q_{NH} = Q_{SH} = 20$ and widths $\phi_{NH} = \phi_{SH} = 16°$. For each simulation including land, Q_{NH} and ϕ_{NH} are varied (Table 2.1) so that the ocean heat transport (OHT, the meridional integral of the Q flux) approaches zero at the coastline (Fig. 2.1b). Consistently, it is zero everywhere in the all-land simulation. Every simulation was performed with T42 horizontal spectral resolution with 30 vertical levels and run for 20 years, with data from the last 10 years used in the analyses shown below. Since our model uses a zonally-symmetric setup, all fields presented in this study are global zonal averages. Because land and ocean differ only by their MLD, the only aspect of the land-sea contrast we account for is the capability of the ocean to store and transport energy due to its higher thermal inertia and prescribed ocean Q flux.

Monsoon Onset Metrics

To quantitatively analyze the influence of continental geometry on the monsoon onset timing, we calculate monsoon onset using two methods. The first identifies onset as the pentad at which the mean precipitation (averaged over 10° to 30°) first exceeds its annual mean, similar to Zhou and Xie (2018) and to which we refer to as the ZX18 index. We also calculate onset following the method described in Walker and Bordoni (2016), to which we refer to as the WB16 index. The WB16 index is based on detecting the change point of a two-phase linear regression of the cumulative moisture flux convergence (CMFC) over a representative region (here taken as the latitudinal band between 10° and 30°, Fig. 2.3). Because the moisture flux convergence primarily balances net precipitation, this index detects onset as the time at which net precipitation switches from negative to positive (and withdrawal as the opposite transition).

2.4 Seasonal Cycle

In this study we regard the monsoon as excursions into subtropical latitudes of the ITCZ embedded within the ascending branch of the cross-equatorial Hadley cell. In this section, we begin by reviewing the observed seasonal cycle of the precipitation and the circulation and we then explore how well energetic predictors capture this evolution.

Temporal Structure

The seasonal cycle of precipitation from each simulation with idealized continent and the all-ocean case is depicted in Fig. 2.2 (color contours). Here, and in most of the following figures, results from the all-land simulation are not shown because they are similar to those discussed in earlier studies (Bordoni & Schneider, 2008; Geen et al., 2018, 2019). Some important statistics and metrics from this case are however presented below. Overall, the precipitation temporal structure in simulations with land extending into the tropics northward of 0°, 10°, and 20° all have a similar asymmetry, characterized by a rapid cross-equatorial jump of the ITCZ from the Southern hemisphere (SH) into the NH during NH spring and a slower retreat back to the SH in NH fall—this behavior is similar to that seen within observed monsoons. In contrast, the 30° and 40° simulations look generally similar to the all-ocean simulation, with a relatively smooth ITCZ progression.

In addition to the gross behaviour described above, some interesting and unexpected features arise from the inclusion of a simple hemispheric asymmetry in MLD. More

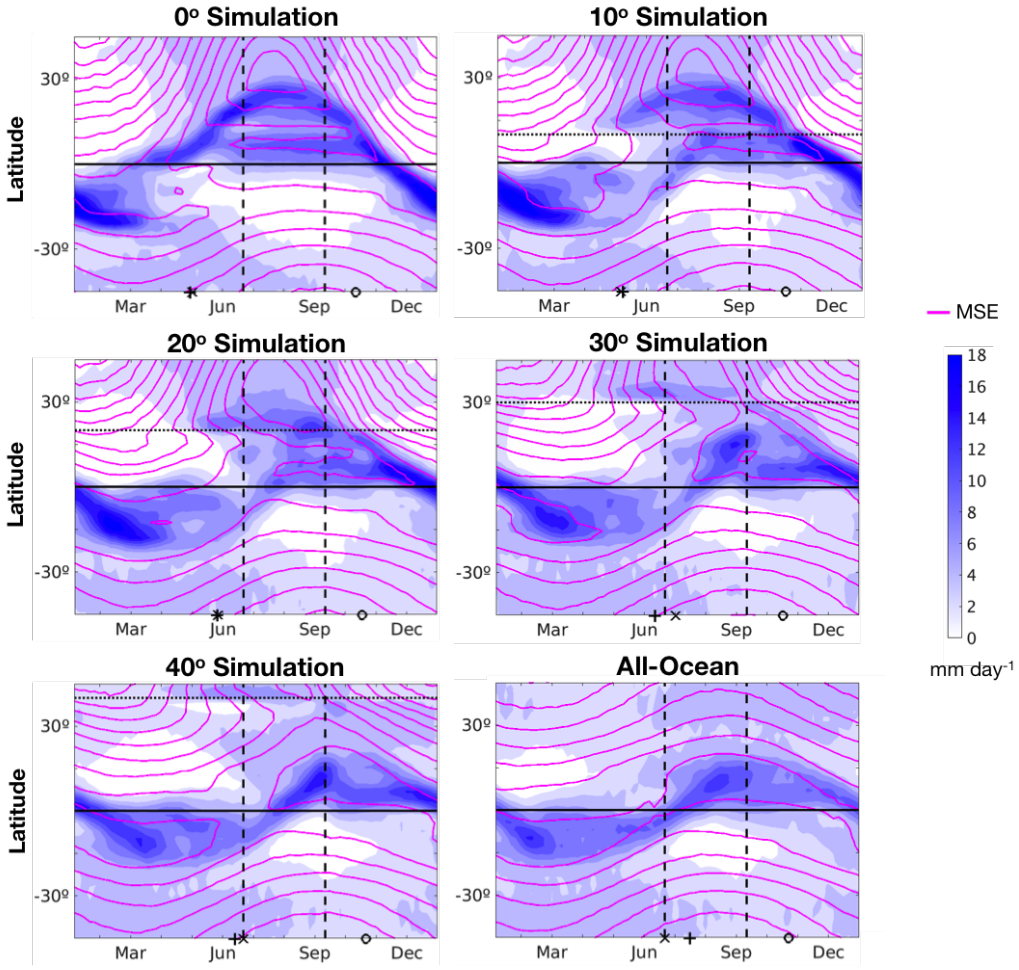

Figure 2.2: Seasonal cycles from simulations with southern boundaries of land at 0°, 10°, 20°, 30°, and 40° and the all-ocean aquaplanet. Color contours indicate precipitation (contour interval 2 mm day^{-1}). Magenta contours indicate near-surface MSE taken at $\sigma = 0.887$ (contour interval 8×10^3 J kg^{-1}). The equator is marked in a solid horizontal black line and the southern boundary of land in each simulation is shown in a dotted horizontal black line. The dashed vertical lines mark June 21 and September 11, used in the analysis for Figs. 2.6, 2.7, and 2.8. The black x's indicate monsoon onset as calculated in Zhou and Xie (2018), while the black plus signs and the black circles indicate monsoon onset and retreat as calculated in Walker and Bordoni (2016).

Table 2.2: Dates of monsoon onset and retreat, as calculated in Walker and Bordoni (2016)

.

Simulation	Onset	Retreat
Land	1 May	16 Oct
0°	1 May	11 Oct
10°	6 May	16 Oct
20°	26 May	16 Oct
30°	11 Jun	16 Oct
40°	11 Jun	21 Oct
Ocean	16 Jul	21 Oct

specifically, the heating over land at the beginning of the NH warm season gives rise to a coastal precipitation maximum in every simulation. In simulations with land extending deeper in the tropics, such as the 0° and 10° simulations, this coastal precipitation maximum does not appear as distinct from the main convergence zone of the cross-equatorial Hadley cell, which, thanks to mechanisms described in Section 2.5, can migrate rapidly into subtropical latitudes. Notice for instance the covariation of the precipitation and the zero contour of the lower-level mass streamfunction in these two simulations (top panels of Figs. 2.2 and 2.4). As land is moved further poleward, as for instance in the 30° and 40° simulations, the two maxima become more separate, with no association between the ascending branch of the Hadley cell and the coastal precipitation maximum (Figs. 2.2 and 2.4). What drives the coastal precipitation maximum? We answer this question by analyzing the fraction of precipitation P due to moisture flux convergence, calculated as $(P-E)/P$, where E is evaporation: a fraction lower (larger) than 50% indicates that P is primarily driven by local evaporation (moisture flux convergence by the large-scale circulation). In the 10° simulation, this ratio is $\sim$ 30% during early summer, and increases to $\sim$ 70% during the peak of the summer. In the 40° simulation, this ratio never exceeds 20% at the coastal precipitation maximum. We recognize that these secondary precipitation maxima are artifacts of using a fully saturated surface in our model. Future work will include further steps towards realism by, for instance, limiting evaporation over land (e.g., Voigt et al., 2016).

Continental geometry also affects the timing of monsoon onset, which, according to both indices used here, tends to become increasingly delayed as the continent southern boundary is moved further poleward, varying over a span of two months

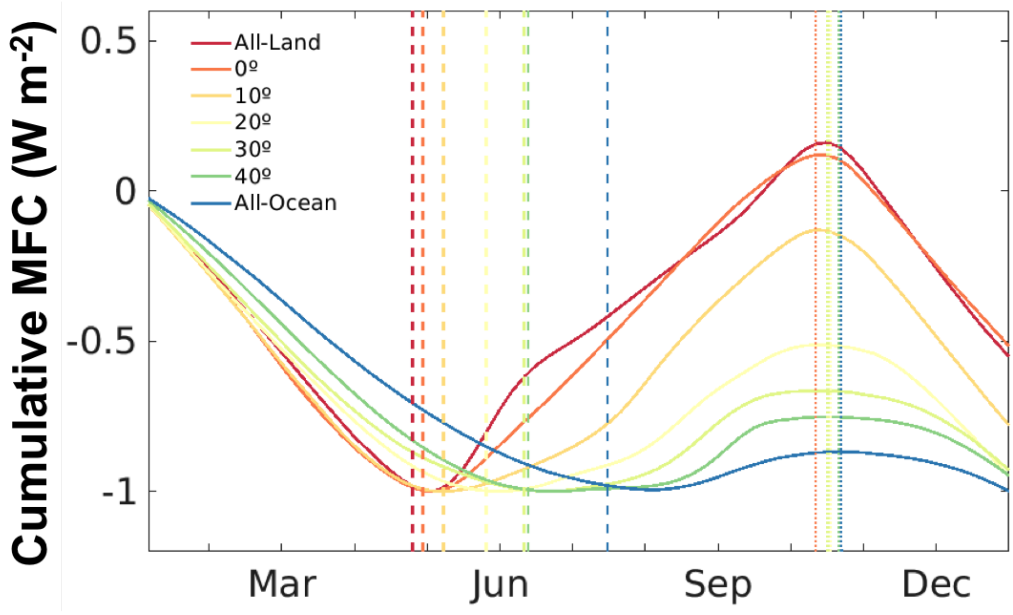

Figure 2.3: Cumulative moisture flux convergence mean (10°N–30°N), normalized by the minimum for each simulation, from which the monsoon onset and retreat indices are calculated as in Walker and Bordoni (2016). Resulting monsoon onset (dashed) and retreat (dotted) indices are listed in Table 2.2.

across all simulations (Table 2.2). Interestingly, the timing of monsoon retreat is less sensitive to the position of the coastal boundary, varying over the span of less than one month. One of the advantages of the WB16 index is that it also gives some insight into the rapidity of monsoon onset: as seen in Fig. 2.3, in the simulations with southern boundary equatorward of 20°, the rate of CMFC increase after monsoon onset strengthens rapidly, as the circulations intensifies quickly and so does the moisture flux convergence in the tropical region. In contrast, the 30°, 40°, and all-ocean simulations show relatively more gradual changes in the CMFC, reflective of less rapid changes in the circulation.

The near-surface MSE distribution (magenta lines in Fig. 2.2) shows similar features as the precipitation distribution, in agreement with expectations from CQE (e.g., Emanuel, 1995; Privé & Plumb, 2007a). The 0°, 10°, and 20° simulations show an abrupt poleward jump in the MSE maximum that coincides with the rapid ITCZ transition during NH spring. An interesting double maxima structure is also observed during the monsoon from July to September when there is also a double ITCZ. The transition during NH fall is much more gradual. Like in the precipitation distributions, the near-surface MSE transitions in the 30°, 40°, and all-ocean experiments are relatively smoother.

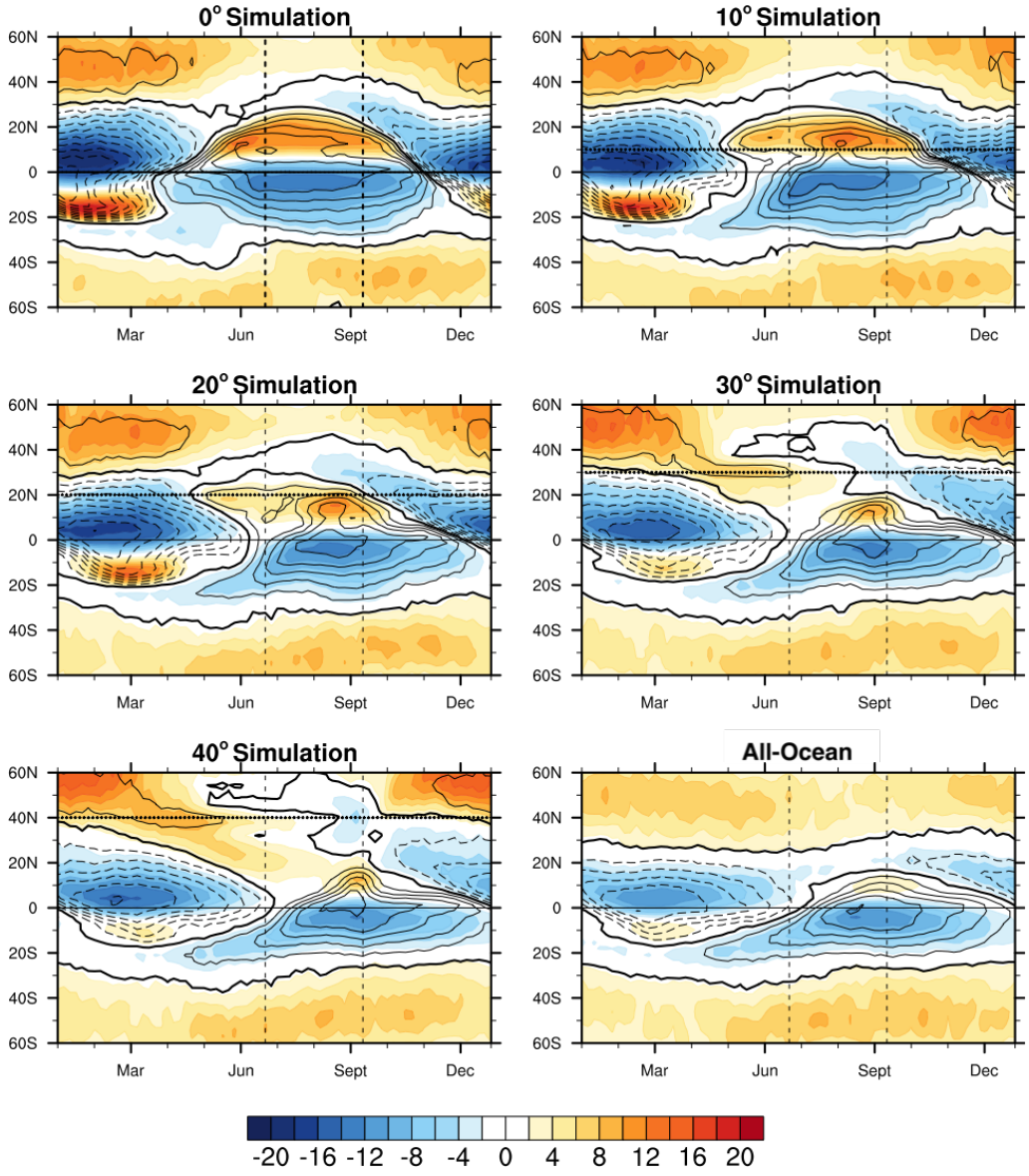

Figure 2.4: Seasonal cycle of the lower-level mass streamfunction and zonal wind from simulations with southern boundaries of land at 0°, 10°, 20°, 30°, and 40° and the all-ocean aquaplanet. Color contours indicate lower-level (σ = 0.887) zonal wind (contour interval 2 m s^{-1}). Black contours mark the lower-level mass streamfunction Ψ_{low} (counterclockwise in solid, clockwise in dashed with contour interval 40×10^9 kg s^{-1}, zero contour in bold). The equator, southern boundary of the continent, and June 21 and September 11 are marked as in Fig. 2.2.

To explore how these precipitation patterns reflect on circulation patterns, Fig. 2.4 shows the seasonal cycles of the lower-level ($\sigma = 0.887$) zonal mean mass streamfunction and zonal wind (u_{low}). In each simulation, the ascending branch of the streamfunction closely follows the precipitation maximum (Fig. 2.2), where a more asymmetric temporal structure and further poleward extent are observed in the 0°, 10°, and 20° simulations relative to those of the 30°, 40°, and all-ocean simulations. At monsoon onset in the 0°, 10°, and 20° simulations we observe a rapid establishment and intensification of lower-level westerlies from around the equator to the cross-equatorial Hadley cell's poleward boundary, compared to a relatively weaker and delayed onset of westerlies in the 30°, 40°, and all-ocean simulations. The establishment of lower-level westerly flow primarily results because the dominant zonal momentum budget in the boundary layer is a balance between the Coriolis force and friction. Westerlies must hence develop whenever northward (southward) meridional flow exists in the NH (SH) (c.f. Schneider & Bordoni, 2008). In the simulations with land extending to lower latitudes, the rapid intensification of the summer westerlies is in fact concomitant with the rapid increase in lower-level meridional winds and rapid growth in the extent of the winter Hadley cell at monsoon onset (Fig. 2.4, also see Fig. 2.6). In contrast, the summer westerlies in the simulations with land located further poleward remain weaker and more confined to the tropics, and also intensify later in the season, consistent with a more slowly growing winter Hadley cell that does not extend as far poleward into the summer hemisphere.

Connection Between the ITCZ and the Energetics

While several ITCZ metrics exist in the literature, here we identify the ITCZ as the location of the precipitation maximum. We recognize that one single parameter does not capture the complexity of the precipitation distribution (Popp & Lutsko, 2017), but this metric captures the most important trends discussed below. We also calculate three ITCZ predictors: the maximum in lower-level MSE (MSE_{max}, Privé & Plumb, 2007a), the latitude of vanishing total energy transport, the energy flux equator (EFE) (e.g., Kang et al., 2008), and its analytical approximation (c.f., Bischoff & Schneider, 2014)

$$\delta \approx -\frac{1}{a}\frac{\langle\overline{vh}\rangle_0}{\partial_y\langle\overline{vh}\rangle_0} = -\frac{1}{a}\frac{\langle\overline{vh}\rangle_0}{\overline{NEI}_0}, \tag{2.3}$$

where δ is the EFE, $\langle vh\rangle$ is the vertically integrated meridional MSE transport and NEI is the net energy input into the atmospheric column (equaling the difference between TOA radiative fluxes and surface radiative and turbulent enthalpy fluxes).

The subscript 0 indicates quantities evaluated at the equator, $\overline{(.)}$ is the time and zonal mean, and a is the Earth's radius. We refer to δ as BS14. Averages of the ITCZ and all three predictors are taken over both solsticial seasons to see how changing hemispheric asymmetry in thermal inertia can affect the ITCZ poleward migration. Given the differences in monsoon onset and withdrawal timing across simulations, these solsticial averages are computed over 15-pentad time intervals centered around the time of maximal excursion.

Not surprisingly, continental geometry strongly impacts the rainfall poleward extent (Fig. 2.5). In the simulations with NH land, while the magnitudes of the ITCZ and predictors vary slightly, they agree well on two main general trends. First, during both NH summer and SH summer, the poleward extent of the ITCZ decreases as the southern boundary of the continent is moved further poleward and the hemispheric asymmetry in thermal inertia is decreased. Second, in each simulation, the NH summer ITCZ tends to extend further poleward than the SH summer ITCZ. This asymmetry decreases as the continent is moved further from the equator. For example, the NH summer ITCZ extends $\sim 9^\circ$ further poleward than the SH summer ITCZ in the 0° simulation, but only $\sim 1^\circ$ in the 30° simulation. No asymmetry is seen in the 40° case. The hemispheric asymmetry in NEI arising from the introduction of NH land in the tropics, therefore, results in a larger poleward excursion of the summertime ITCZ. In this respect, land-sea contrast matters to the extent it can push the ITCZ far enough off the equator, in association with Hadley circulations that become more strongly cross equatorial.

Fig. 2.5 also shows the different ITCZ metrics for the all-land and all-ocean simulations. A comparison between the all-land and the 0° simulations highlights the impact of hemispheric asymmetry in the surface thermal inertia: while the two cases have similar ITCZ locations in NH summer, the ocean in the SH in the 0° simulation prevents the ITCZ from moving as far poleward during SH summer. Interestingly, in the all-ocean simulation the poleward extent of the NH summer and SH summer ITCZs is slightly larger than what is seen in the 40°. This might be because in the all-ocean simulation, precipitation maxima with wider latitudinal ranges but lower intensities are observed during NH summer and SH summer relative to the those observed in the 40° simulations (Fig. 2.2), allowing slightly more poleward solsticial ITCZs.

From the results presented above, only the simulations with land extending from the north pole down to 0°, 10°, and 20° and the all-land case are able to reproduce the

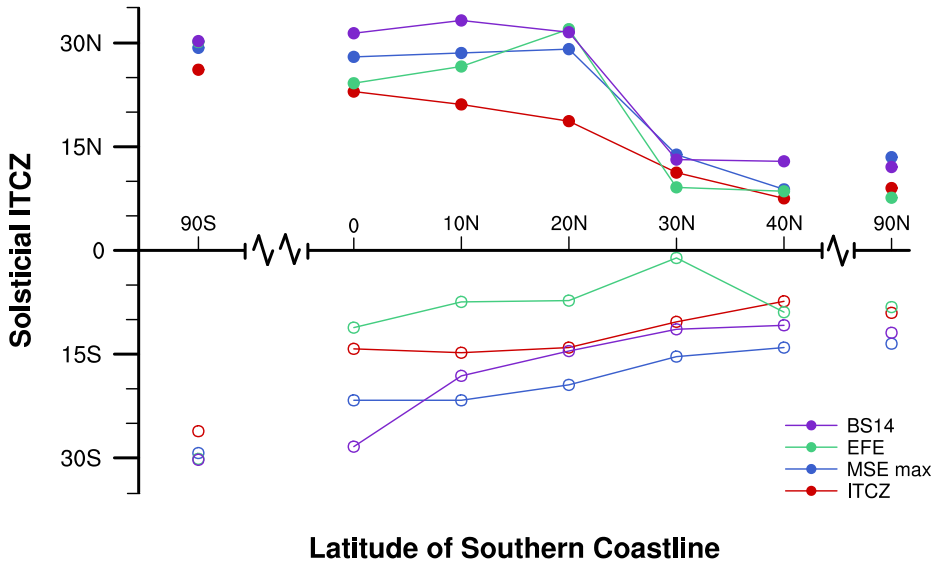

Figure 2.5: Solsiticial (NH summer in filled circles and SH summer in open circles) ITCZ position (red), near-surface MSE maximum (blue), EFE (green), and first-order estimate of EFE from BS14 (purple) for all simulations. Note the discontinuities in the x axis.

rapid cross-equatorial jump of the ITCZ and reversal of zonal winds characteristic of the monsoon. The energetic framework allows us to interpret these results, at least in terms of seasonally averaged ITCZ metrics, through the impact of the land masses on the interhemispheric asymmetry in NEI into the atmospheric column. More in depth analysis of the seasonal evolution of the EFE in relation to energetic changes is left for future work.

2.5 Role of Dynamics

To better understand the mechanisms that drive the seasonal changes described in Section 2.4, we look more closely at the overturning circulation to relate its seasonal transitions to recent monsoon dynamical theories (Bordoni & Schneider, 2008; Geen et al., 2018; Schneider & Bordoni, 2008).

Angular Momentum Budget Perspective

Schneider and Bordoni (2008) and Bordoni and Schneider (2008) showed that the rapidity of monsoon transitions in idealized aquaplanet simulations can be explained as a switch between two dynamical regimes that differ in the amount of influence eddy momentum fluxes have on the strength of the tropical circulation. The leading order balance in the zonally averaged steady-state zonal momentum

budget in the upper branch of the circulation, where friction and vertical advection can be neglected, is:

$$(f + \overline{\zeta})\overline{v} = f(1 - R_o)\overline{v} \approx \mathcal{S}, \tag{2.4}$$

with planetary vorticity $f = 2\Omega \sin\phi$, relative vorticity $\overline{\zeta} = -\partial\overline{u}/\partial y$, meridional wind v, local Rossby number $R_o = -\overline{\zeta}/f$, and transient eddy momentum flux divergence (EMFD) $\mathcal{S} = \partial\overline{u'v'}/\partial y + \partial\overline{u'\omega'}/\partial p$, where u is the zonal velocity, ω is the vertical velocity, p is pressure, and $(.)' = (.) - \overline{(.)}$ is the deviation from the time mean. While all quantities are expressed in cartesian coordinates for simplicity, both the model and our calculations below are in spherical coordinates. As discussed in Schneider (2006), R_o is a measure of how far (small R_o) or close (R_o approaching 1) the circulation is from the angular momentum conserving (AMC) limit. In the first case, that is $R_o \to 0$, Eq. (3.3) reduces to $f\overline{v} \approx \mathcal{S}$. In this regime, AM contours are vertical and the strength of the mean meridional circulation ($\overline{v}$) is tied to the EMFD. When $R_o \to 1$, the meridional AM gradient following the streamlines in the upper branch of the circulation approaches zero, and Eq. (3.3) becomes a trivial balance, no longer providing constraints on the circulation strength. In this limit, hence, the circulation responds more directly to thermal forcing (Held & Hou, 1980; Lindzen & Hou, 1988). Bordoni and Schneider (2008) and Schneider and Bordoni (2008) demonstrated that the rapid monsoon-like transition of the ITCZ into the subtropics seen in simulations with a uniform lower boundary with low thermal inertia coincides with a rapid switch of the circulation from the eddy-driven into the AMC regime.

How does the presence or absence of land in the tropics and subtropics affect these transitions? And how does changing the hemispheric asymmetry in thermal inertia influence their timing and rapidity, by for instance favoring or disfavoring the relative influence of eddies on the strength of the meridional overturning circulation (MOC) at different times of the seasonal cycle? We answer these questions by focusing on the 10° simulation, as representative of the monsoon-like case, and the 30° simulation, more representative of an ocean-like tropical ITCZ, and by analyzing in detail changes in the circulation and the associated zonal momentum budget throughout the seasonal cycle. We also choose two representative time periods (denoted in Fig. 2.2), which are 20-day periods centered around two pentads (June 21 and September 11, respectively) that represent different phases of the monsoon development in the 10° simulation: the first pentad captures the initial phase, where local moisture recycling still contributes significantly to continental precipitation;

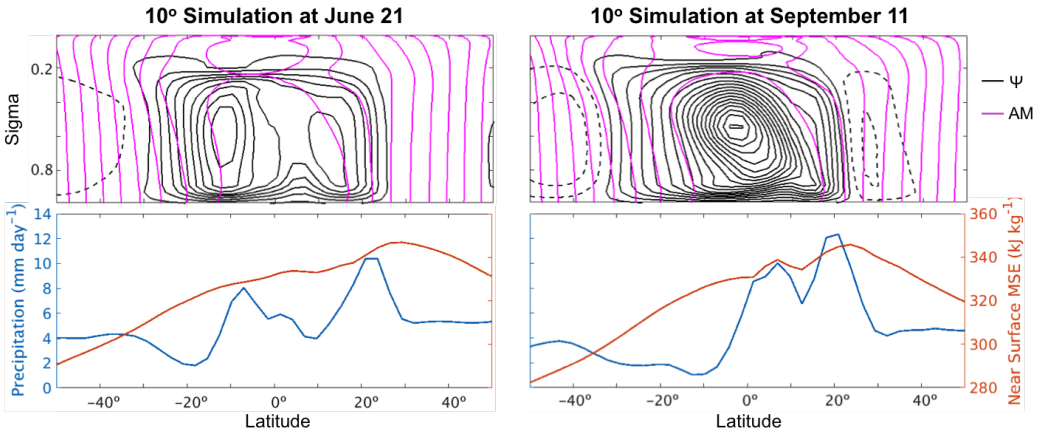

Figure 2.6: (Top) Total streamfunction Ψ in black (counterclockwise in solid, clockwise in dashed with contour interval 20×10^9 kg s^{-1}) and angular momentum contours in magenta (contour interval $\Omega a^2/15$) and (bottom) precipitation (blue) and near-surface ($\sigma = 0.887$) MSE distribution (red) from the 10° simulation.

the second pentad, instead, coincides with the peak of the monsoon, when the precipitation is mostly due to the moisture flux convergence by the broad tropical overturning circulation.

In the 10° simulation, prior to the monsoon transition in early NH summer around June 21, a single strong cross-equatorial circulation cell is not yet established, instead, two smaller circulation cells are observed (left top panel of Fig. 2.6). At this time, the AM contours (magenta) are not completely aligned with the streamlines (black) even in the ascending and upper branches, suggesting deviation from AM conservation. The lower-level MSE (left bottom panel) features one obvious maximum at $\sim 20°$ and a more subtle maximum at $\sim 10°$ due to the heating over the coastline during NH spring. This double-maxima MSE structure causes two counterclockwise circulation cells that have precipitation maxima located at the ascending branch of each cell, which explains the double ITCZ structure observed in Fig. 2.2. By September 11, a strong broad cross-equatorial winter Hadley cell is established with a weaker summer cell located north of it (right top panel of Fig. 2.6). In the upper branch, streamlines are now parallel to the AM contours and the circulation is in the AMC regime. This is the strong tropical summer circulation associated with the monsoon. The rapid movement of the lower-level MSE into subtropical latitudes made possible by the low heat capacity of land (Fig. 2.2) allows the cross-equatorial circulation to strengthen and expand rapidly. These rapid circulation changes allow for similarly rapid precipitation changes. We also note

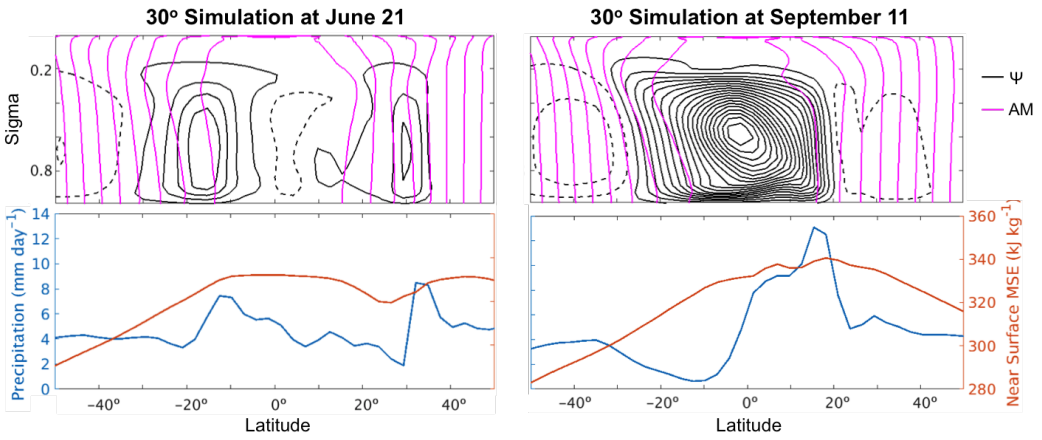

Figure 2.7: Same as in Fig. 2.6 from the 30° simulation.

the existence of a secondary precipitation maximum, located on the summer side of the equator. The secondary precipitation maximum is a very common feature of cross-equatorial circulations in both idealized and realistic simulations (e.g., Privé & Plumb, 2007a) and, as detailed in Lobo and Bordoni (2020), coincides with a region where the near-surface meridional temperature gradient changes sign. This result is consistent with the boundary layer dynamics described in Pauluis (2004), by which the flow must jump into the free troposphere in regions where the pressure gradient cannot sustain the required poleward flow.

The results from the 30° simulation (Fig. 2.7) show a different picture. Around June 21 (left column), the cell structure is more complicated than in the 10° simulation. Two counterclockwise circulations are observed just south of the equator and above the coastline at ∼ 30°, but a smaller clockwise circulation exists between them. The ascending branches of the two counterclockwise cells coincide with the lower-level MSE and precipitation maxima. The upper branches of the overturning cells cross the AM contours, which are essentially vertical. Around September 11 (right column), a broad winter Hadley cell is observed; while distortion of the AM contours from the vertical is seen, the circulation seems to be less efficient at homogenizing AM than the circulation of the 10° case at the same time. Compared to the 10° simulation, the MOC in the 30° simulation extends over regions of larger thermal inertia, which prevents the lower-level MSE from adjusting as rapidly as in the 10° simulation. Hence, the development of a cross-equatorial cell that approaches AM conservation occurs more gradually. This suggests that EMFD influences the circulation strength for a longer part of NH summer, delaying the transition into the AMC regime and preventing the circulation from growing rapidly in strength and

extent. In this respect, monsoon-like rapid transitions cannot occur if land remains limited to higher latitudes, as the circulation responds more linearly to the seasonal insolation changes.

To investigate more quantitatively the influence of eddies on the MOC, and the degree to which it approaches the AMC limit, we decompose the total streamfunction Ψ (c.f. Schneider and Bordoni 2008) into a component associated with eddy momentum fluxes

$$\Psi_e(\phi, p) = -\frac{2\pi a \cos\phi}{fg} \int_0^p \mathcal{S} dp' \tag{2.5}$$

and a component associated with the mean momentum flux

$$\Psi_m(\phi, p) = -\frac{2\pi a \cos\phi}{fg} \int_0^p \mathcal{M} dp' \tag{2.6}$$

where $\mathcal{M}$ is the mean momentum flux divergence. Above the boundary layer where frictional processes can be neglected, $\Psi = \Psi_e + \Psi_m$. Fig. 2.8 shows Ψ_e and Ψ_m (black line) over the EMFD (color) from the 10° and 30 ° simulations at June 21 and September 11. In the 10° simulation around June 21, Ψ_m starts to dominate in both hemispheres as Ψ_e starts to weaken in the subtropics (Fig. 2.8a). Around September 11 when the monsoonal circulation is broad and strong, Ψ_m clearly dominates globally and has strengthened since June 21 (Fig. 2.8b). In fact, Ψ_e is only dominant at around 30°S, expanding the extent of the circulation's descending branch in the winter hemisphere. We note that the NH maximum in Ψ_e in the tropics is associated with eddy momentum flux convergence located in the upper troposphere above the Ψ_e maximum. As discussed in previous work, this is indicative of a source of eddy activity (Held, 2000), and happens where the absolute vorticity gradient changes sign, a necessary condition for barotropic instability in the cross-equatorial cell (Pedlosky, 1964). In the 30° simulation around June 21, both Ψ_e and Ψ_m are much weaker than those at the same time in the 10° simulation and have equal influence on Ψ (Fig. 2.8c). Around September 11, Ψ_m dominates both hemispheres over Ψ_e (Fig. 2.8d). These results hence show how, once the winter Hadley cell becomes broad and well established, the influence of eddies on the strength of the circulation decreases as the MOC gets closer to the AMC limit. They also demonstrate the importance of having land extend into the tropics to enable the transition into the AMC dynamical regime to occur on a rapid intraseasonal timescale.

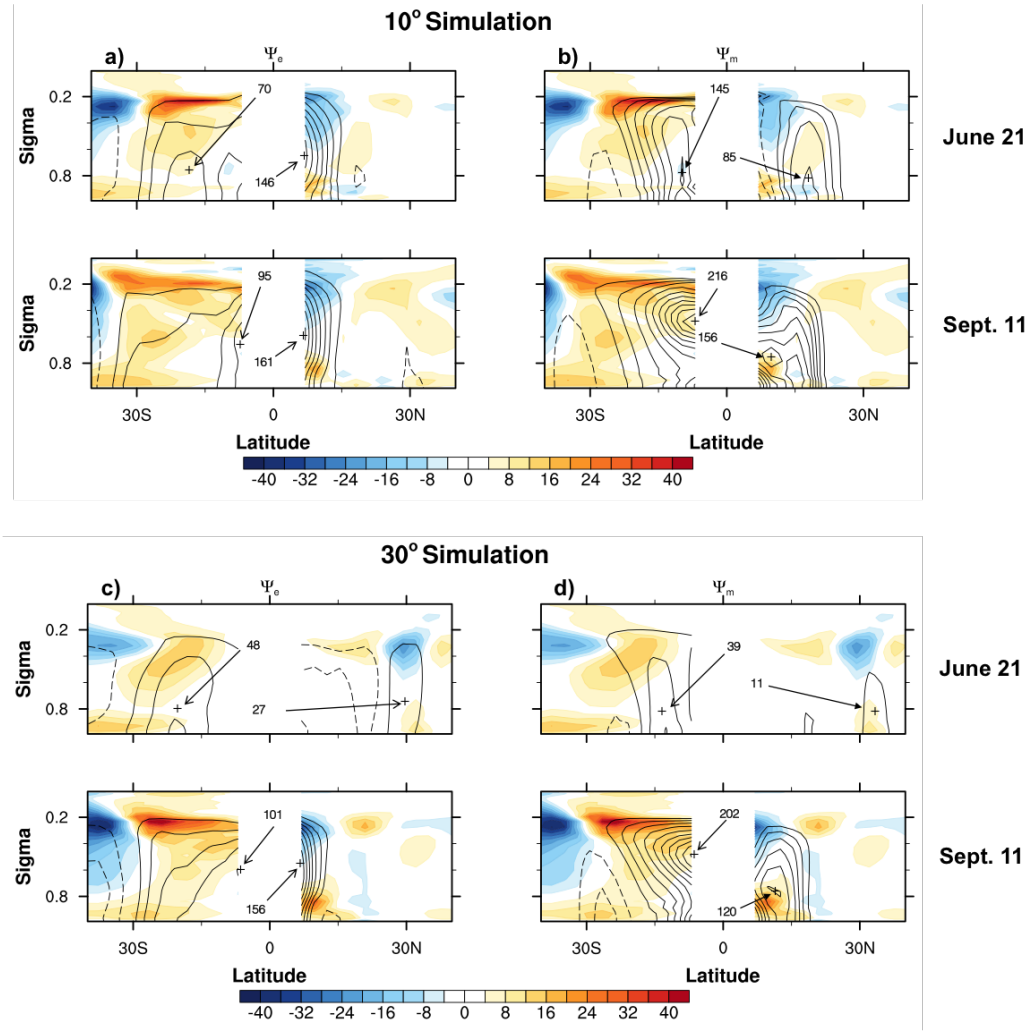

Figure 2.8: Decomposition of the total streamfunction Ψ into eddy Ψ_e (left column) and mean Ψ_m (right column) momentum flux components from simulations with southern boundaries of land at 10° (a, b) and 30° (c, d) at June 21 (top) and September 11 (bottom). Ψ_e and Ψ_m are in black contours (counterclockwise in solid, clockwise in dashed with contour interval 20×10^9 kg s^{-1}). The eddy momentum flux divergence is shown in color contours (contour interval 4×10^{-6} m s^{-2}) and is calculated as $-\nabla \cdot (\overline{p}_s \overline{u'v'}^{\sigma} \cos\phi)/\overline{p}_s$, where $\overline{p}_s$ is the zonal and temporal mean surface pressure, $\overline{(\cdot)}^{\sigma}$ is a surface pressure-weighted zonal and temporal mean along sigma surfaces, and $(\cdot)'$ indicates deviations from the mean. The NH and SH maxima in both Ψ_e and Ψ_m are given in 10^9 kg s^{-1} and marked by the arrows.

The role that tropical land plays in the rapid dynamical regime transition of the MOC becomes more apparent if we look at the seasonal cycle of the terms in the upper-level ($\sigma = 0.195$) zonal momentum budget in Eq. (3.3) (Fig. 2.9) and the upper-level zonal wind u_{up} (Fig. 2.10). The zonal mean Coriolis term $f\overline{v}$ is approximately balanced by the sum of the mean flow advection $-(\overline{v}\partial\overline{u}/\partial y + \overline{\omega}\partial\overline{u}/\partial p)$ (note that in Eq. (3.3) the vertical advection term is neglected) and the eddy momentum flux convergence (EMFC) $-(\partial\overline{u'v'}/\partial y + \partial\overline{u'\omega'}/\partial p)$. In the 10° simulation, during NH summer the poleward extent of the winter Hadley cell rapidly increases starting near June 21 (marked), and gradually retreats after September 11 (marked) around late September (Fig. 2.4). Simultaneously, over the entire extent of the winter Hadley cell, the magnitude of the zonal mean Coriolis term $|f\overline{v}|$ increases (Fig. 2.9a), with large negative values in the NH ($f > 0$) and large positive values in the SH ($f < 0$) due to the strong southward flow ($\overline{v} < 0$) over the entire cell. At the same time over the winter Hadley cell, the mean flow advection (Fig. 2.9b) strongly dominates over the EMFC (Fig. 2.9c) and approximately balances the Coriolis term. The magnitude of the mean flow advection is especially pronounced in the SH range of the winter Hadley cell. This coincides with a rapid intensification of the upper-level easterlies, which do not support westward propagating extratropical eddies (Charney, 1969; Webster & Holton, 1982), over the entire winter Hadley cell during the NH summer (Fig. 2.10a), in agreement with axisymmetric theories (c.f. Lindzen and Hou 1988). The development of the upper-level easterlies in a broad latitudinal range helps shield the winter cell from the eddy influence, which in fact remains confined only to the cell descending branch in the winter hemisphere (Fig. 2.9c).

In the 30° simulation, the regime transition is delayed and smoother. The expansion of the winter Hadley cell into the NH subtropics is more gradual than observed in the 10° simulation, and occurs later in the season around July (Fig. 2.4). The circulation not only has a smoother and delayed transition onset, but also does not extend as far polewards (~20°N) as the winter Hadley cell during NH summer in the 10° simulation (~30°N). The effects of the delay and weakening of the transition, as well as the reduced poleward extent of the winter Hadley cell, are observable in the upper-level zonal mean momentum balance (Figs. 2.9d, e, and f). First, the intensification of the Coriolis term during NH summer is delayed. Simultaneously, the dominance of the mean flow advection over the EMFC is weaker and occurs later in the season in the 30° simulation relative to in the 10° simulation. Additionally, the onset of the strengthening of the upper-level easterlies is also delayed in the 30° simulation (~ July, Fig. 2.10b) compared to the 10° simulation (~ June, Fig. 2.10a) and their peak

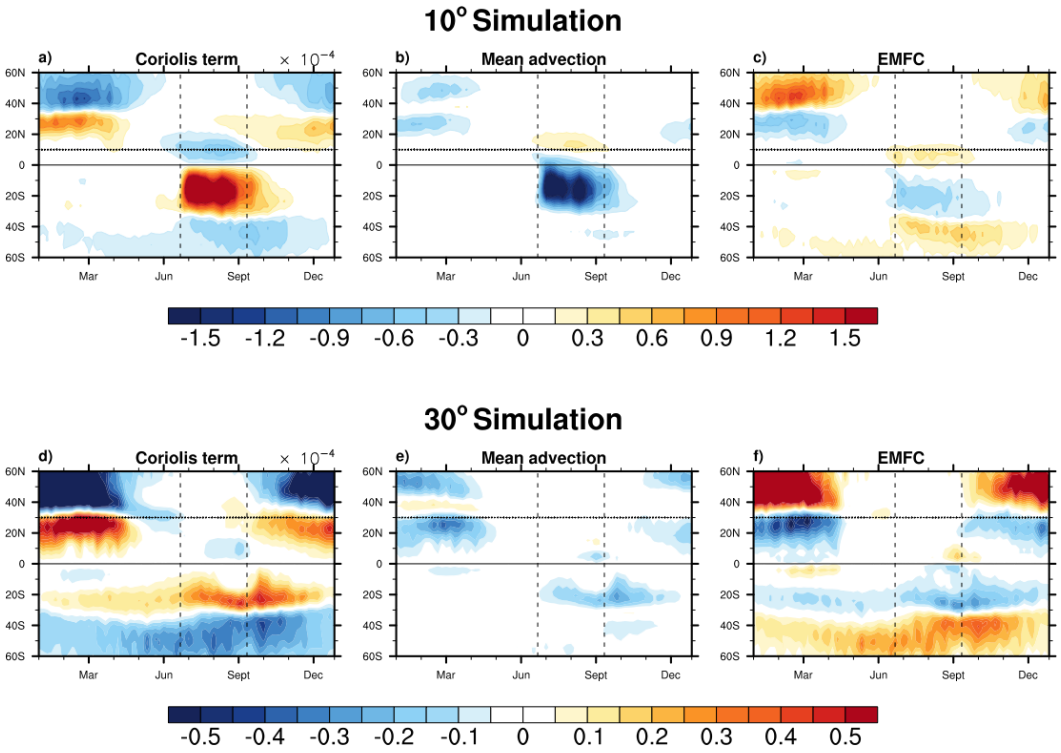

Figure 2.9: Seasonal cycle of the terms in the upper-level ($\sigma = 0.195$) zonal momentum budget in Eq. (3.3): (a) zonal mean Coriolis term $f\overline{v}$, (b) mean flow advection $-(\overline{v}\partial\overline{u}/\partial y+\overline{\omega}\partial\overline{u}/\partial p)$, and (c) transient eddy momentum flux convergence $-(\partial\overline{u'v'}/\partial y + \partial\overline{u'\omega'}/\partial p)$ from the 10° simulation with contour interval 1.5×10^{-5} m s^{-2}, and same terms: (d), (e), and (f), respectively, from the 30° simulation with contour interval 0.5×10^{-5} m s^{-2}. Vertical dashed lines mark June 21 and September 11 and the horizontal dotted line represents the continent southern coastline.

amplitude is much weaker (21.9 m s^{-1} vs. 60.2 m s^{-1}). The weakening and delay of the intensification of upper-level easterlies, as well as their reduced meridional extent, delay the timing and limit the latitudinal range over which they can effectively shield the tropical circulation from the extratropical eddies. This emphasizes that, while the tropical circulation eventually approaches the AMC regime in the 30° simulation, it does so later in the season. Overall, these results demonstrate that having land in the tropics can influence the monsoon onset mainly through enabling the circulation to switch rapidly from the regime where its strength is tied to the extratropical baroclinic eddies to the monsoon regime where it approaches the AMC limit. Tropical land is hence necessary for the development of strong monsoons with a rapid onset in so far as it provides a lower boundary with heat capacity that is low enough to allow for rapid near-surface MSE adjustments that initiate the dynamical feedbacks described above.

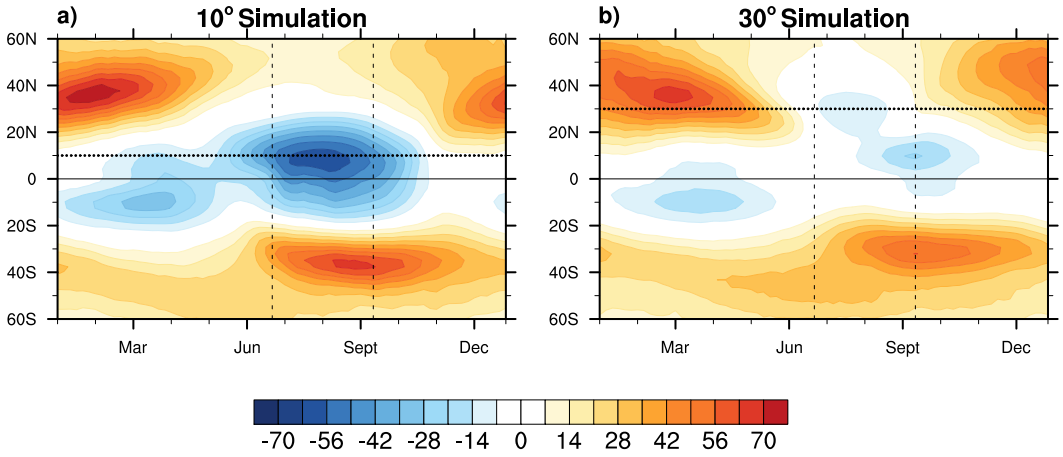

Figure 2.10: Seasonal cycles of upper-level ($\sigma = 0.195$) zonal wind u_{up} (contour interval 7 m s^{-1}) from the (a) 10° and (b) 30° simulations. Vertical dashed lines mark June 21 and September 11 and the horizontal dotted line represents the continent southern coastline.

Vorticity Budget Perspective

The dynamics of rapid monsoon transitions have recently been reinterpreted by Geen et al. (2018) in terms of the upper-level vorticity budget. Additional analyses of the upper-level vorticity budget hence provides an alternative and complementary perspective on the dynamics of monsoon transitions to that from the AM budget. Hence, in this section we analyze the seasonal cycle of the different terms in the vorticity budget, given by:

$$\frac{\partial \zeta}{\partial t} = -\mathbf{u} \cdot \nabla(\zeta + f) - \omega \frac{\partial \zeta}{\partial p} - (\zeta + f)\nabla \cdot \mathbf{u} + \mathbf{k} \cdot \left(\frac{\partial \mathbf{u}}{\partial p} \times \nabla \omega \right). \tag{2.7}$$

The vorticity tendency on the left hand side is balanced by the horizontal vorticity advection, the vertical vorticity advection, vortex stretching, and vortex tilting on the right hand side. In the upper troposphere where ω is small, and the terms with ω are small compared to the horizontal advection and vortex stretching terms, Eq. (2.7) simplifies to:

$$\frac{\partial \overline{\zeta}}{\partial t} = -\overline{v} \frac{\partial (\overline{\zeta} + f)}{\partial y} - (\overline{\zeta} + f) \frac{\partial \overline{v}}{\partial y}. \tag{2.8}$$

Throughout the season, hence the horizontal advection and vortex stretching terms act as tendencies of the upper-level absolute vorticity via changes in $\overline{\zeta}$ (Geen et al., 2018). Remembering that the upper-level absolute vorticity $f + \overline{\zeta}$ is proportional to the meridional gradient of M, a circulation with R_o approaching 1 has vanishing absolute vorticity in its upper branch (Geen et al., 2018; Schneider, 2006).

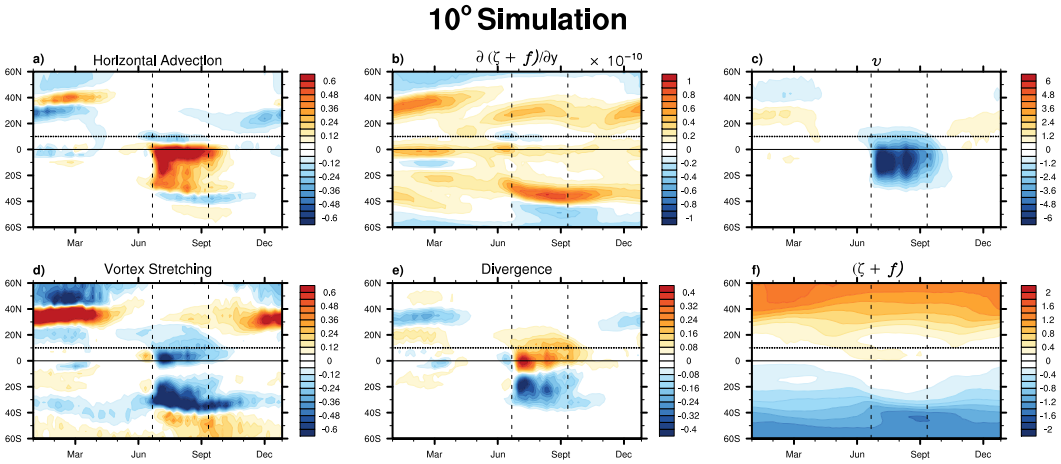

Figure 2.11: Seasonal cycle and decomposition of terms in the vorticity budget in Eq. (2.7) from the 10° simulation at $\sigma = 0.195$: (a) $-\mathbf{u} \cdot \nabla(\overline{\zeta} + f)$ (contour interval 0.06 day^{-2}), (b) $\partial(\overline{\zeta} + f)/\partial y$ (contour interval 0.1×10^{-10} m^{-1} s^{-1}), (c) $\overline{v}$ (contour interval 0.6 m s^{-1}), (d) $-(\overline{\zeta} + f)\nabla \cdot \overline{\mathbf{u}}$ (contour interval 0.06 day^{-2}), (e) $\nabla \cdot \overline{\mathbf{u}}$ (contour interval 0.04 day^{-1}), and (f) $\overline{\zeta} + f$ (contour interval 0.2 day^{-1}). Vertical dashed lines mark June 21 and September 11 and the horizontal dotted line represents the continent southern coastline.

Geen et al. (2018) proposed that, at the onset of NH summer as the ITCZ crosses the equator, simultaneously the horizontal advection tendency becomes positive and the vortex stretching tendency becomes negative in the summer hemisphere. This results in a latitudinally broad region of reduced magnitude of absolute vorticity and, hence, AM conservation. They also showed that the positive horizontal advection tendency results from southward flow in the winter cell's upper branch in NH summer, which increases (decreases) absolute vorticity in the summer (winter) hemisphere by advecting higher absolute vorticity air downgradient. The divergent flow in the ascending branch of the Hadley cell instead contributes a negative vortex stretching tendency.

The seasonal evolution of the upper-level horizontal advection and vortex stretching tendencies calculated from our 10° simulation bear similarity to those described in Geen et al. (2018) (Fig. 2.11). Focusing on the transition into NH summer, from the time the ITCZ crosses the equator before NH summer in May till the end of NH summer in September, from near the equator in the SH up to the winter Hadley cell poleward edge near 25°N is a region of reduced magnitude of absolute vorticity, as the circulation becomes more AMC (Fig. 2.11f). This results from the combined effect of positive horizontal advection of vorticity (Fig. 2.11a) and negative vortex stretching (Fig. 2.11d), whose sum is shown in Fig. 2.13a. Over

most of the meridional range of the winter Hadley cell from 30°S up to the coastline at 10°N, the horizontal advection term is positive, because of the southward mean flow and positive meridional gradient of absolute vorticity in this region, and results in a decrease in the magnitude of the negative absolute vorticity in the SH. At the same time, the vortex stretching tendency is negative from the equator up to $\sim 30°$N due to the divergent flow in the circulation's ascending branch and the positive magnitude of the absolute vorticity in this region. The combined effect (Fig. 2.13a) is the observed reduction in magnitude and meridional gradient of absolute vorticity across the winter Hadley cell from May through September (Fig. 2.11f). We do note that during NH summer there is a region of negative horizontal advection tendency around the coastline at 10°N. This results from a negative meridional gradient in vorticity over the same latitude (Fig. 2.11b), as discussed in the previous section. However, since the positive horizontal advection mainly works to reduce the magnitude of negative absolute vorticity in the SH, this patch of negative horizontal advection at the coastline does not affect the overall influence of the horizontal vorticity advection.

Geen et al. (2018) also suggest that the monsoon regime transitions coincide with peaks in the horizontal advection and vortex stretching tendencies. As the ascending branch of the Hadley circulation and peak in divergent flow move polewards during NH summer, they move from a region with near zero absolute vorticity near the equator to a region of non-negligible absolute vorticity, resulting in a rapid increase in the negative vortex stretching. The link between the peaks in the tendencies and the dynamical regime transition is observable in our 10° simulation: these peaks are in fact observed immediately following June 21, after which the extratropical eddies' influence on the MOC is weakened and the MOC transitions into the AMC limit. While lagging the cross-equatorial jump of the ITCZ more than in the full aquaplanet simulation with 2 m MLD in Geen et al. (2018), these peaks do appear to coincide with the rapid growth in strength and poleward extent of the overturning cell.

Compared to the 10° simulation, the changes in horizontal advection and vortex stretching tendencies in the 30° simulation are relatively smooth and delayed (Fig. 2.12). During NH summer, the positive horizontal advection (Fig. 2.12a) over the winter Hadley cell has a greatly reduced magnitude compared to that in the 10° simulation (Fig. 2.11a), because of a much weaker MOC (compare Fig. 2.11c to Fig. 2.12c). The region of negative vortex stretching during NH summer also ex-

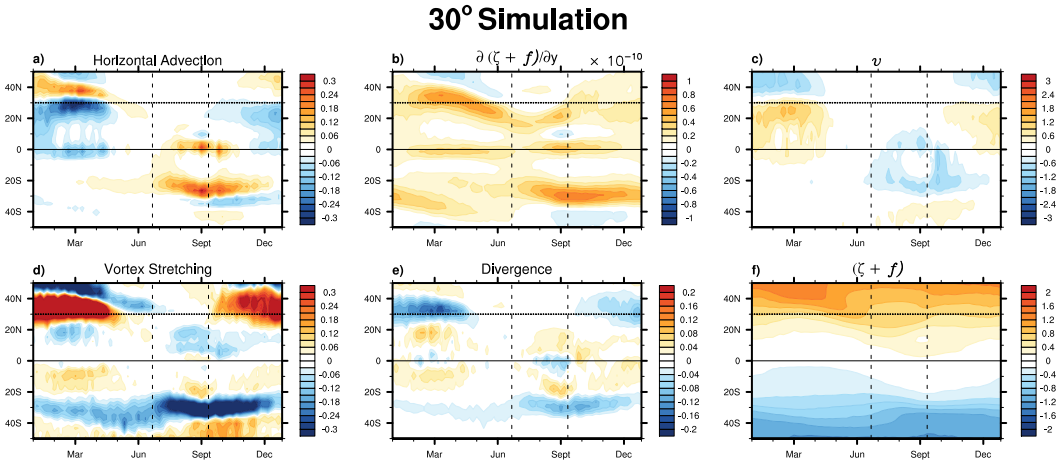

Figure 2.12: As in Fig. 2.11, but from the 30° simulation and contour intervals: a) 0.03 day^{-2}, b) 0.1 $\times$ 10^{-10} m^{-1} s^{-1}, c) 0.3 m s^{-1}, d) 0.03 day^{-2}, e) 0.02 day^{-1}, and f) 0.2 day^{-1}.

tends less polewards and is less strongly negative in the 30° simulation (Fig. 2.12d) than that in the 10° simulation (Fig. 2.11d). These are results of a weaker and narrower winter Hadley cell in the 30° simulation, resulting in weaker horizontal divergence (Fig. 2.12e). Consequently, in the 30° simulation during NH summer the combined effect of the horizontal advection and vortex stretching terms (sum shown in Fig. 2.13b) does not reduce the absolute vorticity in the NH subtropics (Fig. 2.12f) as effectively as in the 10° simulation (Fig. 2.11f), confirming the slower transition into the AMC limit in this case. Additionally, at the start of NH summer there are no significant peaks or rapid changes in the horizontal advection and vortex stretching tendencies as observed in the 10° simulation, reflecting the more slowly evolving dynamics in the simulation with land confined to higher latitudes. This is also apparent in the very smooth evolution of the zero contour of the absolute vorticity (Fig. 2.11f). From the perspective of the vorticity budget, having land in the tropics enables the dynamical monsoon regime transition to occur on a rapid intraseasonal timescale by rapidly strengthening the divergent flow of the Hadley circulation as its ascending branch moves polewards to regions of non-negligible absolute vorticity, to quickly increase the magnitude of the vortex stretching term and of the horizontal vorticity advection, which efficiently reduce the magnitude of the absolute vorticity and decouple the circulation from the eddy momentum fluxes.

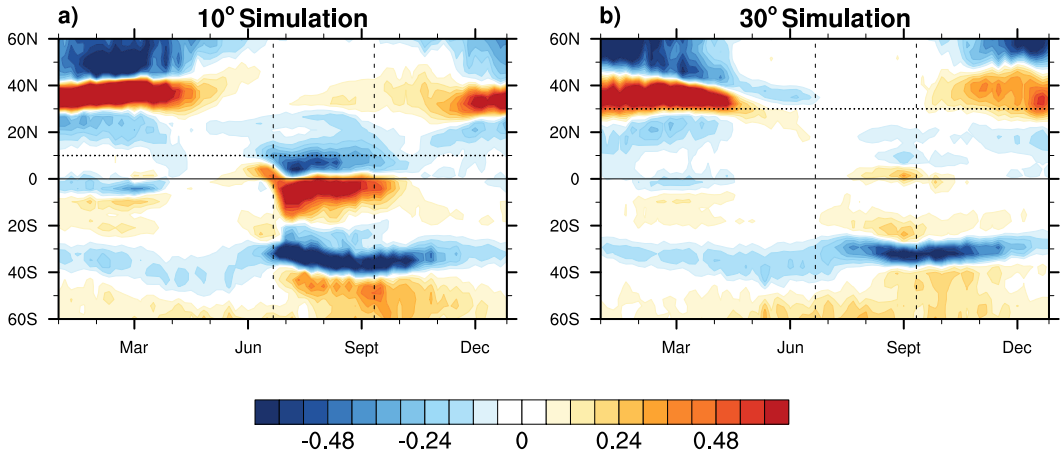

Figure 2.13: Total vorticity tendency (sum of the vortex stretching and horizontal advection tendencies from Figs. 2.11 and 2.12, contour interval 0.06 day^{-2}).

2.6 Discussion

The complementary interpretations of the dynamical monsoon regime transition presented in the previous section are tied together by the migration of the ascending branch of the Hadley circulation, both in terms of the direct effect of the eddy momentum fluxes on the streamfunction (Figs. 2.8, 2.9) and the seasonal evolution of absolute vorticity (Figs. 2.11, 2.12). A more poleward migration of the ascending branch widens the winter cell's poleward extent in both hemispheres and extends the region of prevalent upper-level easterlies within the tropical circulation into a broad latitudinal band in both the summer and winter hemisphere. This helps diminish the influence of the strength of the extratropical eddies originating in the winter hemisphere on the tropical circulation by shielding the circulation and weakening the EMFD at the cell center, and therefore enables the circulation to approach the AMC limit and become more thermally driven and rapidly strengthen. A more poleward migration of the ascending branch also brings the region of strongest upper-level horizontal divergence to a region of higher absolute vorticity in the NH and strongest horizontal advection to a region of large negative magnitude of absolute vorticity in the SH, since the positive meridional gradient of absolute vorticity in the NH increases with latitude. This in turn increases the vortex stretching and horizontal advection tendencies and results in a more efficient reduction of absolute vorticity across the entire winter Hadley cell and therefore a more AMC circulation. Regardless through which interpretation, once the circulation approaches the AMC limit and becomes more thermally driven, the cell can grow rapidly in strength and extent through two dynamical feedbacks — 1) by advecting lower MSE air in its

lower branch from the winter to the summer hemisphere, enabling the circulation to push the near-surface MSE maximum increasingly polewards and strengthen the temperature gradient, which by AM conservation requires a strengthening of the flow (Fig. 2.6); and 2) by also strengthening the upper-level easterlies in the winter hemisphere, effectively shielding the winter cell from the influence of the extratropical eddies and allowing it to more closely approach the AMC limit and further strengthen the upper-level easterlies (Figs. 2.9, 2.10) (Schneider & Bordoni, 2008).

It is through this key ingredient—a significant off-equatorial migration of the ascending branch of the Hadley circulation—that continental geometry appears to play an important role for the monsoon. By having more land or regions of low thermal inertia in the tropics, the distribution of the near-surface MSE can evolve rapidly, and the non-linear mechanisms described above help push its maximum far enough away from the equator into the subtropics for the circulation to grow rapidly in strength and extent. Only when these nonlinear mechanisms can operate on intraseasonal timescales, can a rapid monsoon onset be seen in our simulations.

We conclude this section with a brief remark on the temporal asymmetry between a rapid onset and a more gradual retreat that appears particularly evident in the simulations with continents extending to tropical latitudes. Such an asymmetry was also observed to occur in aquaplanet simulations reported by Geen et al. (2019), who attributed it to changes in SSTs induced by the wind-induced surface heat exchange (WISHE) feedback (Emanuel, 1987; Neelin et al., 1987). More specifically, they argue that WISHE slows the monsoon withdrawal through weak lower-level horizontal winds below the ITCZ, which keep the latent heat flux from the surface low and the SSTs warm below the ITCZ as it retreats to the winter hemisphere. Evidence of a slight temporal asymmetry between onset and withdrawal is also seen in the all-land (not shown) and all-ocean aquaplanet simulations (Fig. 2.2). It is however clear that a large hemispheric asymmetry in lower boundary thermal inertia gives rise to a more pronounced asymmetry in the monsoon temporal evolution: in the presence of a continent at tropical latitudes, the lower-level MSE can adjust rapidly as the circulation transitions into the monsoon regime. As the circulation retreats from the summer hemisphere and its ascending branch moves over the ocean, its large heat capacity instead prevents rapid MSE changes, hence slowing down the withdrawal phase. We believe that the hemispheric asymmetry in the lower boundary thermal inertia might be a more relevant mechanism than the WISHE feedback

for the temporal asymmetry of observed monsoons. More targeted simulations, in which for instance the WISHE feedback is disabled, will shed further light into these open questions.

2.7 Conclusion

Altogether, this study aims to understand how changing continental geometry can affect the spatial and temporal structure of the monsoonal precipitation. Five simulations are analyzed in an idealized aquaplanet GCM, where hemispheric asymmetry in thermal inertia is varied by using different continental configurations with zonally-symmetric land extending polewards from southern boundaries at 0°, 10°, 20°, 30°, and 40°. From studying the seasonal cycles of precipitation, near-surface MSE, mass streamfunction, and horizontal winds, we find that only the 0°, 10°, and 20° simulations with land extending into the lower latitudes have circulation and precipitation changes characteristic of observed monsoons. By breaking down the streamfunction into eddy and mean components and analyzing the seasonal cycle of the upper-level zonal momentum budget, our simulations suggest that different continental geometry can affect the spatial and temporal structure of the circulation and precipitation by affecting the circulation's ability to transition rapidly from a regime where the tropical circulation strength is controlled by eddy momentum fluxes to a regime where the strength is more directly controlled by energetic constraints. Having regions of low thermal inertia in the tropics enables this transition to occur on an intraseasonal scale; in contrast without land in the low latitudes, the circulation transitions are smoother and less similar to those seen in observed monsoons. This is because having land in the tropics allows the near-surface MSE maximum, and with it the ascending branch of the Hadley circulation, to adjust rapidly, allowing internal dynamical feedbacks to operate and to rectify the response to the smooth insolation forcing into a rapid onset.

That experiments with such idealized physics and configuration can replicate important features of the observed large-scale monsoons suggests the robustness of the underlying dynamics. It is however important to highlight the limitations in our study. First, in our simulations even land surfaces are completely saturated. In fact, at the beginning of the warm season, our simulations feature continental precipitation that is primarily driven by local evaporation, rather than moisture flux convergence. This is of course an artifact of our choice of a saturated continent and would be prevented to occur if a more realistic land surface hydrology scheme were used, with expected impacts on the timing of monsoon onset (Cook & Gnanade-

sikan, 1991; Peyrillé et al., 2016). Other limitations include the absence of important radiative feebacks, such as those associated with water vapor and cloud feedbacks, and the lack of albedo contrast between land and ocean, and any zonal asymmetry (Maroon & Frierson, 2016; Maroon et al., 2016). Additionally, we prescribe a zonally symmetric OHT, that neglects possible seasonality in the amplitude and direction of OHT in response to changing surface wind (Kang et al., 2018; Lutsko et al., 2019). Future work will be aimed at progressively including these effects, bridging the gap between our idealized simulations and those with comprehensive Earth System Models and observations.

2.8 Acknowledgements

This work was supported by the National Science Foundation (AGS-1462544) and the Caltech's Terrestrial Hazards Observation and Reporting (THOR) Center. We thank three anonymous reviewers, whose comments greatly improved the manuscript.

Chapter 3

RESPONSE OF MONSOON ONSET TIMING TO GREENHOUSE WARMING IN AN IDEALIZED GCM

Hui, K. L., & Bordoni, S. (2022). *Response of monsoon onset timing to greenhouse warming in an idealized GCM* [preprint].

3.1 Abstract

GCMs in the CMIP5 archive robustly project a delay in the timing of monsoon onset with warming. Several mechanisms have been proposed but their relative contributions remain debated. In this study, we explore the responsible mechanisms in a set of idealized aquaplanet slab-ocean simulations spanning a wide range of climates, from colder to warmer than the current climate, by varying the atmospheric longwave optical depth. While some existing explanations of delayed monsoon onset emphasize the role of the differing response of surface latent heat flux over land and over ocean, our aquaplanet simulations with uniform mixed-layer depth show similar phase delays. Using the angular momentum budget, we find evidence of a delay in the rapidity and timing of the regime transition of the tropical circulation from an eddy-driven into a more angular momentum conserving Hadley cell. By analyzing the atmospheric moist static energy budget, we demonstrate that as the climate warms, the atmospheric energy storage increases significantly during the spring and is able to compensate the changes in the thermal forcing. As a result, the circulation is able to respond to thermal forcing later in the season and the monsoon onset is delayed. Furthermore, we find that in extremely warm climates, the compensating effect of the energy storage is limited due to complex changes in the surface temperature seasonality. As a result, the monsoon onset delay with warming saturates.

3.2 Introduction

The tropical climate and annual cycle are dominated by the onset and retreat of the precipitation guided by the seasonal progression of monsoons and the Intertropical Convergence Zone (ITCZ). The precipitation cycle of all regional monsoons is characterized by a rapid summertime onset with abundant rainfall, followed by an arid winter, and associated circulation changes. Over half the world's population de-

pends on the water brought by the various monsoon systems, so understanding what determines important characteristics, such as monsoon precipitation onset timing, intensity, and spatial extent, are of utmost importance. Particularly understanding how these monsoon characteristics will evolve under global warming will pose an urgent and crucial question for future adaptation and mitigation.

As the tropical precipitation and circulation are closely coupled, changes in tropical precipitation with warming will depend on two main expected opposing effects – 1) the thermodynamical effect of more water vapor in the warming atmosphere as dictated by the Clausius-Clapeyron relation, and 2) the dynamical effect of a weakening of the convective mass flux with warming (Held & Soden, 2006). As the climate warms, how these two opposing effects interact with regional features such as continental geometry and topography will determine how precipitation will evolve in different tropical regions. Although it remains unclear how the two opposing thermodynamical and dynamical effects will affect tropical precipitation, some changes in tropical circulation, precipitation location and intensity, and precipitation onset timing have been well studied and predicted.

The Hadley circulation (HC) is responsible for the poleward energy transport from the tropics to the midlatitudes and determines the main location of tropical precipitation, since the ITCZ is collocated with the ascending branch of the circulation. In the global zonal mean, radiosonde data over the last few decades (Seidel & Randel, 2007) and the response to increasing concentrations of greenhouse gases simulated by comprehensive models (Lu et al., 2007; Staten et al., 2018) show an expansion in the width of the Hadley cell. In addition to a widening of the HC, based on thermodynamical arguments, as the lower-tropospheric water vapor increases robustly with warming, the convective mass fluxes within the tropics overall will decrease and the circulation strength will weaken (Held & Soden, 2006). Idealized general circulation model (GCM) simulations have also proved a useful tool in shedding light on circulation changes with warming. Although lacking a seasonal insolation cycle, under a large range of colder and warmer climates with perpetual equinox, idealized aquaplanet GCMs also show a widening HC with warming, with the tropical circulation strength maximizing in climates slightly colder than the current climate and tapering off in strength as the climate warms (Levine & Schneider, 2011).

There is large consensus between recent studies that a warmer climate will result in an increased amplitude of the tropical precipitation annual cycle (Chou & Lan, 2012; Chou et al., 2007; Geng et al., 2020; Huang et al., 2013; Lan et al., 2019). Within

climate change models from the Fourth Assessment of the Intergovernmental Panel on Climate Change (IPCC), although a weakening of the convective mass flux was predicted, in contrast the poleward horizontal vapor transport, and the associated evaporation minus precipitation ($E - P$) pattern, increased with increased lower-tropospheric water vapor with warming. This suggested a "wet-get-wetter" pattern in the future, since with warming more moisture will be converged, even without any change in the circulation (Held & Soden, 2006). Chou and Neelin (2004) proposed the "upped-ante"and "anomalous gross moist stability (GMS)" mechanisms, where within convective regions, the GMS is reduced due to increased atmospheric boundary layer (ABL) moisture with warming, resulting in further increased convection and precipitation within the convective region, further supporting the "wet-get-wetter" pattern. S.-P. Xie et al. (2010) proposed instead a "warm-get-wetter" mechanism, where the pattern of precipitation change follows the pattern of sea surface temperature (SST) warming instead of the pattern of current precipitation, as implied by the "wet-get-wetter" pattern. Taking simulated clouds into account, simulations within the Coupled Model Intercomparison Project Phase 5 (CMIP5) archive showed a strengthening and tightening of the tropical circulation ascending branch with warming due to high cloud area shrinkage, giving rise to increased tropical precipitation within the ITCZ (Su et al., 2017). Several studies also have looked more specifically at changes in the amount of summertime monsoonal precipitation with warming. Within CMIP5 models, Kitoh et al. (2013) showed monsoonal precipitation will increase with warming due to increases in moisture convergence and evaporation and Wang et al. (2014) showed that increases in horizontal thermal contrast (warmer land vs. cooler ocean and warmer northern hemisphere (NH) vs. cooler southern hemisphere (SH)) would also increase monsoonal rainfall.

Ultimately, through the coupling of the tropical circulation and precipitation, the annual cycle of tropical precipitation is driven by solar insolation. However, factors, which vary largely over different monsoon regions, such as continental geometry and surface properties and fluxes over both land and ocean, determine the exact temporal evolution. While the GCMs in the CMIP5 and CMIP6 archives robustly project a delay in the timing of monsoon onset with warming (Biasutti & Sobel, 2009; Dwyer et al., 2014; Song et al., 2018; Song et al., 2021), a more unified perspective is still needed to connect the various proposed mechanisms. Dwyer et al. (2014) showed that within CMIP5 models, when forced with increased greenhouse gases, the trends in the amplitude and phase of the precipitation annual cycle could be produced by simulations with annual mean and spatially uniform SST warming, suggesting that

annual SST mean warming can explain most of the amplitude increase and phase delay in tropical precipitation observed with warming. Using the "upped-ante" mechanism (Chou & Neelin, 2004), Seth et al. (2013) showed that within CMIP5 models with warming, enhanced convective barriers in the American and African monsoon regions led to monsoon onset delays. Substantial work in the past decade has developed the energetic framework, which relates shifts in the ITCZ position to changes in the atmospheric energy budget (Biasutti et al., 2018; Boos & Korty, 2016a; Frierson et al., 2013; Kang et al., 2008; Schneider et al., 2014). Key to this framework is that the region of maximum moist static energy (MSE) flux divergence is collocated with the region of maximum net energy input (NEI) into the atmospheric column. Since higher MSE is maintained in the upper atmosphere, the upper diverging branches of the HC diverge energy from the tropics polewards. The location where the upper branches of the HC diverge is also the location of maximum tropical precipitation or the ITCZ due to intense ascent of hot moist tropical air by the ascending branch of the HC. Using this energetic framework, recent work has related interseasonal changes with warming in the NEI and effective atmospheric heat capacity C_A between NH spring and summer to changes in the timing of the monsoon onset (Song et al., 2018; Song et al., 2020). Song et al. (2018) showed within CMIP5 models that as the climate warms, the latent energy (LE) demand increases in the spring in the NH, which requires the ascending branch of the HC, and with it the ITCZ, to stay longer in the SH to transport energy into the NH to keep up with the LE demand. As a result, the cross-equatorial jump of the ITCZ associated with the monsoon onset is delayed with warming. Adding upon the work of Dwyer et al. (2014), Song et al. (2018) performed the energetic framework analysis not only on CMIP5 experiments with uniform SST warming, but also those with SST warming pattern. They found monsoon onset delay with warming in both experiments with uniform SST warming and SST warming pattern, suggesting annual mean SST warming cannot fully explain the onset delay with warming and that SST warming pattern also has contributions. Using the same energetic framework, Song et al. (2021) found robust delays in tropical precipitation over northern tropical land and the Sahel within CMIP5 and CMIP6 models, and attributed the delay to changes from external forcing, mostly due to increasing greenhouse gases and decreasing aerosol.

While different mechanisms have been proposed for the response of the tropical precipitation annual cycle with warming, a more unified view using both the energetic and dynamical perspectives may prove useful. The majority of the studies focusing

on the phase delay of monsoonal precipitation with warming have been performed using comprehensive models, which can complicate determining the relative importance of the responsible mechanisms discussed above. In this study, we explore the responsible mechanisms of monsoon onset delay with warming using instead a set of idealized aquaplanet GCM simulations spanning a wide range of climates, from much colder to much warmer than our current climate, by varying only the atmospheric longwave optical depth. By using aquaplanet GCMs with a uniform lower boundary, we remove the effect of land-sea contrast, which enables us to focus on just the effect of a warmer climate. In this way, we hope to distinguish leading order causes of monsoon onset delay with warming, even in the absence of continent, in contrast to some mechanisms proposed using the CMIP5 archive (Seth et al., 2013). Taking advantage of our much larger range of simulated climates compared to CMIP5, we aim to explore the highly nonlinear relationship between temperature and moisture on the balance between the circulation strength and amount of moisture, which determines the resulting moisture flux convergence (MFC) performed by the tropical circulation and the amount and location of precipitation, and also affects the monsoon onset timing through changes in the atmospheric energy budget. Monsoon onset can also be interpreted through a dynamical perspective as a regime switch between two regimes that differ in the amount of influence the extratropical eddies have on the tropical circulation using the angular momentum (AM) budget (Bordoni & Schneider, 2008; Schneider & Bordoni, 2008). The relative influence of the extratropical eddy momentum flux divergence (EMFD) on the tropical circulation has been explored in idealized aquaplanet GCM work under climate change under perpetual equinox (Levine & Schneider, 2011), but not yet with the inclusion of an insolation seasonal cycle where the monsoon dynamical transition may be observed. Therefore, in this work, in addition to studying monsoon onset timing changes due to changes in the atmospheric energy budget with warming, we will also analyze our simulation output from a dynamical lens to better connect the energetic changes to changes in the circulation and associated precipitation throughout the annual cycle. The idealized GCM and simulations used in this study, as well as the methods and theoretical frameworks used for analysis, are described in Section 3.3. Section 3.4 focuses on the seasonal cycles of precipitation and the circulation, comparing the results over the large range of simulated climates and connecting changes in precipitation and the associated circulation. Section 3.5 interprets the simulated changes in monsoon onset timing with climate warming from the energetic perspective using the energetic framework. And finally, discussion and conclusions follow in Section

3.6.

3.3 Methods and Tools

Idealized GCM and Simulations

The simulations used for this study were produced using a moist idealized aquaplanet GCM based on the Geophysical Fluid Dynamics Laboratory (GFDL) Flexible Modeling System (FMS) (Frierson et al., 2006; O'Gorman & Schneider, 2008), which solves the primitive equations of motion on a sphere with Earth's radius. This model has been used extensively to study many aspects of tropical and extratropical circulations and their response to climate changes, and we refer to previous work for a more detailed description (Bordoni & Schneider, 2008; Hui & Bordoni, 2021; Levine & Schneider, 2011, 2015; O'Gorman & Schneider, 2008; O'Gorman & Schneider, 2009).

Here, we want to study the response of monsoonal circulations to radiative perturbations induced by greenhouse gases in the simplest possible setting. To this aim, we use a completely uniform mixed layer ocean with specified depth of 5 m as lower boundary and a prescribed zonally symmetric and time invariant Q flux (e.g., Merlis et al., 2013a). As shown in previous studies (Geen et al., 2018, 2019; Hui & Bordoni, 2021; Zhou & Xie, 2018), such a shallow mixed layer allows for rapid monsoon-like transitions in the tropical circulation and precipitation patterns even in the absence of land-sea contrast. In fact, aquaplanet monsoons over a shallow mixed layer ocean have allowed for substantial progress in the theoretical understanding of monsoons (Geen et al., 2020) and here we study the response of such elemental monsoons to climate change.

A two-stream gray radiation scheme is used where the optical depth τ is prescribed as a function of latitude and pressure (O'Gorman & Schneider, 2008). The reference simulation produces a climate that resembles in many aspects present-day Earth's climate, with a global mean surface temperature of 288.6 K. A wide range of climates is generated by rescaling the optical depth by a factor α such that $\tau = \alpha\tau_{ref}$ (Kaspi & Showman, 2015; Levine & Schneider, 2015; O'Gorman & Schneider, 2008). When $\alpha < 1$ (> 1), the resulting simulated atmosphere is optically thinner (thicker) than in our current climate and results in a colder (warmer) climate than that in present day. Although a diurnal cycle is not included, the GCM is forced by a seasonal cycle of insolation with a 360-day Julian year that uses realistic Earth-like values of obliquity and solar constant of 23.5° and 1360 W m^{-2} respectively, but zero eccentricity.

Table 3.1: Atmospheric optical depth multiplication factor abs used for each simulation, and resulting global annual mean surface temperatures (T_s) and precipitation amounts (P).

Simulations		
α	T_s (K)	P (mm day^{-1})
0.2	261.7	0.81
0.3	267.8	1.43
0.4	272.7	2.01
0.5	276.9	2.59
1.0	288.6	4.15
2.0	299.7	5.26
4.0	309.6	5.88
6.0	314.9	6.05

The GCM includes an active hydrological cycle, where precipitation can form by either large-scale condensation or convection following a simplified Betts-Miller convection scheme as in Frierson (2007). Since precipitation is assumed to fall out immediately, there is no liquid water or ice in the atmosphere and hence no clouds. However, we use a spatially-uniform surface albedo of 0.38 to compensate for the lack of clouds. With these simplifications, this GCM does not account for important climate feedbacks such as surface albedo, cloud, or radiative water vapor feedbacks, however, the tropical and extratropical circulations and their interactions and impact on the hydrological cycle are still well simulated. Every simulation was performed at T42 horizontal spectral resolution with 30 vertical levels and run for 25 years, with data from the last 15 years used in the analyses shown below. All fields presented in this study are global zonal averages since our model uses a zonally-symmetric setup.

For this study, a series of eight simulations were performed to simulate a large range of climates. The values of longwave optical depth rescaling factor α prescribed and the resulting global annual mean surface temperatures (T_s) and daily precipitation rates (P) are shown in Table 3.1. By varying the optical depth rescaling factor from $\alpha = 0.2$ to $\alpha = 6.0$, we produce a large range of climates ranging from extremely cold and dry to very hot and moist, with T_s ranging from 261.7 to 314.9 K and P ranging from 0.81 to 6.05 mm day^{-1}. Overall, global mean precipitation increases as the climate warms (Fig. 3.1a) at a rate of $\sim 2.5\%$ K^{-1} (Fig. 3.1b), consistent with previous findings and energetic arguments on constraints on global

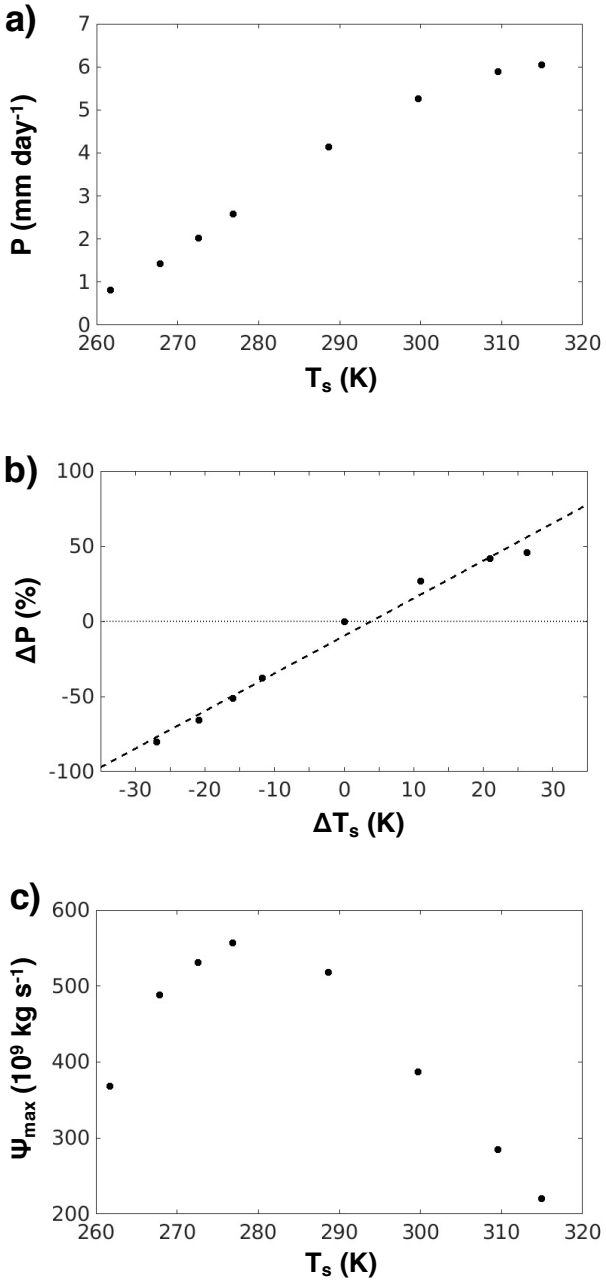

Figure 3.1: Panel a) contains the scatter plot of global annual mean daily precipitation rate (P) versus global annual mean surface temperature (T_s) from all eight simulated climates. Panel b) shows the scatter plot of the percentage change in global mean precipitation versus the global mean change in surface temperature. The dashed line reveals the linear fit of ΔP to ΔT, which increase at a rate of 2.5% K^{-1}. Panel c) contains the scatter plot of absolute maximum streamfunction (Ψ_{max} in kg s^{-1}) versus the global annual mean surface temperature (T_s in K).

mean precipitation (IPCC 6 2021, Held & Soden, 2006; O'Gorman et al., 2012). More specifically, precipitation increases with surface temperature at a rate of 3.0% K^{-1} from the coldest to current climate and a rate of 1.3% K^{-1} across the three warmest climates, as estimated from a two-phase linear regression, consistent with studies of similarly idealized warming simulations over a large range of climates (O'Gorman & Schneider, 2008). The extreme range of simulated climates also show observable changes in the monsoonal circulation strength, defined as the extremal value of the cross-equatorial winter Hadley cell in the solstice season. Figure 3.1c shows the absolute maximum streamfunction (Ψ_{max}) during Northern hemisphere (NH) summer versus the global mean surface temperature. The circulation strength peaks in climates similar to and slightly colder than the current climate, consistent with literature that focus on the annual mean (Levine & Schneider, 2011; O'Gorman & Schneider, 2008; Schneider et al., 2010). We will further investigate the seasonal changes in precipitation and circulation structure and strength in Section 3.4.

Monsoon Onset and Retreat Metrics

Within literature, there are various methods used to calculate monsoon onset based on different metrics and theories (Bombardi et al., 2019; Walker & Bordoni, 2016; Zhou & Xie, 2018). In this study, we quantitatively analyze the changes in monsoon onset and retreat timing with a warming climate using the monsoon timing metric developed by Walker and Bordoni (2016) (hereafter WB16). This method has the advantage compared to other metrics of capturing changes in the large-scale overturning circulation that are directly associated with changes in net precipitation (that is, the difference between precipitation and evaporation) using the large-scale atmospheric moisture budget:

$$\text{MFC} = -\int_0^{p_s} \nabla_p \cdot (\mathbf{u}q)\frac{\mathrm{d}p}{g} = P - E + \frac{\partial w}{\partial t}. \tag{3.1}$$

The MFC is calculated as the vertically-integrated horizontal MFC, $\nabla_p \cdot ()$ represents the horizontal divergence in pressure coordinates, $\mathbf{u} = (u, v)$ is the horizontal wind vector, q is specific humidity, P is the precipitation rate, E is the evaporation rate, g is the gravitational acceleration, and $w = \int_0^{p_s} q\frac{\mathrm{d}p}{g}$ is the total precipitable water or the moisture storage. Following this method, we calculate the cumulative moisture flux convergence (CMFC) across the season over a representative region (here taken as the latitudinal band between 10° and 30°) and detect the change point of its two-phase linear regression. Within NASA's Modern-Era Retrospective analysis for Research and Applications, Version 2 (MERRA-2) observations data for the years

1980-2015, Walker and Bordoni (2016) showed that within our current climate in the South Asian Monsoon region, the storage $\partial w/\partial t$ is negligible. With negligible storage, the MFC primarily balances net precipitation, and therefore the change point detects onset as the time at which net precipitation switches from negative to positive (and withdrawal as the opposite transition). However, this study analyzes a much larger range of extreme climates. Considering the highly non-linear relationship between temperature and moisture, one might expect the extremely warm climates to experience non-negligible changes in $\partial w/\partial t$. For this reason, we additionally calculate the monsoon onset and retreat timing using the same change point method, but instead using the cumulative net precipitation $(P-E)$. In this way, we can observe and quantify any differences in our monsoon onset and retreat timing calculation method due specifically to storage changes.

ITCZ Position

Within the simulations used for this study, the precipitation distributions often become doubly peaked during different times of the season, which results sometimes in rapid jumps in the latitude of maximal precipitation between hemispheres or between the two branches of the double ITCZ. To avoid this issue and reduce grid dependence, when studying seasonal variations in the latitudinal position of tropical precipitation, we follow the method presented in Adam et al. (2016) and calculate the ITCZ position as

$$\phi_I = \frac{\int_{30^\circ\mathrm{S}}^{30^\circ\mathrm{N}} \phi \left(P\cos\left(\phi\right)\right)^n \mathrm{d}\phi}{\int_{30^\circ\mathrm{S}}^{30^\circ\mathrm{N}} \left(P\cos\left(\phi\right)\right)^n \mathrm{d}\phi}, \tag{3.2}$$

where ϕ is the latitude, P is the zonal mean precipitation, and n is a smoothing parameter. This equation represents a weighted average, where $n = 1$ yields ϕ_I equal to the precipitation centroid (Frierson & Hwang, 2012) and large n converges to ϕ_I at the latitude of maximal precipitation. We use $n = 5$ since the latitudinal extent and timing of the seasonal transitions of the resulting ϕ_I matched the calculated precipitation maximum locations and monsoon onset and retreat timings well.

While we define the ITCZ position as ϕ_I in Eq. (3.2) to study the general trends in the seasonal migrations of the ITCZ with climate warming, we recognize that one single parameter is often not able to fully capture the complexities of all the simulated precipitation distributions (Popp & Lutsko, 2017). Therefore, when we study the changes in solstitial mean ITCZ across the different simulated climates, we additionally calculate the ITCZ position following several other ITCZ metrics that exist in the literature to relate changes in the ITCZ location to changes in the

circulation or energetics following various theoretical frameworks. These include: the latitude of maximal precipitation and the latitude of maximal low-level moist static energy (MSE_{max}, Privé & Plumb, 2007a). Due to the wide range of resulting timings of monsoon onset and retreat across the simulations, the solstitial mean ITCZ metrics are calculated over 15-pentad time intervals centered around the time of maximal poleward excursion.

Angular Momentum Budget

Recent work has shown that within idealized aquaplanet simulations, the rapid monsoon onset can be interpreted as a switch between two dynamical regimes that differ in the relative influence the extratropical eddy momentum fluxes have on the strength of the tropical overturning circulation (Bordoni & Schneider, 2008; Schneider & Bordoni, 2008). The two dynamical regimes can be understood by looking at two limits of the zonal momentum budget, which within the upper branch of the Hadley circulation, can be approximated as

$$(f + \overline{\zeta})\overline{v} = f(1 - R_o)\overline{v} \approx \mathcal{S}, \tag{3.3}$$

with planetary vorticity $f = 2\Omega \sin\phi$, relative vorticity $\overline{\zeta} = -\partial\overline{u}/\partial y$, meridional wind v, local Rossby number $R_o = -\overline{\zeta}/f$, and transient eddy momentum flux divergence (EMFD) $\mathcal{S} = \partial\overline{u'v'}/\partial y + \partial\overline{u'\omega'}/\partial p$, where u is the zonal velocity, ω is the vertical velocity, p is pressure, and $(\cdot)' = (\cdot) - \overline{(\cdot)}$ is the deviation from the time mean. (While Cartesian notation is used here for simplicity, both the model and all our calculations are done in spherical coordinates). R_o measures how far (small R_o) or close ($R_o \to 1$) the Hadley circulation is from the angular momentum conserving (AMC) limit (Schneider, 2006). In the limit of $R_o \to 0$, the strength of the mean meridional flow ($\overline{v}$) is directly and linearly tied to the EMFD. In the limit of $R_o \to 1$, the circulation approaches the AMC limit and responds more directly and nonlinearly to energetic constraints (Held & Hou, 1980; Lindzen & Hou, 1988). Bordoni and Schneider (2008) and Schneider and Bordoni (2008) demonstrated that in idealized simulations under our current climate with uniform MLD, the timing of the rapid monsoon transition is coincident with the dynamical regime transition from an eddy-driven circulation to a more AMC circulation. In a previous paper (Hui & Bordoni, 2021), we showed how a similar transition occurs over idealized zonally symmetric continents if the equatorward coastal boundary extends to tropical latitudes. In Section 3.4, we utilize the AM budget analysis to investigate whether changes in the monsoon onset timing can be related to observed

changes in the relative influences of the mean and eddy components on the total circulation strength.

Energetic Framework

The atmospheric energy budget has been shown to provide powerful constraints on tropical precipitation and has allowed for significant advances in the understanding of its mean position and response to perturbations on different time scales in the past decade or so.

The energy budget for an atmospheric column states that the divergence of the meridional atmospheric heat transport (AHT) performed by the tropical circulation is balanced by the difference between the net energy input (NEI) into the column from the top and bottom and the energy stored in the atmospheric column (e.g., Kang et al., 2008; Neelin & Zeng, 2000):

$$\frac{\partial}{\partial y}\langle \mathrm{AHT} \rangle = F_{net} - \frac{\partial \langle \mathscr{E} \rangle}{\partial t}, \tag{3.4}$$

where $F_{net} = F_{TOA} - F_{SFC}$ is the NEI, with F_{TOA} equaling the net radiation at the top of the atmosphere (TOA) into the atmospheric column and F_{SFC} equaling the net outgoing energy flux leaving the atmosphere into the surface. AHT is the vertically integrated meridional moist static energy (MSE) flux $\langle vh \rangle$, where $h = c_p T + gz + L_v q$ is the MSE, with specific heat at constant pressure c_p, temperature T, latent heat of vaporization L_v, and $\langle\ \rangle$ represents a vertical integral over the entire atmospheric column. $\partial \langle \mathscr{E} \rangle / \partial t$ is the time tendency of the sum of the dry enthalpy and latent energy $\mathscr{E} = c_p T + L_v q$, and represents the energy that is stored in the atmospheric column, which over long time averages is approximately 0. One fundamental assumption in the energetic framework is that the ascending branch of the Hadley cell is, on long temporal means, approximately co-located with the latitude where the column-integrated atmospheric energy transport (AET) vanishes, also known as the energy flux equator (EFE) (Kang et al., 2009; Kang et al., 2008), and where the meridional divergence of AHT maximizes. Given that the Hadley cell ascending branch also coincides with the region of maximal precipitation or the ITCZ, these arguments provide a powerful connection between the energetics, circulation, and ITCZ position. These arguments neglect the possible role of the atmospheric energy storage, which can be significant at sub-annual timescale important for seasonal transitions. In Section 3.5, we analyze and interpret the changes in monsoon onset timing with a warming climate from the energetic framework perspective, following

similar analysis as in Song et al. (2018). Importantly, when seasonal transitions are considered, the change in the storage term plays a fundamental role.

3.4 Seasonal Cycle

We begin analyzing the effects of climate change on the timing and structure of the monsoonal precipitation and circulation over the whole seasonal cycle. As done in previous work on aquaplanet monsoons, we identify them as subtropical convergence zones embedded in the ascending branch of cross-equatorial Hadley cells. In this section, we review the simulated seasonal cycles of the precipitation and the circulation and connect the simulated changes with changes in the dynamics via the AM budget. Since a zonally and hemispherically symmetric uniform lower boundary was used for each simulation, the simulation results are symmetric between the NH and SH. Here, for clarity, we will focus on the seasonal changes in precipitation and the circulation in the Northern Hemisphere (NH).

Precipitation Seasonal Cycle

Figure 3.2 shows the seasonal cycle of precipitation from each of the eight simulated climates. Across all simulated climates, monsoon-like convergence zones form in the subtropics of the summer hemisphere and move rapidly into the opposite hemisphere at the end of the warm season. A secondary convergence zone is also seen on the summer side of the equator. Consistent with results shown in Figure 3.1, there is an an overall increase in precipitation over the entire seasonal cycle as the climate warms. A few qualitative additional trends are observed — the precipitation appears to become more sharply peaked, the double ITCZ structure becomes more pronounced, the ITCZ moves further poleward, and the monsoon onset delays. Are these observations quantifiable? Below, we look at and quantify these trends in more detail.

ITCZ Position

Figure 3.3 shows the NH summertime mean values of the ITCZ metrics covered in Section 3.3: the latitude of maximum precipitation (ITCZ), the latitude of the maximum low-level MSE, and the precipitation weighted centroid (Adam16). All of the solstitial mean ITCZ metrics show a clear increase in poleward extent with warming, increasing on average 7.3° from the coldest to the warmest climate.

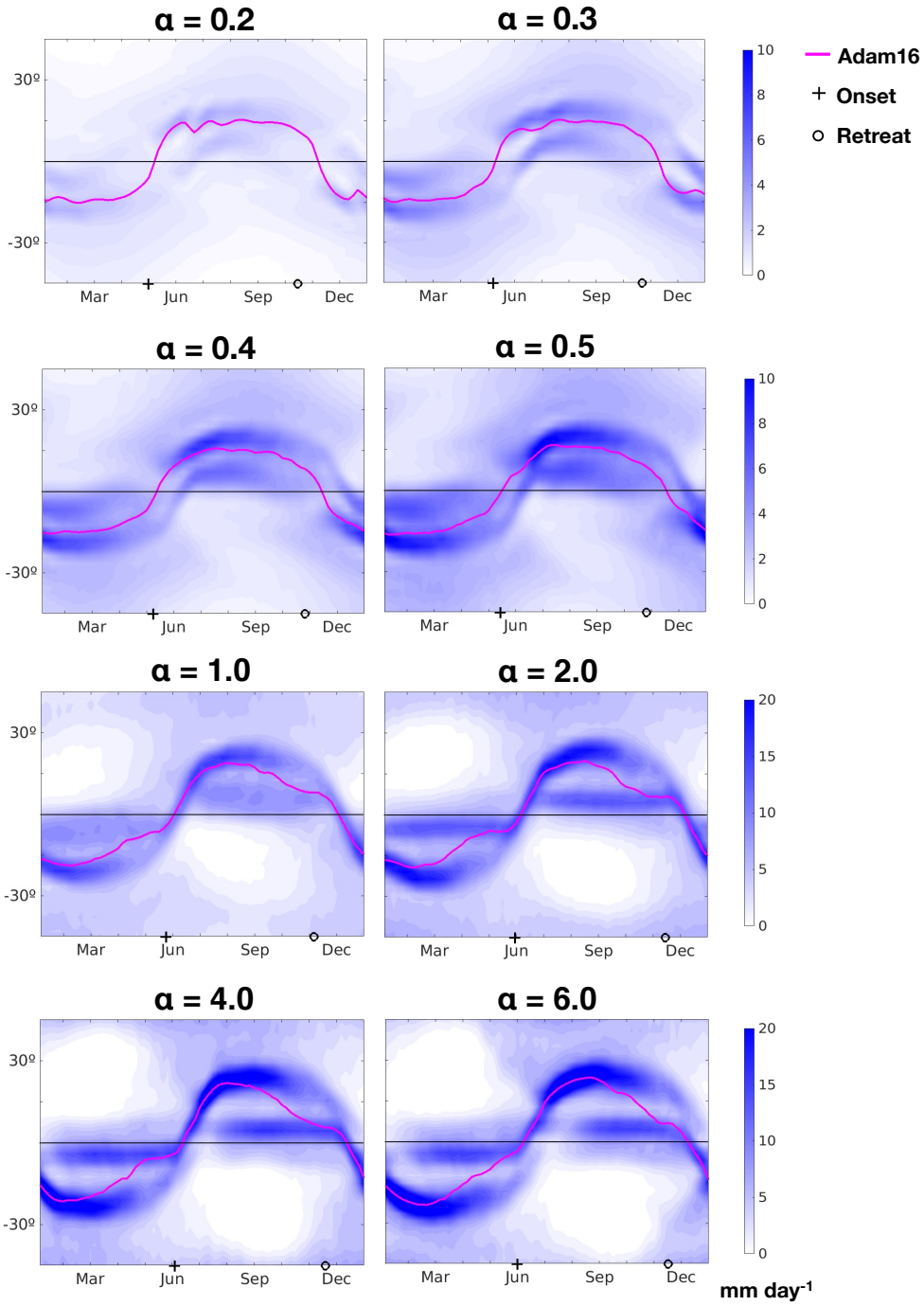

Figure 3.2: The seasonal cycles of precipitation from the coldest (top left) to warmest (bottom right) simulated climates are shown in the blue contours (contour interval: 0.25 mm day^{-1} ($\alpha \leq 0.5$) and 1.0 mm day^{-1} ($\alpha \geq 1.0$)). The magenta line tracks the precipitation weighted centroid following Eq. (3.2) with $n = 5$. Along the time axis, the monsoon onset and retreat indices calculated following the WB16 method using the CMFC are marked with plus signs and open circles, respectively.

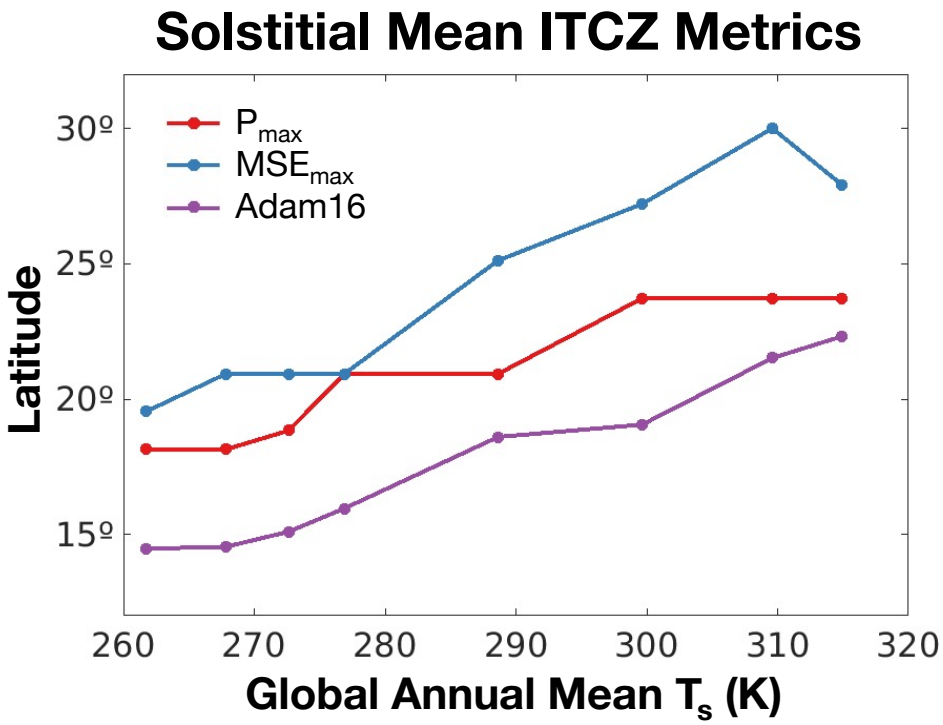

Figure 3.3: Solstitial NH summer mean ITCZ position (red), near-surface MSE maximum (blue), and precipitation weighted centroid from Adam et al. (2016)a (purple) versus the global annual mean surface temperature from each simulation.

Double ITCZ Structure

In addition to changes in the seasonal mean ITCZ position, the precipitation spatial distribution shape also evolves with warming. During the solstitial seasons, within all the simulations the precipitation in the summer hemisphere features a doubly peaked distribution, with one more poleward branch and one more equatorward branch. However, the relative strengths between the two peaks vary across the climates. We track the precipitation absolute maximum (magenta) and the equatorward precipitation maximum (green) in Figure 3.4, where the equatorward maximum is calculated by finding the precipitation local maximum between 10°S and 10°N. In the colder climates, the two precipitation peaks tend to be more distinct from each other in the beginning of the summer, transitioning into the summer hemisphere at different times, with the more poleward arm jumping across the equator earlier than the more equatorward arm, and in the later summer months becoming more weighted towards the poleward arm (top two rows of Figs. 3.2 and 3.4). As the climate warms, these two ITCZ branches tend to merge in early NH summer crossing the equator

together, and instead become heavily weighted towards the equatorward branch in the later summer months (bottom two rows of Figs. 3.2 and 3.4). A closer look at the monthly evolution of precipitation distributions and comparisons with the corresponding distributions of surface temperature gradient and mass streamfunction reveal that the two precipitation peaks are driven by different dynamics. The distributions of precipitation during the first day of each month from May to September for the $\alpha = 0.2, 1.0$, and 4.0 climates are shown in Fig. 3.5. The corresponding mass streamfunctions for those time slices and climates are depicted in Fig. 3.6. The absolute precipitation maximum, which mostly is co-located with the poleward branch of the double ITCZ, is associated with the ascending branch of the Hadley cell and is caused by the MFC driven by the broad overturning circulation (compare poleward precipitation maximum in Fig. 3.5 to ascending branch of Hadley cell in Fig. 3.6). In contrast, the more equatorward branch of the double ITCZ is caused by boundary layer (BL) dynamics described in Pauluis (2004). More specifically, in the deep tropics, where the Coriolis parameter is small, in regions of near-surface temperature gradients that are too weak to sustain the required meridional flow, the flow must jump above the BL to cross that region. This causes local ascent and local precipitation. This is observed in Fig. 3.4, where during summer the location of the equatorward precipitation maximum (green line) is co-located with near-equatorial weak near-surface temperature gradients, and in Fig. 3.6 where once the Hadley cell has become broad and cross-equatorial, a region of vertical motion is observed in the BL near or slightly poleward of the corresponding equatorward precipitation maximum (Fig. 3.5). While our focus in this study is mainly on the more poleward branch of the double ITCZ, since we consider the monsoonal precipitation to be the precipitation caused by the MFC by the large-scale tropical circulation, it is important to understand the distinction between the two ITCZ arms and their underlying dynamics and their differing response to warming in relation to the monsoon onset, as we discuss in more detail in the next subsection.

Monsoon Onset Delay

Qualitatively, the ITCZ appears to transition across the equator into the summer hemisphere earlier for colder climates than for warmer climates. To quantify this delaying trend, the monsoon onset and retreat indices are calculated as in WB16, and are summarized in Table 3.2 and marked in Figs. 3.2 and 3.7. We quickly note here that using both the cumulative MFC and net precipitation resulted in similar onset and retreat timing results, so while the changes in moisture storage

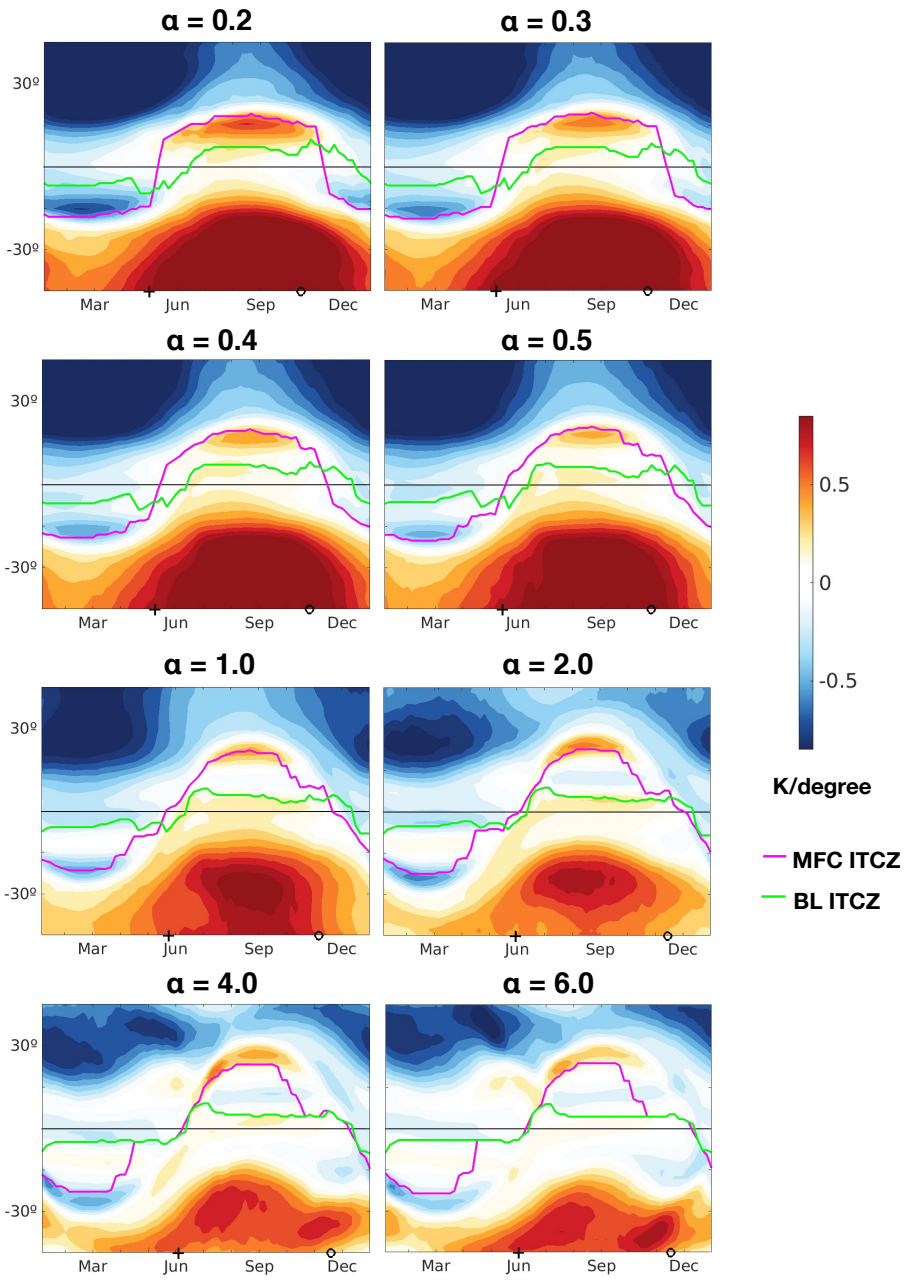

Figure 3.4: The seasonal cycles of the near-surface (σ = 0.9633) temperature gradient (K per degree latitude) from the coldest (top left) to warmest (bottom right) simulated climates are shown in the color contours (contour interval: 0.1 K per degree latitude). The magenta line tracks the latitude of the absolute maximum in precipitation that we associate with the moisture flux convergence driven by the large-scale overturning circulation. The green line tracks the latitude of the local maximum in precipitation between 10°S and 10°N, which we associate with boundary layer dynamics. Both lines have been smoothed by calculating the moving mean over a sliding window of five pentads centered around the current pentad. The onset and retreat indices are marked, as in Fig. 3.2.

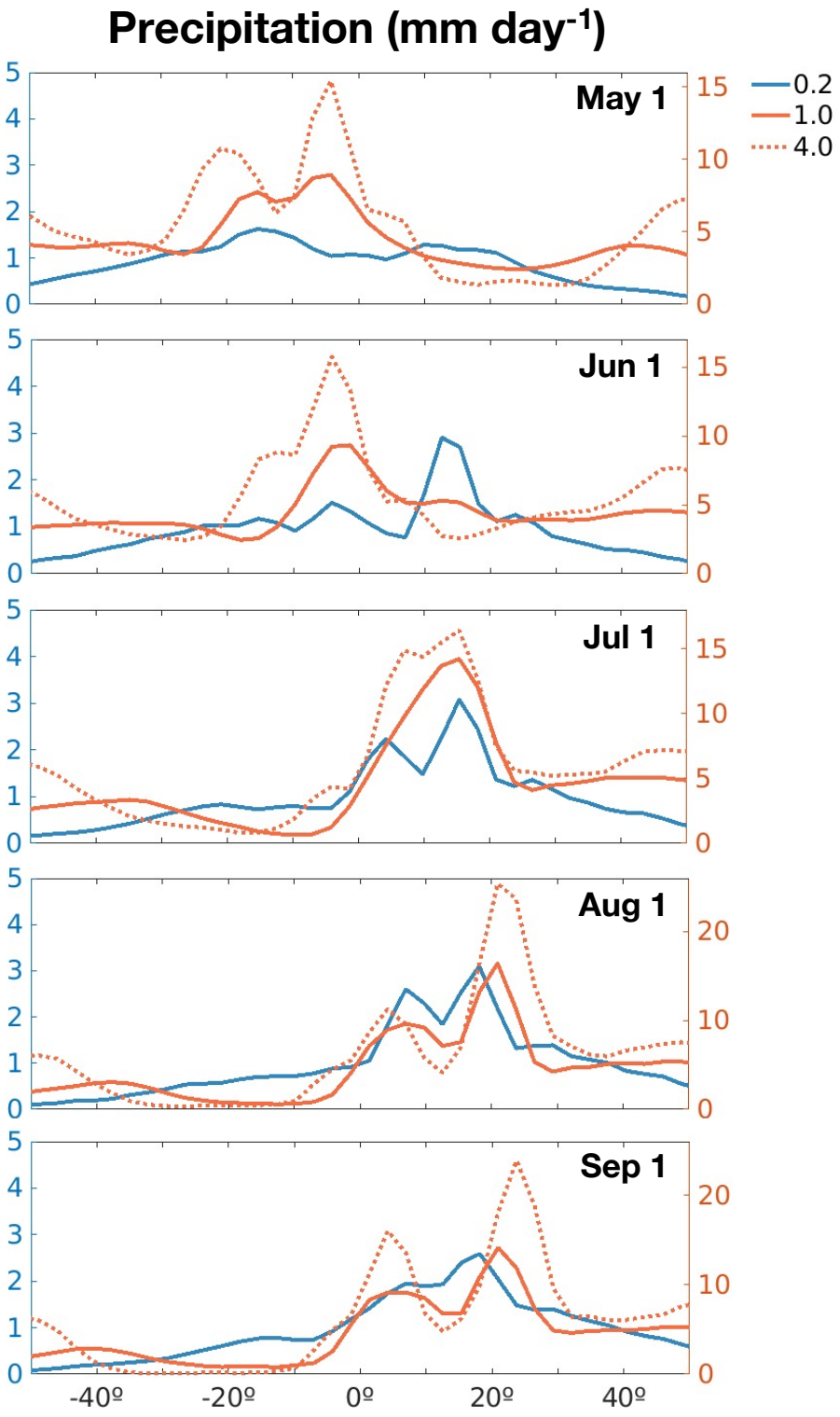

Figure 3.5: Three-pentad mean distributions of precipitation centered around May 1, June 1, July 1, August 1, and September 1 (top to bottom) from the climates with $\alpha = 0.2$ (blue, left y-axis), 1.0, and 4.0 (orange solid and dotted, respectively, right y-axis).

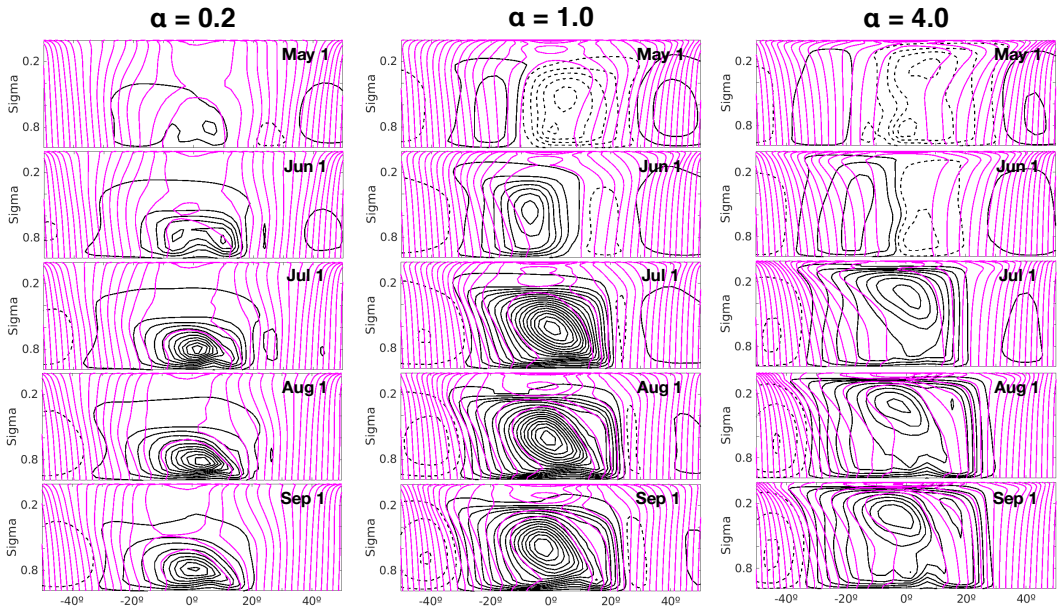

Figure 3.6: The mass streamfunction in black (counterclockwise in solid, clockwise in dashed; contour interval: 30×10^9 kg s^{-1}) and angular momentum contours in magenta (contour interval: $\Omega a^2/30$) from the climates with $\alpha = 0.2$ (left column), 1.0 (middle column), and 4.0 (right column). Each plot contains the three-pentad mean distributions centered around first day of each month from May to September (shown in chronological order from top to bottom row).

may affect the seasonal transitions of the precipitation and circulation, they likely do not affect the accuracy of our onset and retreat calculation method. We observe a clear monotonic delaying trend in monsoon onset as the climate warms, with a delay of one month from May 1 to June 1 between the coldest and warmest climates. A similar one month delay in retreat timing from October 16 to November 16 is observed, as expected from an aquaplanet covered with a uniform surface, where the monsoon transitions into the SH during SH summer experience similar delays with warming. Interestingly, the monsoon onset (and retreat) delay with warming is clear, even without the presence of land-ocean contrast, raising the question of relevant mechanisms.

Table 3.2 and Fig. 3.7 show an additional observation of interest. Although a clear delay in onset is observed comparing the coldest to warmest simulated climates, the monsoon onset delay appears to saturate in the warmest climates. From the climates colder than the current climate to the climate just warmer ($\alpha = 0.2$ to 2.0), the monsoon onset shows a monotonic delay from May 1 to June 1. However, across the warmest simulated climates ($\alpha = 2.0, 4.0$, and 6.0), the monsoon onset timing

Table 3.2: Dates of monsoon onset and retreat calculated with the WB16 method using the cumulative MFC (CMFC), and similarly with the cumulative net precipitation (cumulative $(P - E)$, CPME).

	Onset		Retreat	
Simulation	CMFC	CPME	CMFC	CPME
0.2	1 May	1 May	16 Oct	16 Oct
0.3	6 May	6 May	21 Oct	21 Oct
0.4	6 May	6 May	26 Oct	26 Oct
0.5	16 May	11 May	26 Oct	26 Oct
1.0	26 May	26 May	6 Nov	1 Nov
2.0	1 Jun	1 Jun	16 Nov	16 Nov
4.0	1 Jun	1 Jun	21 Nov	16 Nov
6.0	1 Jun	1 Jun	16 Nov	16 Nov

does not feature any change. We will revisit this interesting feature of the warmest climates in our later analysis (Section 3.5).

It is interesting to note that with warming, the cross-equatorial transition of the poleward ITCZ branch (magenta; driven by large-scale MFC and often co-located with the absolute maximum in precipitation) delays, while the equatorward ITCZ branch (green; driven by BL dynamics) always lags the poleward branch and doesn't experience any delay (Fig. 3.4). The timing of the poleward ITCZ branch transition delays to the point that it eventually coincides with the migration into the summer hemisphere of the near-equatorial ITCZ in the warmer climates ($\alpha = 2.0, 4.0$, and 6.0), all of which have monsoon onset occurring around June 1 (Table 3.2). These results are consistent with the calculated WB16 monsoon onset and retreat indices, which are based on transitions in the MFC. What is interesting is that once the MFC-driven ITCZ branch transition timing delays to the point the branch coincides with the BL dynamics-driven ITCZ branch, whose timing remains consistent across all climates, it delays no further.

While this study focuses on the delay in the timing of the cross-equatorial transition of the poleward MFC-driven ITCZ branch with warming, it is also interesting to understand why the timing of the equatorward branch transitions remains so relatively consistent. As mentioned earlier, the equatorward branch matches well with the location of regions of low-level cross-equatorial meridional flow over regions where the surface temperature gradient reverses, resulting in weak temperature gradients in the deep tropics, and therefore regions of local ascent and precipitation (Pauluis,

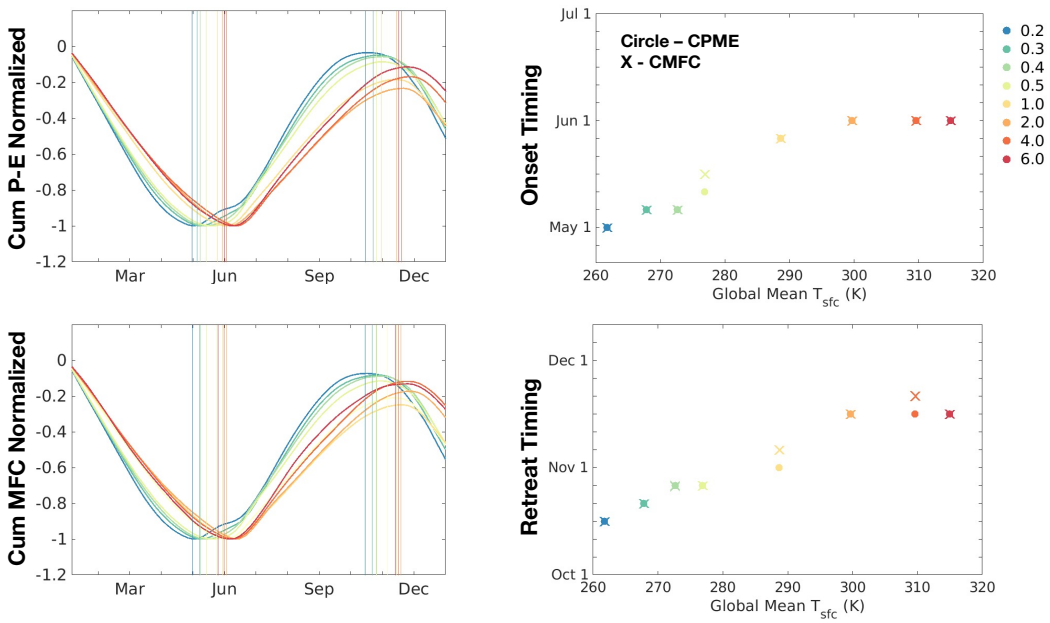

Figure 3.7: Cumulative moisture flux convergence (CMFC) mean and cumulative net precipitation ($P-E$) (CPME) mean (10°N–30°N), normalized by the minimum for each simulation, from which the monsoon onset and retreat indices are calculated as in Walker and Bordoni (2016). Resulting monsoon onset and retreat indices (vertical lines) are listed in Table 3.2.

2004) (Fig. 3.4). The reason why this transition timing remains constant across our different climates is likely due to the fact that the simulated climates are driven by changes in the atmospheric optical depth and not by orbital changes. Therefore, the insolation cycle remains unchanged. The timing of the equatorward precipitation local maximum seasonal transitions follows the timing of the seasonal transitions of the near-surface temperature, which can be related to the insolation cycle by a phase lag dependent on the slab-ocean MLD (Zhou & Xie, 2018). As both remain unchanged, the timing of the reversal in near-surface temperature gradient in the equatorial region also remains largely unchanged.

Altogether, a warming climate is observed to be accompanied with total increases in precipitation, further poleward excursions of the ITCZ during the solstitial seasons, and delayed monsoon onset. We next explore how these striking trends in precipitation spatial distribution and timing manifest themselves in changes in the circulation extent, strength, and leading-order AM budget.

Circulation Changes with Greenhouse Warming

Low-Level Horizontal Wind and Streamfunction

We begin by characterizing circulation changes in terms of changes in the low-level zonal wind u (Figure 3.8). As documented in previous work, in all simulations, the rapid migration of the ITCZ into the summer hemisphere subtropics is accompanied by a reversal in the zonal winds from easterlies to westerlies. Next, looking at the trends in the zonal winds with climate warming, the surface winds tend to increase in magnitude as the climate warms from the coldest climate to climates slightly colder than the current climate, with maximum zonal wind speeds of $u_{low} = 12$ m s^{-1} in the coldest climate with $\alpha = 0.2$, increasing to $u_{low} = 17$ m s^{-1} in the climate with $\alpha = 0.5$. For the climates with $\alpha > 0.5$, maximum zonal wind magnitudes remain similar in magnitude to that of the $\alpha = 0.5$ climate. A delay in the timing of reversal in surface zonal winds can be observed in Fig. 3.8 that matches well the delay in onset timing of monsoonal precipitation with warming observed in Fig. 3.2.

Figure 3.8 also displays the seasonal cycles of the low-level streamfunction Ψ_{low}. The bold zero contour of the streamfunction marks the circulation cell's boundary and throughout the entire seasonal cycle correlates well with the ITCZs marked in Figs. 3.2 and 3.4, particularly with the poleward ITCZ branch due to MFC driven by the Hadley cell (magenta in Fig. 3.4). The monsoon onset delay is also observed here since the cross-equatorial migration of the Hadley cell boundary during NH spring becomes increasingly delayed with warming, starting in the coldest climate in early May compared to early June in the climates warmer than the current climate. Altogether, the seasonal cycles of the precipitation, surface wind, and low-level circulation paint a consistent picture.

Angular Momentum Budget

Although we have seen a clear trend in monsoon onset delay with warming within the seasonal cycles of precipitation and low-level circulation, can evidence of the monsoon onset delay also be observed within changes in the balance of the meridional flow? Recalling the AM theory explained in Section 3.3, we consider the monsoon onset as a dynamical regime transition, where the two regimes differ in the amount of influence the EMFD has on the strength of the tropical overturning circulation. We investigate whether the monsoon onset delay is observable as a delay in the regime transition timing between a flow that is coupled to the EMFD to

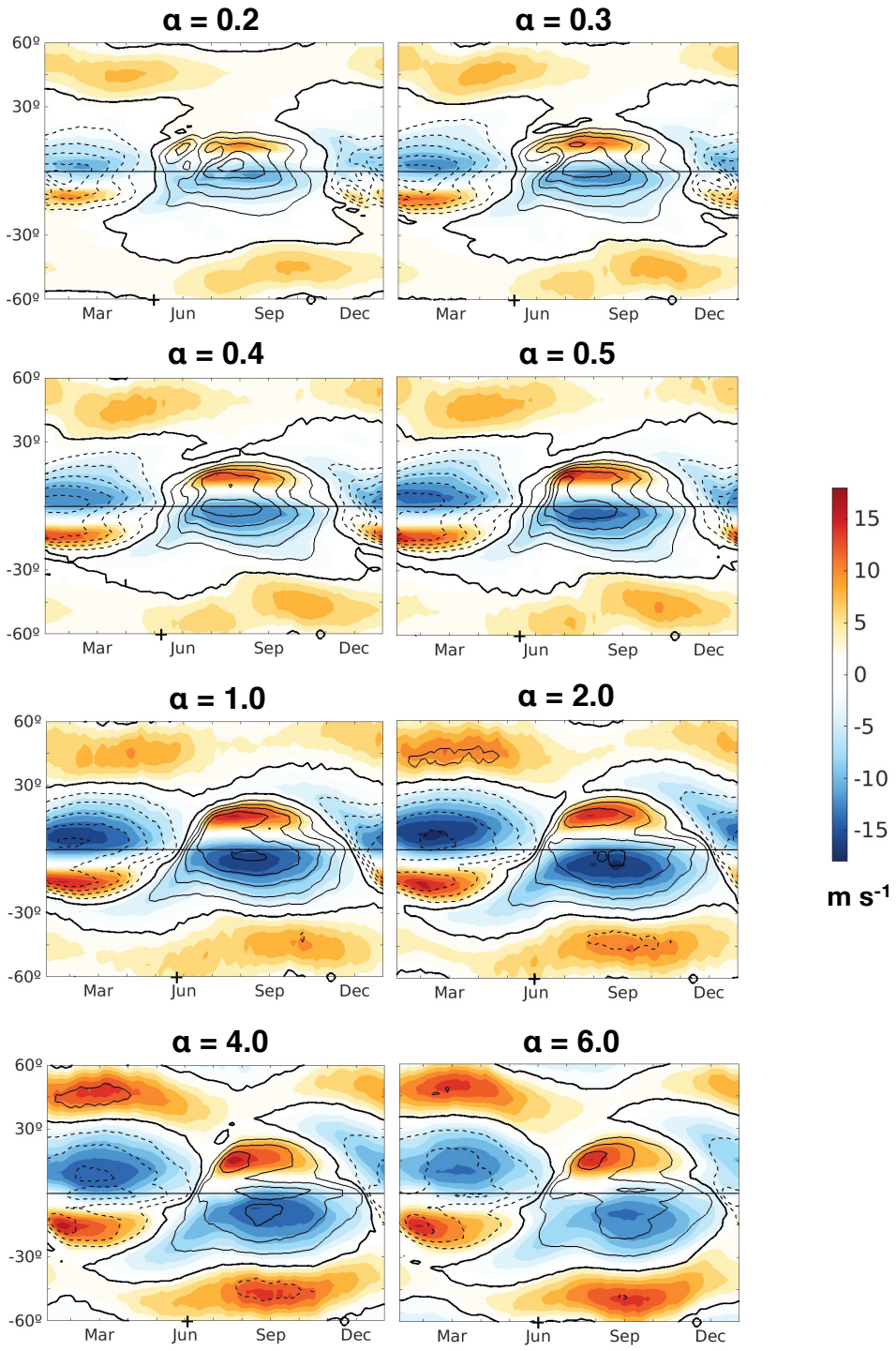

Figure 3.8: Seasonal cycle of the lower-level mass streamfunction and zonal wind from the coldest (top left) to warmest (bottom right) simulated climates. Color contours indicate lower-level (σ = 0.887) zonal wind (contour interval: 2 m s^{-1}). Black contours mark the lower-level mass streamfunction Ψ_{low} (counterclockwise in solid, clockwise in dashed with contour interval 40×10^9 kg s^{-1}, zero contour in bold). Onset and retreat are marked, as in Fig. 3.2.

a flow that is more AMC and responds more directly to thermal constraints and what are the trends in absolute and relative strength of the eddy versus mean circulations.

Figure 3.6 contains the streamfunction contours for the climates with $\alpha = 0.2$, 1.0, and 4.0 during the first pentad of each month from May to September. There are striking differences in the circulation structure, strength, and transition timing across the climates. As the climate warms, the circulation grows deeper, with Hadley cell upper branch heights increasing from $\sigma \sim 0.60$ to 0.23 to 0.12 between the simulations with $\alpha = 0.2$, 1.0, and 4.0, respectively. As discussed in the previous subsection, we also observe differences in the seasonal evolution of the two-cell structures for each climate. In all the $\alpha = 0.2, 1, 0$, and 4.0 climates shown, the near-equatorial region of ascent associated with BL dynamics becomes more pronounced in the summer by July 1, once a stronger meridional cross-equatorial flow has been established. However, how this region of ascent persists throughout the remaining summer season varies between the climates. Within the cooler $\alpha = 0.2$ climate, this region of ascent persists throughout the summer through September 1, but appears to weaken. In the $\alpha = 1.0$ climate, the near-equatorial ascent region also continues to persist through September 1, but in contrast to that within the $\alpha = 0.2$ climate, strengthens. Finally, within the $\alpha = 4.0$ climate, the near-equatorial ascent region also continues to persist through September, but appears to strengthen and deepen even further than within the $\alpha = 1.0$ climate. These observations are consistent with the doubly peaked precipitation distributions observed in Figs. 3.4 and 3.5. The circulation strength also changes across the climates. The streamfunction contours grow more tightly packed together within the climate with $\alpha = 1.0$ in comparison to both the $\alpha = 0.2$ and 4.0 climates, further demonstrating that circulation strengths tend to peak at climates similar to the current climate (Fig. 3.1c). Additionally, the delay in transition timing of the circulation is clearly depicted. In the coldest climate with $\alpha = 0.2$, although May 1 has a complex two cell structure, by June 1 a broad cross-equatorial circulation has already been established that continues to remain strong through September 1. As the climate warms to the current climate with $\alpha = 1.0$, during May 1 the Hadley cell ascending branch is still held back well within the SH. At June 1, the ascending branch has just barely crossed the equator, and eventually by July 1, a strong broad circulation is well established. Further warming the climate with $\alpha = 4.0$, the transitions become even further delayed. During both May 1 and June 1, the Hadley cell ascending branch is still held back within the SH. Only by July 1 is a strong cross-equatorial circulation observed, which only reaches its furthest poleward extent by August 1.

The delay of monsoon onset with warming is also observed within changes in the timing of the dynamical regime switch. As the climate warms, the circulation tends to take longer to switch from a flow tied to the EMFD to a more AMC flow. The AM contours are superimposed over the streamfunction contours within Fig. 3.6. A similar delay is observed in the transition timing of when the circulation becomes broad and cross-equatorial and when the circulation becomes more AMC, which is identified as when the AM and streamfunction contours run parallel in the circulation upper branch. Within the $\alpha = 0.2$ climate, by June 1, as the circulation already grows broader, the AM contours also begin to run more parallel to the flow in the upper branch of the Hadley cell and the flow begins to switch to the AMC monsoon dynamical regime. In contrast, as the climate warms, the $\alpha = 1.0$ and $\alpha = 4.0$ climates only begin having well-established broad cross-equatorial circulations with AM contours running parallel to the upper-level flow starting July 1 and August 1, respectively.

The delay associated with a warming climate in the transition timing of the dynamical regime from a flow tied to the EMFD to the more AMC flow of the monsoon regime is more clearly observed when we look at the seasonal cycles of the terms in the upper-level zonal momentum budget in Eq. (3.3) (Fig. 3.9). The zonal mean Coriolis term $f\overline{v}$ is approximately balanced by the sum of the mean flow advection $-(\overline{v}\partial\overline{u}/\partial y+\overline{\omega}\partial\overline{u}/\partial p)$ (note that in Eq. (3.3) the vertical advection term is neglected) and the eddy momentum flux convergence (EMFC) $-(\partial\overline{u'v'}/\partial y+\partial\overline{u'\omega'}/\partial p)$. In the $\alpha = 0.2$ climate, at the end of May the zonal mean Coriolis term $f\overline{v}$ rapidly increases in magnitude in both the NH and SH as the meridional winds increase across the entire winter Hadley cell and the circulation becomes broad and cross-equatorial. At the same time, the mean flow advection term, $-(\overline{v}\partial\overline{u}/\partial y+\overline{\omega}\partial\overline{u}/\partial p)$, also increases in magnitude across the winter Hadley cell and begins to dominate the balance with the mean Coriolis term, signaling the regime transition of the circulation into a more AMC flow at monsoon onset. Meanwhile, the EMFC remains relatively small in magnitude compared to the other two terms across the winter Hadley cell. This is due to the rapid intensification of the upper-level easterlies within the winter cell (Fig. 3.10), which are not conducive to westward-propagating extratropical eddies (Charney, 1969; Webster & Holton, 1982), and as a result shield the cell from the influence of the EMFD. Although plotted at different vertical levels and with different color ranges to accommodate changes in the circulation height and strength, the $\alpha = 1.0$ and 4.0 climates show similar circulation regime transitions into monsoon-like regimes with flow dominated by the mean circulation. However,

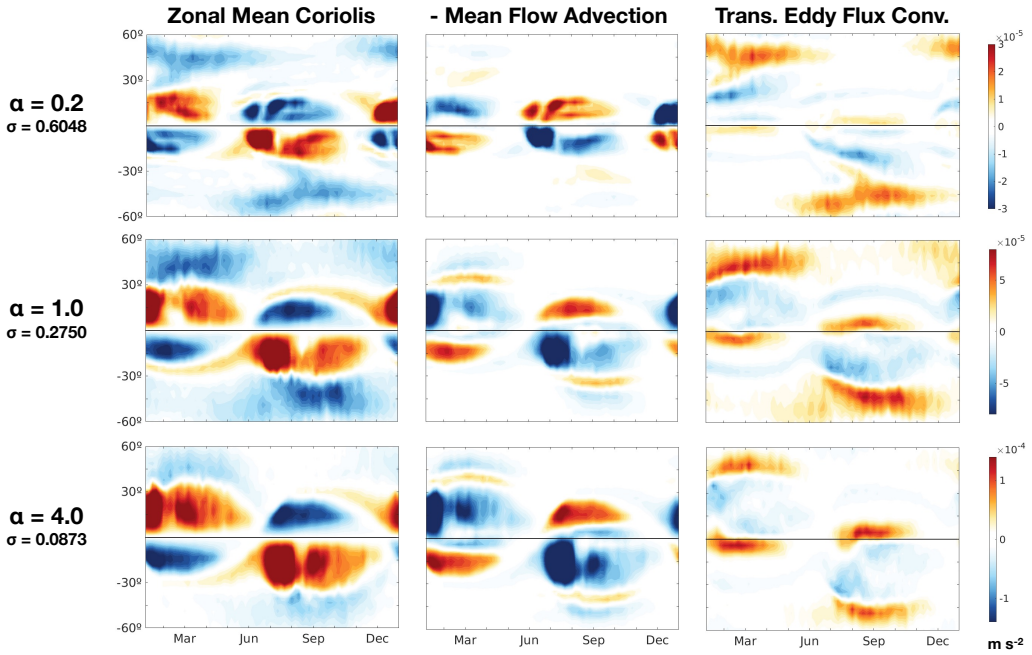

Figure 3.9: Seasonal cycle of the terms in the upper-level (height chosen at vertical level with maximum southward meridional wind) zonal momentum budget in Eq. (3.3): zonal mean Coriolis term $f\overline{v}$ (left column), mean flow advection $-(\overline{v}\partial\overline{u}/\partial y + \overline{\omega}\partial\overline{u}/\partial p)$ (middle column), and transient eddy momentum flux convergence $-(\partial\overline{u'v'}/\partial y + \partial\overline{u'\omega'}/\partial p)$ (right column) from the $\alpha = 0.2$, 1.0, and 4.0 simulations (top to bottom rows, respectively) with contour interval 0.2×10^{-5} m s^{-2} ($\alpha = 0.2$), 0.5×10^{-5} m s^{-2} ($\alpha = 1.0$), and 0.8×10^{-5} m s^{-2} ($\alpha = 4.0$). Note that values from each climate are plotted on different color ranges due to the large differences in magnitudes between the simulations.

the transition timing delays as the climate warms, with the mean flow advection dominating the balance with the mean Coriolis term starting around end of June within the $\alpha = 1.0$ climate and the beginning of July within the $\alpha = 4.0$ climate.

The changes that we observe in the precipitation and circulation seasonal cycles with a warming climate, including increases in the precipitation amount and circulation strength and changes in their spatial structure and poleward extents, most strikingly show a clear delay in monsoon onset timing. While the onset delay is unmistakable within this seasonal cycle analysis, it is still unclear what causes the onset timing delay with warming. In the following section, we use the energetic framework to further investigate the relationship between the warming climate and the monsoon onset delay.

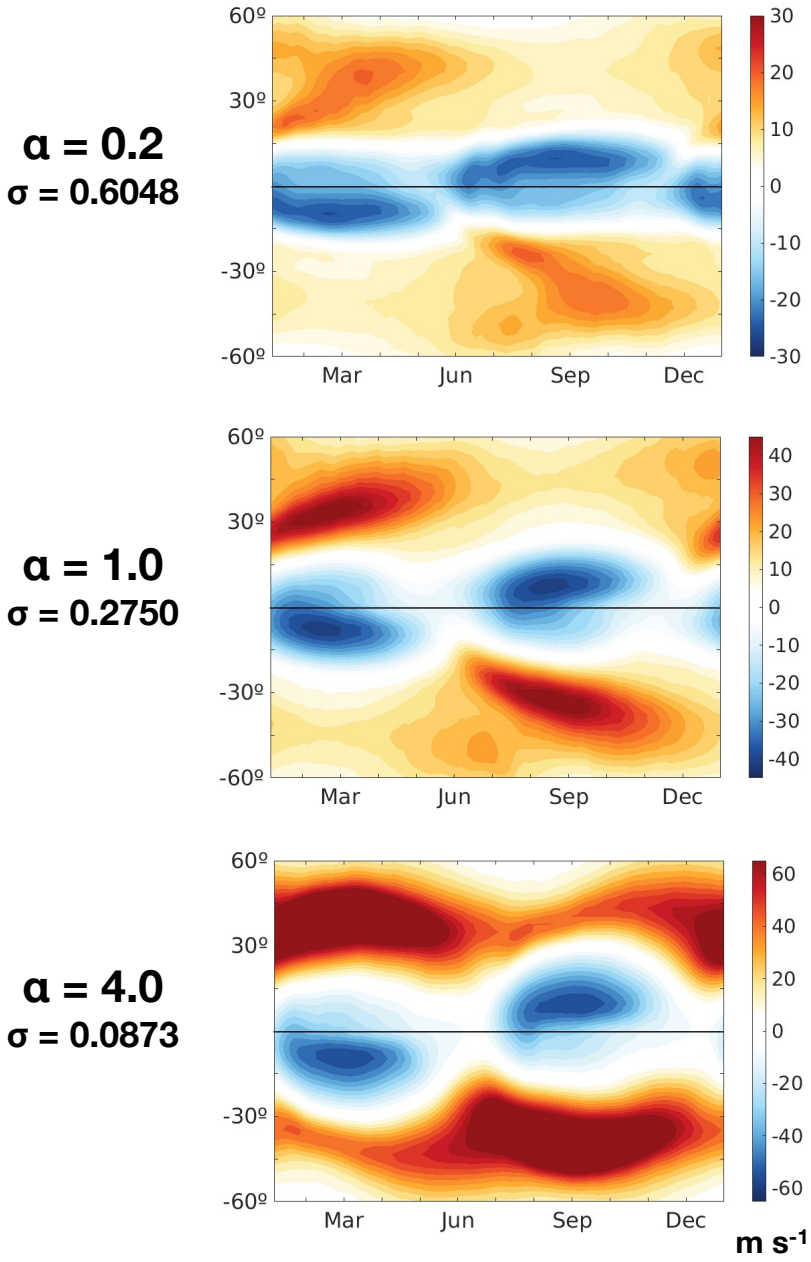

Figure 3.10: Seasonal cycle of the upper-level (same as in Fig. 3.9) zonal wind u from the $\alpha = 0.2$, 1.0, and 4.0 simulations (top to bottom) with contour interval 2 m s^{-1} ($\alpha = 0.2$), 3 m s^{-1} ($\alpha = 1.0$), and 5 m s^{-1} ($\alpha = 4.0$). Note each plot shows a different color range due to the large differences in magnitudes between the simulations. The positive values from the $\alpha = 4.0$ climate are saturated to show more detail.

3.5 Energetic Framework Perspective

There is a rich literature exploiting the energy budget to study different aspects of tropical circulations and their response to climate change (Chou & Neelin, 2004; Kang et al., 2008; Neelin & Zeng, 2000; Seth et al., 2013; Song et al., 2018). In this section, we take advantage of this powerful theoretical framework to study how a warming climate can cause the monsoon onset timing delay observed within our idealized aquaplanet simulations.

Song et al. (2018) were able to show that within CMIP5, with $4\times CO_2$ warming in the zonal mean there was a clear delay in monsoon onset timing. By analyzing the changes in the terms of the MSE budget equation (Eq. (3.4)) with warming and comparing these changes in NH spring versus NH summer, they found that with warming, the surface temperatures increase more in NH spring than NH summer in the NH, and therefore increase the latent heat (LH) demand in the NH. This increased LH demand in the NH during spring results in a southward shift of the ascending branch of the tropical circulation, and with it the ITCZ, in order to transport more energy from the SH to the NH to keep up with the LH demand. As a result, with warming the ITCZ remains in the SH for longer and delays the monsoon onset. The key argument is that in warmer climates, it is the increased energy storage within the NH subtropics, driven by the increased latent energy tendency during NH spring, that drives that monsoon onset delay. Here, following the analysis applied by Song et al. (2018) to the CMIP5 $4\times CO_2$ output, we perform a similar analysis of the interseasonal changes in the atmospheric energy budget in order to investigate whether similar mechanisms are observed within our simulations and whether the energetic framework argument can also explain well the monsoon onset timing changes we observe over the extreme range of climates covered by our simulations.

To start, we first analyze the seasonal evolution of all the terms in the MSE budget to look for evidence of an increasing role for storage as an important term for the atmospheric energy budget with warming. Recalling and rearranging Eq. (3.4), the net energy input into the atmospheric column F_{net} should be balanced by the sum of the divergence of AHT, calculated as the horizontal divergence of the vertically-integrated MSE flux $\partial\langle vh\rangle/\partial y$, and the energy storage, calculated as the time tendency of the vertically-integrated energy $\partial\langle\mathscr{E}\rangle/\partial t$. Fig. 3.11 shows the NH tropical mean (10°N - 30°N) F_{net}, along with the mean component of the energy flux divergence and the energy storage. Note that in Eq. (3.4) the F_{net} is balanced by the sum of the total energy flux divergence and the energy storage. Here, we show the

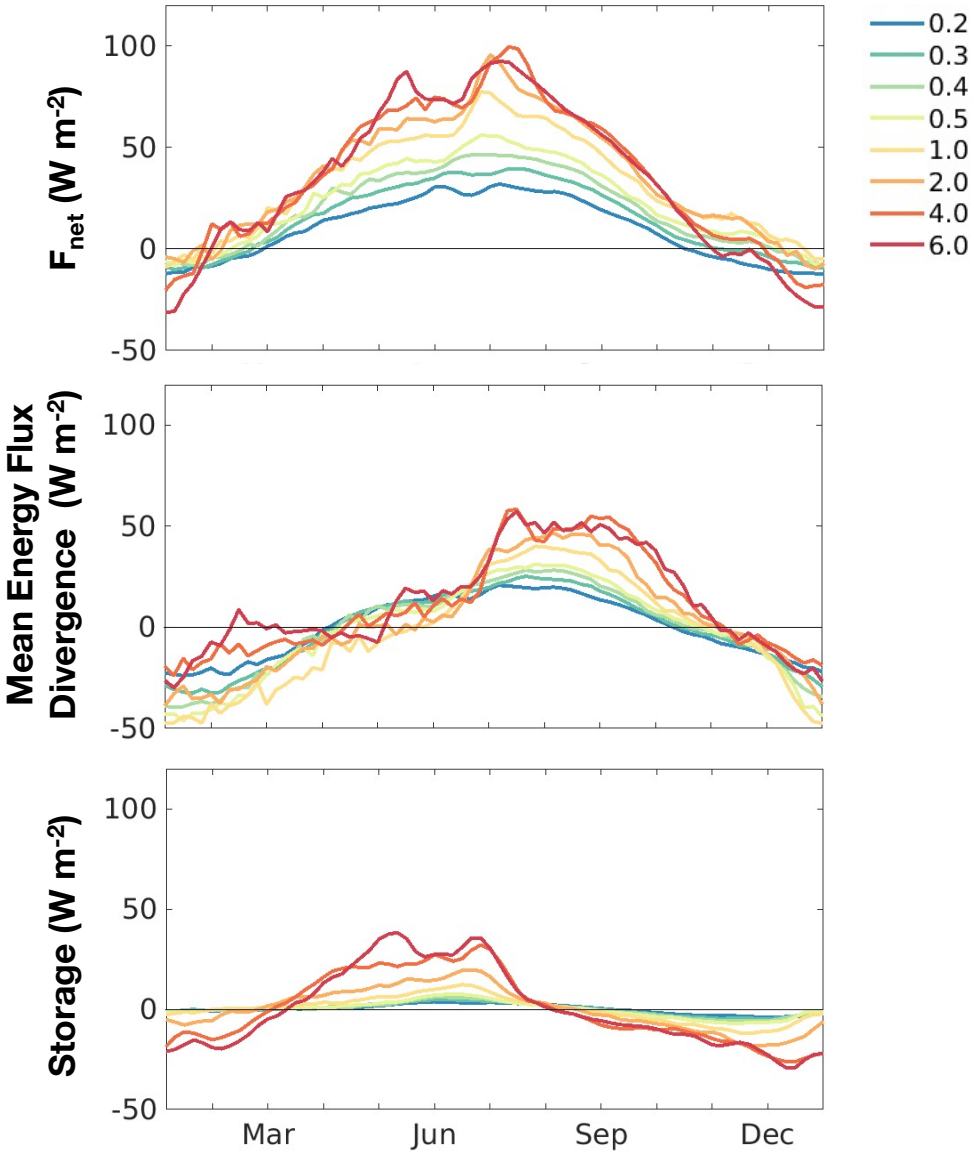

Figure 3.11: Seasonal cycle of the NH tropical mean (10°N - 30°N) of the terms in the MSE budget: F_{net} (top), the mean component of the energy flux divergence $\partial\langle\overline{vh}\rangle/\partial y$ (middle), and the energy storage $\partial\langle\mathscr{E}\rangle/\partial t$ (bottom) from all the simulated climates.

mean component because this represents the divergence of energy flux performed by the mean tropical circulation, our focus here. Starting from the the coldest climates ($\alpha = 0.2, 0.3, 0.4$, and 0.5), we observe that the F_{net} has a sinusoidal shape roughly following the insolation cycle, with minimum values during NH winter and maximizing in the NH summer around July. For these climates, F_{net} is almost entirely balanced by the mean energy transport term, with energy storage playing a negligible role. This is due to the colder temperatures of these climates, which through the Clausius-Clapeyron relation, limits the amount of atmospheric moisture and, with it, latent energy storage. As the climate warms, we observe the overall NH summer F_{net} increase in magnitude, with maximum summertime values increasing from 32 Wm^{-2} to 92 Wm^{-2} between the coldest ($\alpha = 0.2$) and warmest ($\alpha = 6.0$) climates, and F_{net} maximizing during July in all the climates. As the climate warms, the relative role of the energy flux divergence and storage terms in balancing the F_{net} throughout the seasonal cycle becomes more complex. Within the warmer climates, the mean energy flux divergence increases in magnitude with warming, and has a rapid intensification in July, matching well the timing of largest peak in F_{net} and dominating the balance with F_{net} over the storage. The large values of mean energy flux divergence continue to dominate the balance with F_{net} from July to October. This part of the season is at the height of the monsoon, where the circulation is more AMC and the mean circulation driven by the Hadley cell is broad and cross-equatorial, driving strong large-scale MFC and precipitation. As expected by the Clausius-Clapeyron relationship, as the climate warms we observe a striking increase in the energy storage. In contrast to the coldest climates where storage was negligible, in the warmest climates ($\alpha = 2.0, 4.0$, and 6.0), as the climate warms the storage plays an increasingly significant role in the MSE budget, particularly during NH spring from April to June.

Fig. 3.12 takes a closer look at the MSE budget decomposition from the climates with $\alpha = 0.2, 1.0$, and 4.0. The tropical mean precipitation is also plotted to highlight the relative timing to the changes in the atmospheric energy balance. In all three climates, we see a couple common trends. First, in all three climates, in NH summer when the mean energy flux divergence increases, the eddy energy flux divergence decreases and the energy transport is dominated by the mean. This balance occurs during the monsoon season from around June to October, when the circulation is shielded from the influence of extratropical eddies, and as a result becomes more AMC and driven by thermal forcing. The timing of the mean dominating over the eddy flux divergence, occurring in early May, early June, and late June

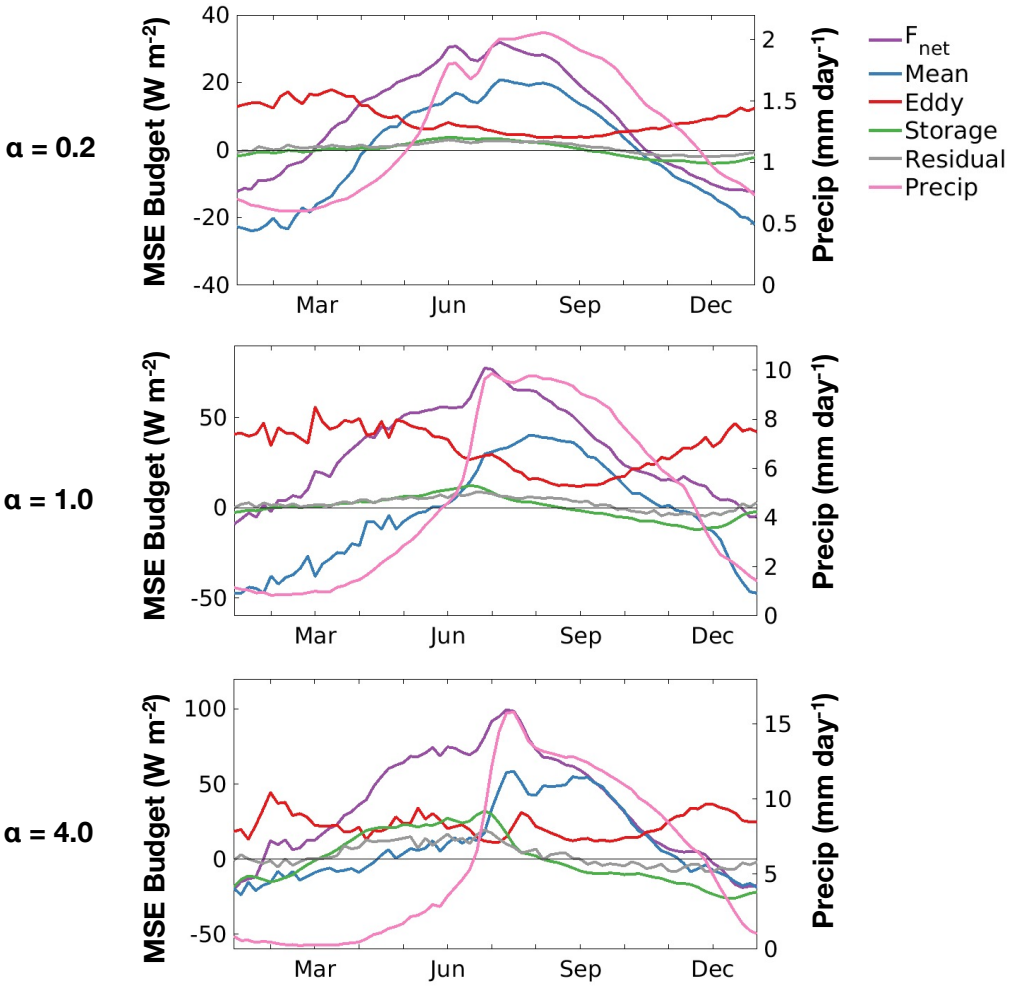

Figure 3.12: Seasonal cycles of the tropical mean terms in the MSE budget from the $\alpha = 0.2$ (top), $\alpha = 1.0$ (middle), and $\alpha = 4.0$ (bottom) climates. F_{net} (purple) is balanced by the sum of the mean energy flux divergence (blue), the eddy energy flux divergence (red), the energy storage (green), and the remaining residual term (gray). On the right y-axis, precipitation (pink) is plotted to highlight the relative timing of all the seasonal changes. Note different y-axis ranges are used to show more detail within each climate.

in the $\alpha = 0.2, 1.0$ and 4.0 climates, respectively, is consistent with the observed dynamical flow regime transitions observed in Fig. 3.9. During the monsoon season when the mean dominates over the eddy energy transport, the main energy balance is between F_{net} and the mean energy flux divergence. Second, from all the terms in the MSE budget, the precipitation seasonality best tracks the seasonal cycle of the mean energy flux divergence, as expected. The peak in precipitation matches well the timing of the peak in mean energy flux divergence. This is consistent with the monsoon onset and the increased monsoonal precipitation due to the MFC driven by the Hadley cell performing the mean energy transport. Third, we observe that the F_{net} tends to lead the mean energy transport and precipitation. A closer look at each climate is needed to observe trends in the MSE budget with warming.

In the coldest climate ($\alpha = 0.2$), the thermal forcing (F_{net}) peaks earlier in the beginning of June. With the reduced magnitude of the eddy energy transport, the F_{net} is mostly balanced by the mean energy transport, especially since the storage and residual terms are so small. In the current climate ($\alpha = 1.0$), F_{net} peaks at the end of June. Interestingly, during NH winter through spring, the eddy term remains relatively large, even being the dominant term in April. We also do notice that the storage term has started to increase in NH spring, however it is still dominated by the eddy term. In the warmer climate ($\alpha = 4.0$), F_{net} peaks also in late June. However, in this hotter climate during NH spring the F_{net} is instead mainly balanced by the eddy term and the storage term. With warming, the storage term has increased to play a more important role in the atmospheric energy budget, particularly during NH spring.

Although we have found clear evidence that within our climate change simulations we observe an increasing role of the energy storage on the atmospheric energy budget with warming, how does this increase in storage affect the circulation transitions? What controls the change in the storage, especially its seasonal evolution? To understand the role of the changes in energy storage on the monsoon, we look at the interseasonal differences in changes in the terms of the MSE budget in Eq. (3.4) with warming between NH spring verus NH summer, as in Song et al. (2018). Figure 3.13 shows these interseasonal differences (April mean minus July mean) in the changes in the three terms of the atmospheric energy balance written in Eq. (3.4) relative to the current climate, calculated as $\Delta(.) = [(.)_{\mathrm{APR}} - (.)_{\mathrm{JUL}}]_{\alpha} - [(.)_{\mathrm{APR}} - (.)_{\mathrm{JUL}}]_{\alpha=1.0}$. First, we observe that as the climate warms, the divergence of AHT increases more in NH spring than in NH summer in SH around -30° to -40°, resulting in hemispherically

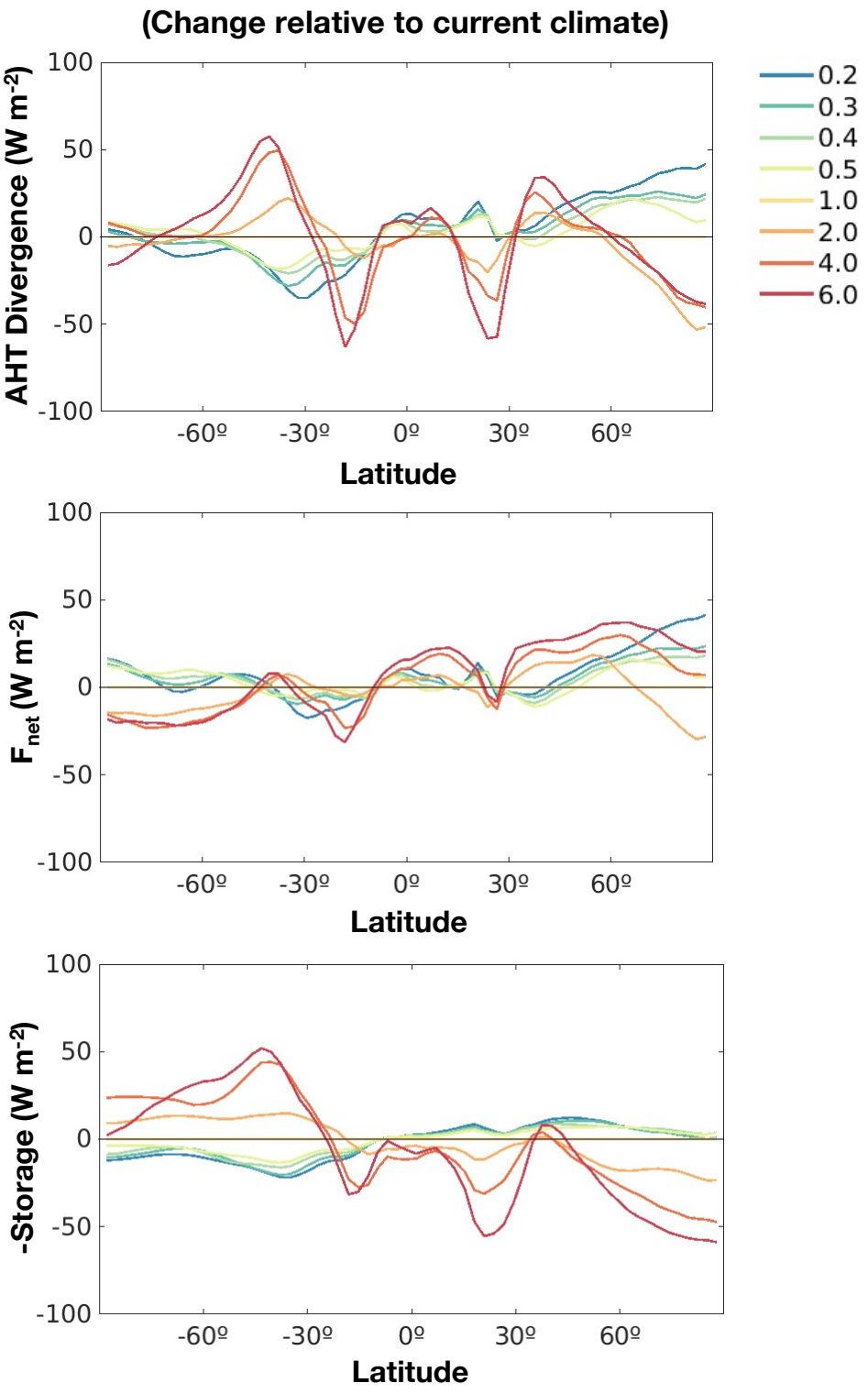

Figure 3.13: The changes relative to the current climate in the interseasonal differences (April minus July) of the terms of the atmospheric energy budget equation (Eq. (3.4)).

asymmetric distributions of changes with warming. As the ascending branch of the tropical circulation, and with it the ITCZ, is collocated with the region of maximum divergence of AHT, this result shows that as the climate warms, the divergence of AHT is greater in NH spring in the SH for longer, resulting in the ascending branch of the circulation and the ITCZ remaining in the SH for longer, and causing a delay in monsoon onset. What drives these changes in the AHT divergence in NH spring versus summer? Fig. 3.13 also shows the interseasonal changes in the F_{net} and the storage, which is plotted as $-\partial\langle\mathscr{E}\rangle/\partial t$ to match Eq. (3.4), so positive (negative) values signal a decrease (increase) in energy storage. The interseasonal changes in F_{net} relative to the current climate are relatively more neutral, but a more pronounced hemispheric asymmetry is seen in the warmer climates relative to the colder climates. In contrast, the interseasonal changes in the MSE tendency relative to the current climate dominate the balance in Eq. (3.4) and balance the changes in the energy flux divergence. As the climate warms, the energy storage into the column decreases more in NH spring than summer in the SH, also around -30° to -40°, corresponding well to the region of increased AHT divergence. We also note that at the same time, in the NH, between 20° to 30°, the MSE storage increases more in NH spring than summer. These two effects give rise to the hemispherically asymmetric changes observed in the AHT divergence that are related to the monsoon onset delay with warming.

We take a closer look at what causes the energy storage to decrease more in the SH and to increase more in the NH in the NH spring than summer by decomposing $-\partial\langle\mathscr{E}\rangle/\partial t$ into the internal energy and latent energy components. The interseasonal differences in changes in the latent energy tendency component of the MSE tendency, $-\partial\langle L_v q\rangle/\partial t$, relative to the current climate are plotted in Fig. 3.14. Comparing the energy storage in Fig. 3.13 and the latent energy tendency in Fig. 3.14 shows that the changes in latent energy tendency dominate the changes in the MSE tendency, which drive the hemispherically asymmetric changes observed in the AHT divergence. Under global warming during NH spring, the increased LH storage in the NH shifts the ascending branch of the Hadley cell to the SH, and with it the ITCZ, to transport more energy towards the NH to keep up with the increased LH demand, and therefore delays the monsoon onset.

To further investigate the interseasonal changes in the energy storage with warming, we need to determine what controls the seasonal evolution of the latent energy storage, $\partial\langle L_v q\rangle/\partial t$. Song et al. (2018) linearized the Clausius-Clapeyron relationship

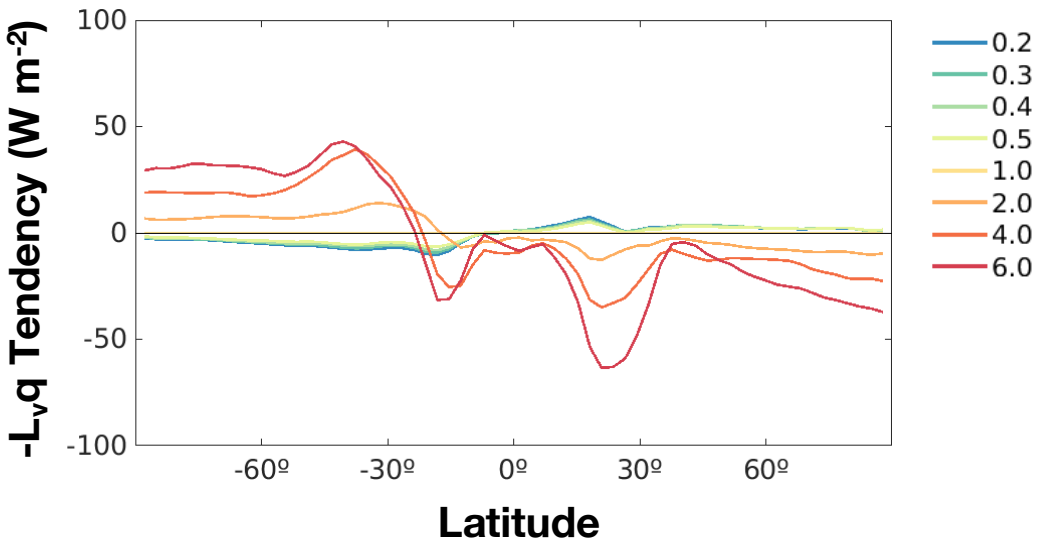

Figure 3.14: The changes relative to the current climate in the interseasonal differences (as in Fig. 3.13) of the latent energy tendency component of the MSE tendency plotted in Fig. 3.13.

to show that the change in latent energy tendency, $\Delta\frac{\partial\langle L_v q\rangle}{\partial t}$, under global warming is linearly proportional to the climatological surface temperature tendency of the current climate, $\frac{\partial T_s}{\partial t}$:

$$\Delta\frac{\partial\langle L_v q\rangle}{\partial t} \approx a\Delta T_s\frac{\partial T_s}{\partial t}, \tag{3.5}$$

where a is a coefficient determined by the present climate state (as in Song et al., 2018), T_s is the surface temperature, and $\Delta(.) = (.)_\alpha - (.)_{\alpha=1.0}$ represents the change relative to the current climate. Because our simulations cover such an extreme range of colder and warmer climates than our current climate, we modify Eq. (3.5). We continue to calculate both $\Delta\partial\langle L_v q\rangle/\partial t$ and ΔT_s relative to the control climate ($\alpha = 1.0$). However, in the calculation of a and $\partial T_s/\partial t$, we use temperature values from the climate we are comparing to the current climate as the climatological values, instead of values from the current climate. We calculate the LHS of Eq. (3.5) directly and compare with the RHS linearized approximation at each latitude for April and July for each of our simulations. The results, shown in Fig. 3.15, remain quite consistent with the results presented in Song et al. (2018) and the linear approximation of the latent energy tendency (middle row) captures the changes in the directly calculated latent energy tendency (top row) quite well, despite we are studying idealized aquaplanet simulations that cover a much larger range of climates than covered in CMIP5. Consistent with the results from Song

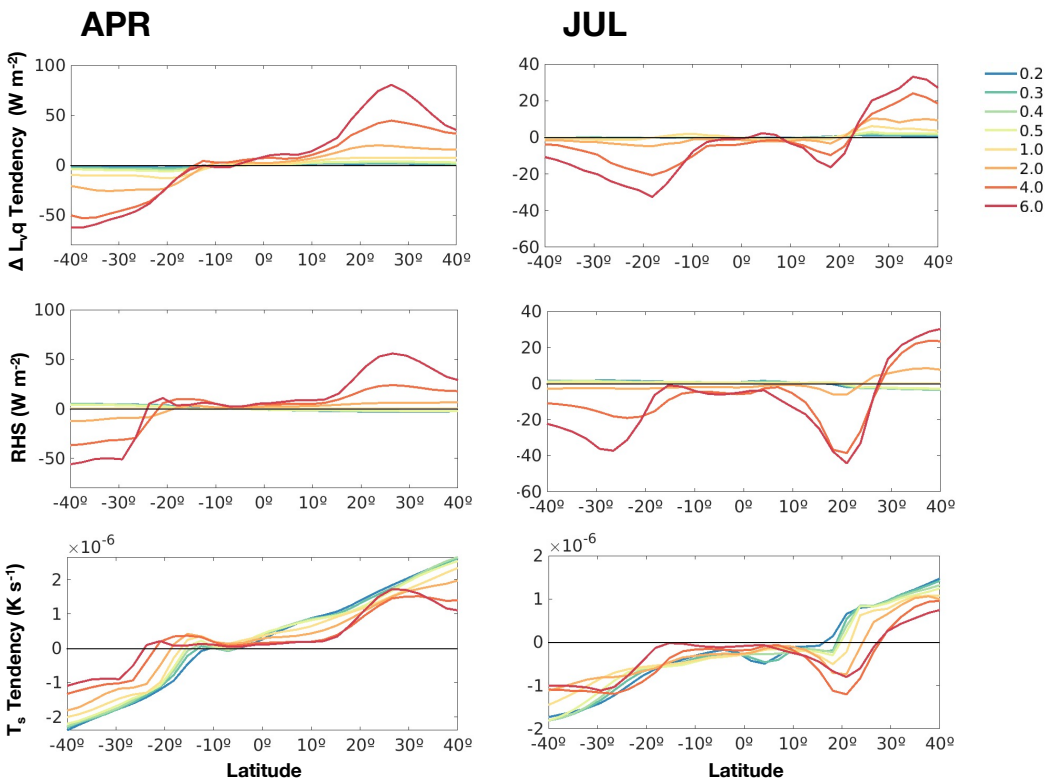

Figure 3.15: The April (left column) and July (right column) monthly mean changes relative to the current climate in latent energy storage. The change in latent energy tendency $\Delta\frac{\partial\langle L_v q\rangle}{\partial t}$ calculated directly from the model output (top row) and calculated as the RHS of the linear approximation in Eq. (3.5) (middle row). The surface temperature tendency $\frac{\partial T_s}{\partial t}$ from each climate used to calculate the linear approximation (bottom row).

et al. (2018), within our idealized simulations, the seasonal variations of a and ΔT_s are relatively weak, whereas the seasonal cycle of the latent energy tendency strongly follows that of the surface temperature tendency of each climate $\partial T_s/\partial t$ (compare top and middle rows to the bottom row in Fig. 3.15). The changes in April versus July are quite different. With warming, in April, the latent energy tendency has a more hemispherically asymmetric shape, with latent energy storage increasing more in the NH and latent energy storage decreasing more in the SH. This is driven by the strongly hemispherically asymmetric shape of the April mean T_s tendency (bottom left panel in Fig. 3.15), where larger positive magnitudes of T_s tendency are observed in the NH and larger negative values are observed in the SH because during NH spring, the NH heats up more as it is entering summer while the SH cools down and begins to enter winter. In contrast, in July, within the tropics the latent

energy tendency remains relatively small and symmetric about the equator. This is due to the smaller values of surface temperature tendency during July because under the current climate, T_s maximizes in the summer around July. As a result, in July the T_s tendency, and with it the $\Delta L_v q$ tendency, is generally smaller than in April. It is interesting to note that in the warmest climates ($\alpha = 2.0, 4.0$, and 6.0), at high temperatures the connection between the seasonality of the surface temperature and latent energy storage has an even more exaggerated effect. During NH spring in April, a peak in T_s tendency is observed in the subtropical latitudes between 20° to 30°, which gives rise to a significant peak in latent energy storage in the same latitudes and highlights the impact of the nonlinear relationship between temperature and moisture. On the other hand, during NH summer in July, in the warmest climates, we unexpectedly observe negative T_s tendency values, meaning that within the NH tropics the surface actually starts to cool in July. The negative T_s tendency during July has an interesting effect on the changes in latent energy storage. Following the seasonality of the surface temperature, the NH tropics actually experience a decrease in latent energy storage with warming during July.

Altogether, the energetic framework paints a convincing picture to explain the monsoon onset delay with warming. With warming, surface temperatures increase more in the NH during NH spring than summer. This in turn, increases the LH demand in the NH during spring. The increased LH demand in the NH during spring forces the circulation ascending branch, and with it the ITCZ, to be held back within the SH for longer in order to transport more energy towards the NH to supply the increased LH demand. This in turn delays the cross-equatorial jump of the ITCZ, and with it the monsoon onset.

Revisiting the Monsoon Onset Delay Saturation with Extreme Warming

It is interesting that as the climate warms, the monsoon onset delay eventually saturates (Table 3.2 and Figs. 3.2 and 3.4). Indeed, by the mechanism explored above, one might expect that as the climate continues to gets warmer, the atmosphere will have an always increasing capacity to hold more moisture following the Clausius-Clapeyron relation. By this reasoning, the energy storage and effective heat capacity of the atmosphere would continue to increase and with more climate warming we would expect a greater monsoon onset delay. In the same way, one could guess that in a warmer climate, with a higher effective heat capacity due to increased atmospheric moisture, the warmer climate would create a more "ocean-like" circulation, similar to increasing the MLD of an aquaplanet, giving the system more memory and allowing

for the seasonal transitions in the circulation and precipitation to be delayed.

In fact, what we find is different. If hotter climates were to result in more"ocean-like" lower boundaries, we would not only find delayed monsoon onset, but also smaller poleward excursions of the ITCZ and smoother seasonal transitions, and altogether circulations that would not resemble monsoons (Hui & Bordoni, 2021). Instead, from our idealized simulations, in our extremely hot climates ($\alpha = 2.0, 4.0$, and 6.0), although the onset timing is delayed, we continue to observe very monsoon-like circulations with rapid onset and dynamical regime transitions and even further poleward extents. So why doesn't a hotter climate with larger energy storage continue to increase the monsoon onset delay?

Especially within the extremely warm simulated climates where energy storage plays a larger role, the monsoon onset is determined by when the energetic balance with the thermal forcing, F_{net}, switches from being balanced by the energy storage to being balanced by the mean energy transport by the circulation. Recalling that the total energy storage is dominated by the latent energy storage (compare bottom panel of Fig. 3.11 with Fig. 3.16a), what determines the timing of that switch is the seasonality of the latent energy storage, which we showed is driven by the seasonality of the surface temperature tendency, as shown in Fig. 3.15 and approximated by Eq. (3.5). Particularly, the mean energy flux divergence starts to dominate the balance when the storage term rapidly decreases. Fig. 3.16 compares the seasonal cycles of the tropical mean latent energy storage (also shown normalized to show more detail) and the surface temperature tendency. The curves are comparable (as they are approximately linearly proportional to each other by a and ΔT_s as in Eq. (3.5)), particularly when the terms change sign. As expected, Fig. 3.16a shows that the latent energy storage increases significantly with warmer climates. More importantly, however, we observe that in the warmest climates ($\alpha = 4.0$, and 6.0), the latent energy storage actually decreases and changes sign to negative earlier in the season than in the colder simulations (Fig. 3.16b). This results in an earlier decrease in total energy storage and no relative delay in the timing of the switch from the F_{net} being compensated by the storage to being balanced by the mean energy transport (note the timing of the peak increase in mean energy flux divergence in Fig. 3.12 between the hottest climates is hard to distinguish). This explains why we do not observe increasing onset delay within our hottest simulated climates.

What might cause the latent energy storage in the warmest climates to decrease earlier in the season? Within the warmest climates, the earlier change of sign in the

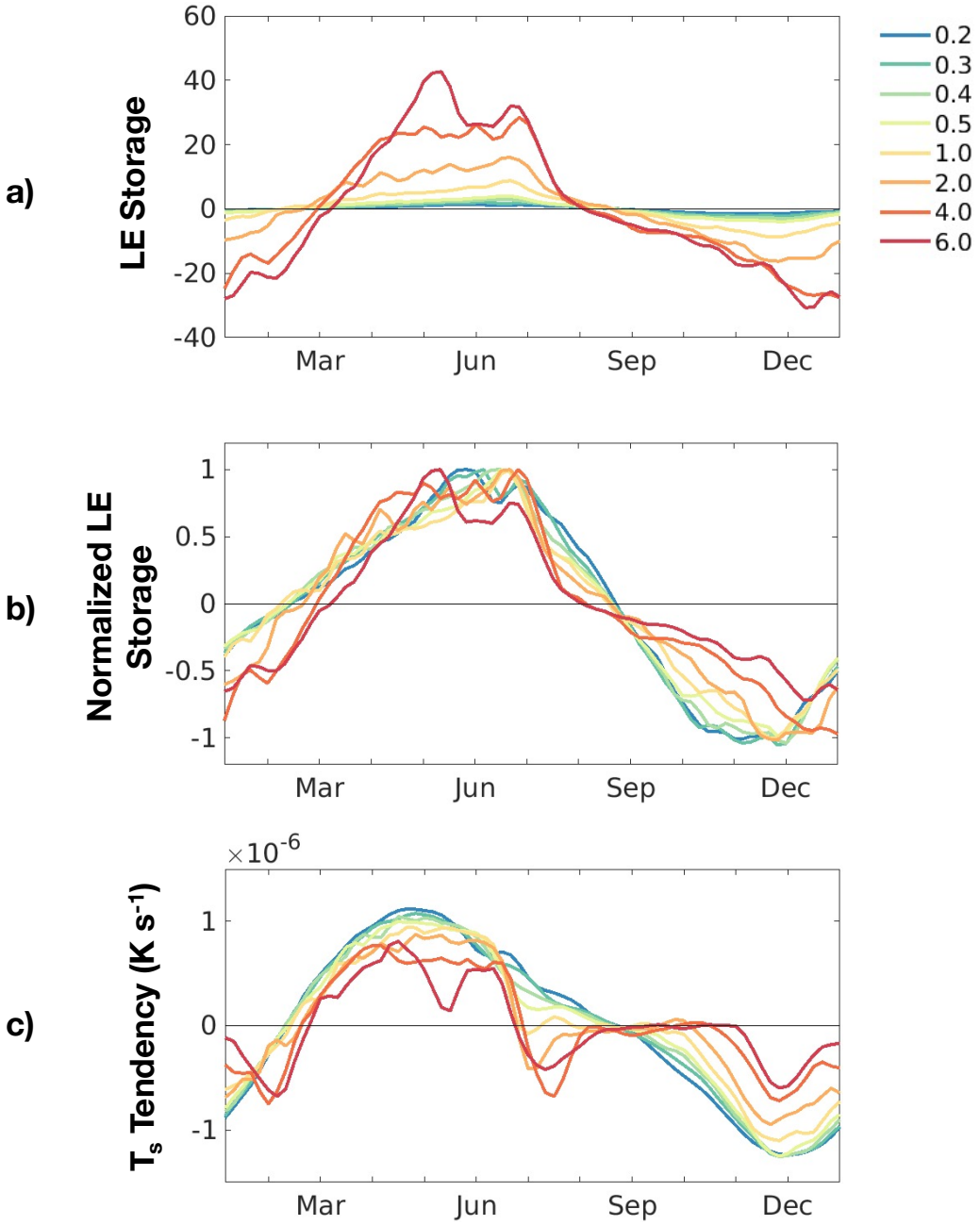

Figure 3.16: The seasonal cycles of the tropical mean a) latent energy storage $\partial\langle L_v q\rangle/\partial t$, b) latent energy storage normalized by the maximum of each curve to show more detail, and c) surface temperature tendency $\partial T_s/\partial t$.

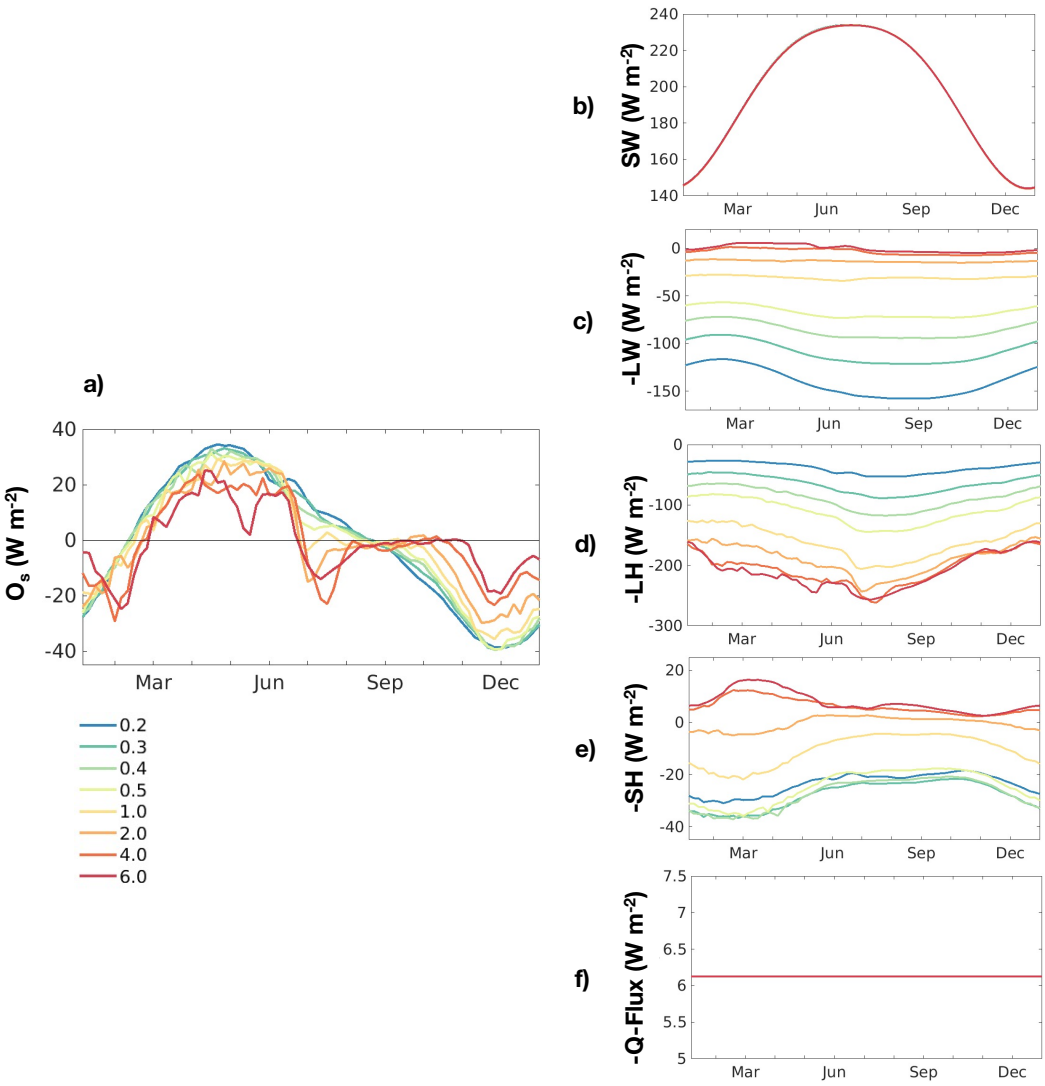

Figure 3.17: The seasonal cycles of the tropical mean ocean energy storage O_s (a) and the terms in the surface energy budget (Eq. (3.6)): shortwave flux to the surface (b), longwave flux out of the surface (c), surface latent heat flux out of the surface (d), surface sensible heat flux out of the surface (e), and ocean Q flux (f). Note the different y-axis ranges of each plot.

latent energy storage is due to the earlier change in sign of the surface temperature tendency (Fig. 3.16c). The time tendency of the surface temperature is determined by the surface energy budget, which follows:

$$c\rho d\frac{\partial T_s}{\partial t} = O_s = S^s - L^s - LH - SH - \nabla \cdot F_0, \tag{3.6}$$

with ocean heat storage O_s on the left hand side, with water specific heat c, density ρ, and MLD d, being balanced by radiative and turbulent energy fluxes into the surface (with net incoming shortwave (SW) flux S^s, net outgoing longwave (LW) flux L^s, outgoing sensible and latent heat fluxes, respectively SH and LH) and any energy flux convergence by ocean currents ($-\nabla \cdot F_0$, also known as Q flux). The NH tropical mean seasonal cycles of the ocean heat storage is plotted in Fig. 3.17a. In agreement with Eq. (3.6), the seasonality of O_s is proportional to the seasonality of $\partial T_s/\partial t$ (Fig. 3.16c). The terms in the surface energy budget are also plotted to reveal what might cause an earlier decrease and change in sign in the $O_s \propto \partial T_s/\partial t$. Since we do not vary the insolation cycle between the simulations, the SW cycle is the same for all the climates (Fig. 3.17b). This is also true for the ocean Q flux, where we used the same time invariant distribution, resulting in an equal and constant value in time for all the climates (Fig. 3.17f). Between the climates, the main differences in the surface energy budget arise from changes in the outgoing LW, surface LH, and surface SH fluxes.

Starting with the coldest climates, the main surface energy balance is between the incoming SW and outgoing LW fluxes. The LW flux approximately follows the insolation cycle, with an inherent phase lag due to the heat capacity of the ocean surface, which is dependent on the MLD $d = 5$ that was selected and used for all the simulations (Fig. 3.17c). The LW flux has more seasonality in the colder climates since the colder climates have smaller prescribed atmospheric optical depth and less atmospheric moisture, due to colder temperatures. Therefore, in these climates the surface is able to radiate away more energy in the net LW and respond to temperature changes. Relative to the outgoing LW flux, the surface LH and SH fluxes are much smaller in magnitude (Fig. 3.17d, e), and are likely due to colder temperatures and smaller magnitudes of surface winds (Fig. 3.8). Both the LH and SH fluxes are coming out of surface and into the atmosphere.

As the climate warms, we observe a change in the dominant terms in the surface energy balance. The main energy balance is between the incoming SW and surface LH flux. Due to higher prescribed atmospheric optical depths and increased atmospheric temperatures, the outgoing LW flux is reduced to nearly zero (Fig. 3.17c).

This means that as the climate continues to warm, at extreme temperatures the surface is unable to get rid of heat through the LW flux as too much LW is being radiated back down to the surface, resulting in an almost negligible net LW flux (e.g., O'Gorman & Schneider, 2008). Instead, as the climate warms, the surface LH flux increases to make up for the decrease in LW flux. Not only do we observe an overall increase in magnitude of the surface LH flux as the climate warms, but we especially notice a rapid intensification of the surface LH flux near the beginning of July (Fig. 3.17d). This peak matches well with the shape and timing of when the O_s and $\partial T_s/\partial t$ curves change sign from positive to negative (June to July transition in Figs. 3.17a and 3.16c). This result suggests that as the climate warms to extremely warm temperatures, the summertime tropical surface temperature tendency may switch to negative earlier in the season due to large increases in surface LH flux. The surface SH flux also shows interesting changes with warming. Within climates warmer than the current climate, we observe that the SH flux changes direction, and fluxes energy from the atmosphere to the surface (O'Gorman & Schneider, 2008). This occurs because the near-surface atmospheric temperatures in the tropics increase so much that the they exceed the surface temperatures and instead flux energy to the surface. However, as the climate warms, the magnitudes of changes in the surface SH flux are small compared to the changes in the surface LH fluxes.

The analysis of the surface energy budget reveals interesting changes that occur as the climate warms. In particular, the insolation cycle switches from being balanced mainly by the outgoing LW flux in colder climates, to being balanced mostly by the surface LH flux as the climate warms. These changes with a warming climate, especially as the climate warms to extreme temperatures, result in the surface temperature tendency, and with it the latent energy and MSE storage, to decrease and change sign to negative earlier in the summer season. As a result, how long the compensating effect of the MSE storage is active is limited and the mean circulation transport needs to respond to the net thermal forcing without much delay between the warmest climates.

3.6 Discussion and Conclusion

Connecting the AM and Energetic Frameworks

In this study, we aim to investigate the monotonic monsoon onset delay projected with global warming within the CMIP5 and CMIP6 model suites (Song et al., 2018; Song et al., 2021) by using an extensive set of idealized aquaplanet simulations that cover an extreme range of climates, ranging from much colder to much warmer than

the current climate. We found that by simply varying the climate by varying the atmospheric optical depth, striking changes occur within the monsoonal precipitation onset timing and spatial distribution. Across our simulations, with warming we saw a significant delay in the monsoon onset timing and we observed changes in the double-peaked structure and poleward extents of the tropical precipitation. We tried to explain these changes using two main approaches, one rooted in the circulation dynamics, and the other based on energetic arguments. Can these two arguments be connected and do they support each other?

Focusing on the circulation and using the AM budget, we observed that the same delay in monsoon onset timing with warming was observed within the timing of the tropical circulation's transition from a dynamical regime heavily influenced by extratropical eddies to a monsoon regime where the flow was more AMC and directed by energetic constraints. We observed that within colder climates, the ascending branch of the circulation, and with it the ITCZ, jumped across the equator into the the NH hemisphere earlier in the season at the start of NH summer, initiating the dynamical feedbacks earlier in the season that allow for the tropical circulation to approach a more AMC dynamical regime that allows for the circulation to grow rapidly in strength and poleward extent. In contrast, within warmer climates, the seasonal transitions of the ITCZ were delayed, and as a result the tropical circulation reached the monsoon AMC dynamical regime later in the season.

From the energetic perspective, as the climate warms, NH spring temperatures increase faster than during NH summer, causing a LH demand in the NH during NH spring, and as a result, holding back the ascending branch of the tropical circulation in the SH, and with it the ITCZ, in order to transport more energy into the NH to keep up with the LH demand — overall resulting in a monsoon onset delay. This can be observed within the anomalous circulation created when comparing the current climate with the next colder ($\alpha = 0.5$) and next warmer ($\alpha = 2.0$) climates (Fig. 3.18). As the climate warms, relative to the next colder climate (compare $\Psi_{1.0} - \Psi_{0.5}$ and $\Psi_{2.0} - \Psi_{1.0}$), an anomalous circulation forms during May 1 and June 1 with the ascending branch located in the SH, which transports energy into the NH. Only by July, is the anomalous circulation in the upper branch centered in the NH and transports energy into the winter hemisphere. In other words, as the climate warms, the insolation changes do not need to immediately be compensated by circulation changes since some of the changes are instead compensated by changes in the system's thermodynamics through changes in the LH tendency (Figs. 3.14

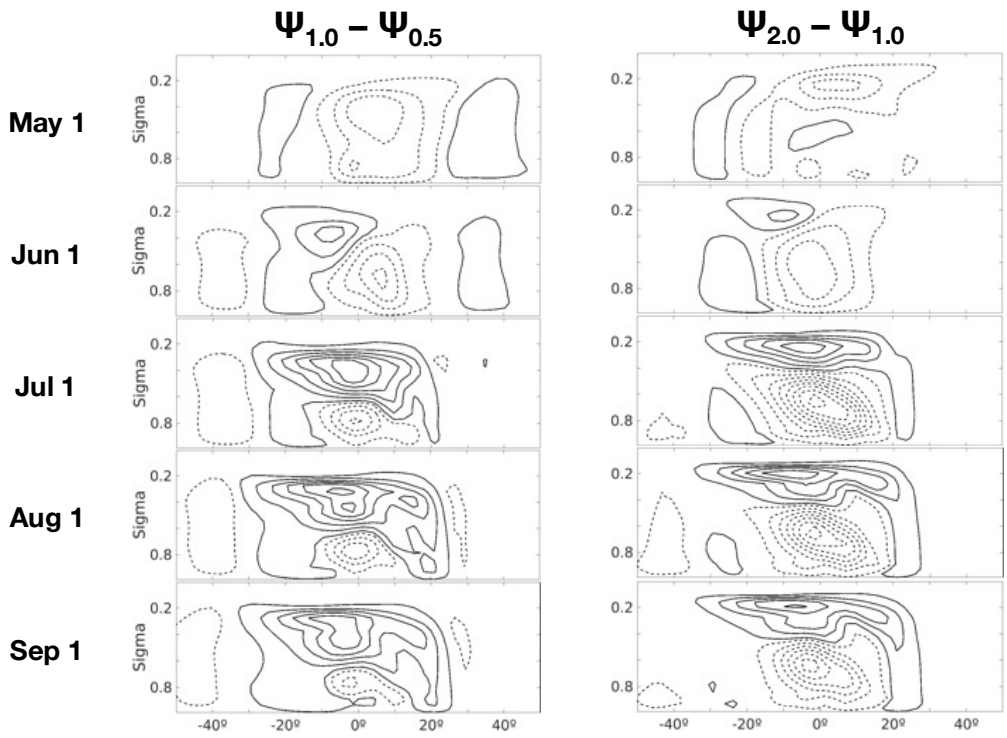

Figure 3.18: The anomalous streamfunctions during the first pentad of each month from May to September (top to bottom) from comparing the current climate to the $\alpha = 0.5$ climate (left column) and comparing the $\alpha = 2.0$ climate to the current climate (right column). The same contour styles and interval are used as in Fig. 3.6.

and 3.16a).

The two frameworks can be connected by understanding the seasonal migration of the ITCZ. Previous work has shown that having regions of low thermal inertia in the lower boundary within the tropical latitudes is necessary for monsoon transitions to occur on rapid intraseasonal timescales (Bordoni & Schneider, 2008; Hui & Bordoni, 2021). This is because the lower thermal inertia of the lower boundary helps the ascending branch of the circulation, and with it the ITCZ, jump across the equator and start its poleward migration earlier in the season. As the ITCZ moves further poleward, dynamical feedbacks are initiated that further help the circulation move increasingly towards the monsoon dynamical regime, where the flow is more AMC and the circulation can increasingly move further poleward and strengthen quickly (Bordoni & Schneider, 2008). In this study, within our simulated colder climates, due to the Clausius-Clapeyron relationship, there is less moisture within the atmosphere and therefore the thermal inertia is lower. Because the colder atmosphere does not have as much capacity to uptake moisture, changes in the

insolation forcing must be immediately compensated by changes in the circulation. In contrast, within our simulated warmer climates, the saturation vapor pressure is much higher and the atmosphere can hold much more moisture, increasing the atmosphere's thermal inertia. In these warmer climates, the circulation responds to changes in the insolation forcing with a delay since some of these changes are also compensated by thermodynamical changes due to changes in the atmospheric moisture. This can be clearly observed in the decomposition of the MSE budget in Figs. 3.11 and 3.12. In the warmer climates, as the storage term increases more in the NH spring, it balances the thermal forcing (F_{net}). Only during the summer when the storage decreases does the circulation need to respond to the F_{net} (note the timing of rapid increase in mean energy flux divergence). Once the circulation responds and the ITCZ is able to move further off the equator with the associated circulation becoming broad and cross-equatorial, the influence of the eddies are reduced and the flow approaches the more AMC monsoon regime (Figs. 3.9 and 3.12). The results are delayed, yet still rapid, circulation transitions and associated monsoon onsets with warming.

Connection Between the Seasonality of the Surface Temperature Tendency and Energy Storage

Our additional analysis described at the end of Section 3.5 adds to the original proposed mechanism by Song et al. (2018) and highlights the importance of the connection between the seasonal cycles of the energy storage and surface temperature tendency. While increased energy storage due to increases in latent energy storage with warming predicts well the monsoon onset delay, it is also important to carefully consider the full seasonal cycle of the energy storage. As the climate warms to extreme temperatures, due to complicated seasonal changes in the surface energy balance, the surface temperature tendency can cause unexpected changes to the seasonal cycle of the energy storage. In our case, we observed that in extremely warm climates, although storage increased significantly, it also decreased earlier in the season due to earlier decreases in surface temperature tendency. As a result, within the warmest climates, we did not observe any relative monsoon onset delay.

Diving deeper into understanding the unexpected changes in LW, surface LH, and surface SH fluxes is beyond the scope of this study and are left for future work. Recent work has explored the complex relationship between the LW, surface LH, and surface SH fluxes with warming using the Penman-Monteith equation (Siler et al., 2019). This new framework allows the change in ocean evaporation to

be partitioned into a thermodynamic response to surface warming and additional diagnostic contributions from changes in individual surface variables, such as the surface radiation, BL dynamics and relative humidity, and ocean heat uptake. A future analysis of our idealized aquaplanet climate change simulations using this new approach could shed light on the interesting changes in the surface energy balance and the dominance of the surface LH flux term with extreme warming.

Model Advantages and Limitations

The choice of idealized model was advantageous for this study as it allowed us to simulate a large range of extreme climates, both warmer and colder than the current climate, without the need to perform very long simulations. The idealized simulations were successful in capturing the monotonic delaying trend in the monsoon onset with climate warming, and due to their idealized configurations and physics, allowed certain trends in the precipitation and circulation changes and changes in the atmospheric energy budget to be clearly observed and studied. The results from this study suggest a few interesting questions left for future work. While this study focused on the mechanisms responsible for delayed monsoon onset with warming, it would be interesting to look more closely at the nonlinear effects on the dynamics and thermodynamics of the atmosphere that arise when studying such a large range of extreme climates. For example, the effects of this nonlinearity were observed in the "saturating" onset delay effect observed in the warmest climates presented here. However, further work in this direction could help expand our understanding of the tropical circulation and precipitation in paleoclimate or could inform us on possible future changes.

Also, while using the idealized model can make certain mechanisms more clearly observed, the idealized configuration and physics also neglect several mechanisms and feedbacks that play important roles in the real world. Our idealized simulations showed that with climate warming, changes in the energy storage due to latent energy storage changes drove the changes in the divergence of AHT. However, the current model configuration was set up with a uniform MLD, uniform albedo, and unlimited surface evaporation, all of which can have significant impacts on the atmospheric energy budget and moisture supply through one or both the F_{net} and $\partial\langle\mathscr{E}\rangle/\partial t$ terms. It will be important for future work to explore the effects of more realistic representations of these aspects to determine how they might influence the atmospheric energy budget. For example, if the surface evaporation were limited, as occurs over some tropical land regions in the real world, the compensation of the

circulation changes by latent energy changes in the atmosphere may be reduced and the monsoon onset delay may be lessened. Land-ocean moisture and temperature contrast and land-ocean moisture advection can also significantly impact the F_{net} and $\partial\langle\mathscr{E}\rangle/\partial t$ terms in magnitude and seasonality, to influence the effectiveness of the mechanism demonstrated in this idealized work. Also, the model does not represent clouds, which also have important radiative effects and can greatly influence the atmospheric energy budget through the F_{net} term, as well as terms in the surface energy budget, which we demonstrated can strongly impact the seasonality of the latent energy storage. Detailed studies of each of these effects within intermediate GCMs would help bridge the gap between such idealized work as described in this paper and comprehensive GCMs. These studies will be necessary to gain better understanding of the actual role the physical mechanisms explored in this idealized study play in individual monsoon regions observed in the real world.

Chapter 4

CONCLUSION

4.1 Thesis Summary and Concluding Remarks

Despite the potentially devastating socio-economic impacts, the future response of the monsoon to climate change remains poorly understood. Although there is consensus on global zonal mean tropical changes with climate warming, there is still a need for improved understanding and constraining of future projections of the monsoon spatial extent and onset timing, especially at the regional scale, which will be critical for informing planning that affects large populations. The work presented in this thesis aims to investigate the influence of continent on the monsoon under the current climate and the influence of climate change, under an extremely large range, with the goals to inform us on potential monsoon changes with climate warming in different regions. Using the same idealized aquaplanet GCM, we use different model setups to study the individual roles of continent and climate change on the monsoon.

In Chapter 2, we focus on studying the influence of continent on the monsoon under the current climate. Using an idealized aquaplanet GCM where land and ocean only differ by MLD, we run simulations with different configurations of zonally-symmetric NH land extending from the North Pole and vary the hemispheric asymmetry in the surface thermal inertia by varying the latitude of the southern coastal boundary. Using the AM budget framework, we show that having regions of land extending into the tropical latitudes is necessary to generate circulations with the rapid onset and gradual retreat similar to observed monsoons. Having tropical regions of low thermal inertia enables the circulation to transition rapidly earlier in the season from an eddy-mediated regime to a monsoon regime where the flow is more AMC. Once the flow has reached the monsoon regime, due to dynamical feedbacks, the cross-equatorial Hadley cell is able to grow rapidly in strength and poleward extent. In the absence of tropical land, the circulation transitions are smoother and are unable to extend as far poleward, and altogether are less “monsoon-like". In summary, the important influence continent has on the monsoon under the current climate is in helping the circulation’s ability to make the dynamical regime switch to the monsoon regime on a rapid intraseasonal timescale.

Our results from Chapter 2 have helped advance fundamental understanding of the dynamical regime transition with the inclusion of continent and recognize connections between simulated and observed monsoons. Our idealized work, along with other recent idealized studies, has led to the novel perspective that the regime transition can be roughly associated with a tropical latitude in both idealized and observed monsoons (Geen et al., 2019; Hui & Bordoni, 2021). That is to say that if the ITCZ lies equatorward of this latitude the flow is within the eddy-mediated "ITCZ regime", whereas if the ITCZ lies poleward of this latitude, the flow will transition into the more AMC "monsoon regime". We also observe this behavior in our idealized work in Chapter 3. More details of our work and related idealized monsoon studies and their contributions to improved understanding in the context of the observed global and regional monsoons are reviewed in Geen et al. (2020).

In Chapter 3, we explore the role of climate change on the monsoon. Using the same idealized aquaplanet GCM, instead we prescribe a uniform global MLD, and vary the climates by varying the atmospheric optical depth. We take advantage of our idealized model and run a set of simulations spanning a large range of climates, from much colder to much warmer than the current climate to additionally explore any interesting effects of the highly nonlinear relationship between temperature and moisture on the monsoon. Even without the presence of land-sea asymmetries, our idealized simulations show a monsoon onset delay with warming, consistent with results from the CMIP5 and CMIP6 archives (Biasutti & Sobel, 2009; Dwyer et al., 2014; Song et al., 2018; Song et al., 2021). Through the AM budget, we find evidence of the onset delay in the changes of the timing in the dynamical regime switch from the eddy-driven regime to the monsoon AMC regime. Motivated by the mechanism proposed by Song et al. (2018), we analyze the interseasonal changes in the terms of the atmospheric energy budget and demonstrate that the monsoon onset delay with warming is due to increases in the springtime atmospheric energy storage, which is strongly linked to the seasonal cycle of the surface temperature tendency within each climate and remains consistent with the results in (Song et al., 2018). This increase in storage helps compensate changes in the net thermal forcing, which allow the tropical circulation to respond to the thermal forcing later in the season.

Interestingly, we find that within our warmest simulated climates, the monsoon onset delay effect saturates, resulting in no relative onset delay between our warmest three climates. Extending our analysis of the MSE budget, we show that a closer look at

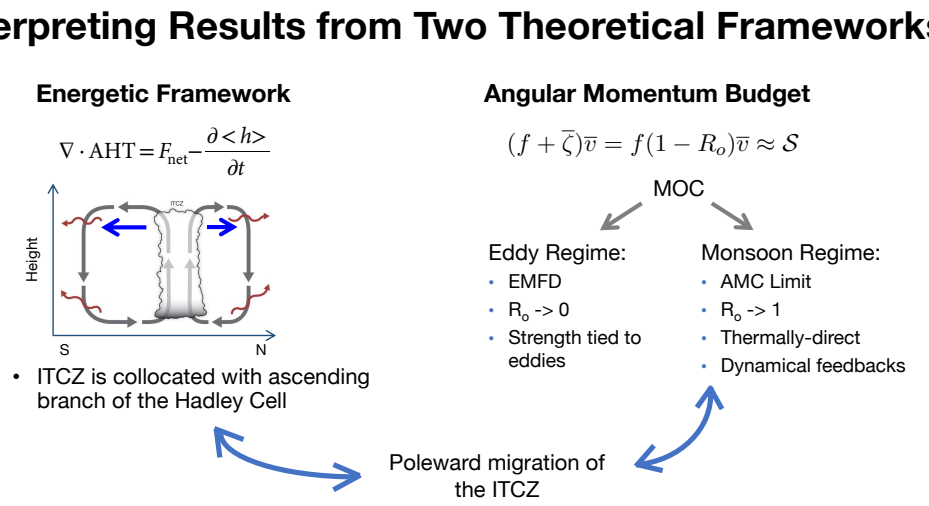

Figure 4.1: Schematic summarizing the two main theoretical frameworks the analyses of this thesis centers around.

the full seasonal cycle of the energy storage is necessary. Especially in extremely warm climates, where the storage term increases significantly and plays an important role in the MSE budget, we find that due to complex changes in the seasonality of the surface temperature, although the storage increases significantly in the spring, it also decreases earlier in the summer. As a result, how long the larger storage can compensate the thermal forcing in the season is limited, and hence the monsoon onset delays no further. In summary, a warmer climate has the most potential to affect the monsoon through increases in atmospheric energy storage that can affect the onset timing. Springtime increases in energy storage predict well longer monsoon onset delay, however as we approach extremely warm temperatures, the full seasonal cycle of the storage needs to be more carefully considered to predict onset timing changes. More specifically, for extremely warm climates, the insolation cycle switches from being balanced mainly by the outgoing LW flux in colder climates, to being balanced mostly by the surface LH flux, suggesting an increasing role of surface LH flux in determining the surface temperature tendency and hence, the onset delay.

Throughout both studies, our analyses focus on using both the AM budget and MSE budget frameworks. The former helps analyze changes in the circulation to identify monsoon onset timing as the dynamical regime transition from an eddy-mediated regime to a more AMC monsoon regime. The latter, on the other hand, helps us understand the location and seasonal migration of the circulation ascending branch and with it the ITCZ. Our work shows that the while a lot can be learned from each

framework, putting the two together gives a fuller picture. We demonstrated that using the energetic framework could help us diagnose changes in the ITCZ seasonal migration through changes in the atmospheric energy budget. Using the AM budget, we were able to determine whether circulations reached monsoon regimes and why they were able to have rapid seasonal transitions. We found that the two frameworks can be connected by the poleward excursion of the ITCZ. A schematic describing the two theoretical frameworks and putting them into context with each other is provided in Fig. 4.1. Within our simulations, the energetic framework helped us understand the position of the ITCZ throughout the season. Once the ITCZ was able to move far enough off the equator due to changes in the atmospheric energy balance, dynamical feedbacks were initiated that allowed for rapid seasonal migrations of the ITCZ due to the dynamical regime switch, as understood from the AM budget. In Chapter 2, we saw that only in simulations with regions of low surface thermal inertia extending deep enough into the tropical latitudes, was the ITCZ able to move further poleward and initiate dynamical feedbacks to help bring the ciruclation into a monsoon AMC regime. Without the regions of tropical land, the ITCZ was not able to move far enough poleward to initiate the feedbacks, and the circulation did not ever achieve as AMC of a flow. Similarly, in Chapter 3, monsoon onset only occurred in all the climates when the ITCZ was able to move far enough off the equator. With warming, due to the compensating effect of the latent energy storage in the spring, the circulation's response to thermal forcing was delayed. However, due to the low enough MLD used, with the appropriate changes in the atmospheric energy balance, the ITCZ was eventually able to move further poleward. Even if delayed in warmer climates, once the circulation was able to move far enough poleward, we still observed rapid monsoon onset and the circulations still all achieved a more AMC flow, unlike in our more "ocean-like" simulations in Chapter 2. In this way, the two frameworks can complement each other in analysis to explain not only when and where the monsoon onset and precipitation will occur, but also why in some cases the rapid monsoonal circulation transitions and why not in others.

4.2 Motivation for Future Work

The results from both parts of this thesis highlight the important role the surface, both in its physical conditions and energy balance, has on setting the monsoon. First, we demonstrate that simple changes in the physical conditions of the surface, in our case the surface thermal inertia (Chapter 2), can have large impacts on the tropical circulation's ability to transition rapidly into the dynamical monsoon regime. Our

10° simulation in Chapter 2 (Hui & Bordoni, 2021) can be considered a good analog for the South Asian Monsoon (SAM): in addition to land extending polewards from low latitudes over a large longitudinal range in the NH and ocean in the southern hemisphere, MLDs over the Indian Ocean north of 10-15° do not exceed 10 m in May just before monsoon onset (Walker, 2017). A quick comparison of the precipitation seasonal cycle from our simulation with the 10° continent (top right panel of Fig. 2.2) with that from the SAM region from GPCP daily precipitation data (top panel of Fig. 1.2) illustrates that even in such a highly idealized model, a quite realistic circulation can be simulated by just varying the surface heat capacity in a similar way. It is striking that a simple zonally symmetric continent with equatorward boundary confined within 20 degrees of the equator produces a monsoon with a rapid onset and gradual retreat similar to what is observed in the SAM region (Fig. 1.2).

Our second study (Chapter 3) highlights the important influence of the surface through the impact the surface temperature seasonality can have on the energy storage, which can potentially affect monsoon onset timing by helping compensate the change in the net thermal forcing and allowing the circulation to respond to the thermal forcing later in the season. As we think about how this idealized work can be extended to inform us on future changes in observed monsoons, it is important to consider the many factors that could potentially influence the surface temperature seasonality. Recalling Eq. (2.1), these factors could include: changes in the surface heat capacity through changes equivalent to changing the MLD or specific heat capacity, and changes in any of the other fluxes — the SW, LW, LH, SH, and ocean Q flux. SW flux can be affected by changes in clouds or albedo (Byrne & Zanna, 2020), which are not represented (clouds) or kept constant and uniform (albedo) within our idealized model, but surely will play an important role in the real-world. Changes in the LW flux are likely difficult to predict due to the complex relationship between temperature and moisture, not to mention also any interesting radiative changes that may arise from cloud changes. Our results demonstrate that future changes in the surface LH and SH fluxes are also not straightforward, and suggest a complex relationship between future LW flux and surface LH flux changes. Our model uses a zonally-symmetric time invariant ocean Q flux configuration. In reality, the ocean heat transport has its own seasonal cycle and may also change with future changes in the ocean circulation. Additionally, our aquaplanet model simplifies our setup by using a fully saturated lower boundary. The strong relationship between the surface temperature and energy storage seasonal cycles that we find in our

Table 4.1: Simulations run combining the effects of idealized continent and climate change. The onset and retreat metrics following WB16 are listed.

Simulations			
Southern Boundary	α	Onset	Retreat
10°	0.5	16 May	16 Oct
10°	0.7	16 May	16 Oct
10°	1.0	11 May	16 Oct
10°	2.0	11 May	21 Oct
10°	4.0	16 May	1 Nov
30°	0.5	1 Jun	6 Oct
30°	0.7	11 Jun	21 Oct
30°	1.0	11 Jun	11 Oct
30°	2.0	21 Jun	16 Oct
30°	4.0	21 Jun	11 Oct

simulations is dependent of the infinite moisture supply from the surface, since most of the increases in energy storage with surface temperature tendency are due to the latent energy storage increases. How well this mechanism for onset delay with warming works in the real world monsoons will need to be explored in settings where the surface moisture is limited or has its own seasonal cycle. Many of the proposed changes above are not so intuitive and may evolve with future climate warming in unexpected ways. In future work studying projected changes in the monsoonal precipitation timing and location with warming, it will be important to consider all these complicated changes in both the surface conditions and surface energy budget, as well as their interaction.

Indeed, some preliminary analysis demonstrates the complexity of understanding future monsoon changes even in an idealized setup. Using the same idealized aquaplanet model described in Sections 2.3 and 3.3, a few simulations combining the effects of both different idealized NH continent and both colder and warmer climates than the current climate were run and explored as motivation for future work. The same MLDs were used for ocean and land, as in Hui and Bordoni (2021), and the continent and climates are varied in a similar fashion, by varying the southern boundary latitude of the land and by multiplying the longwave atmospheric optical depth by the coefficient α.

The latitude of the southern coastal boundaries and optical depth coefficients used, as well as their calculated monsoon onset and retreat metrics (WB16), are shown

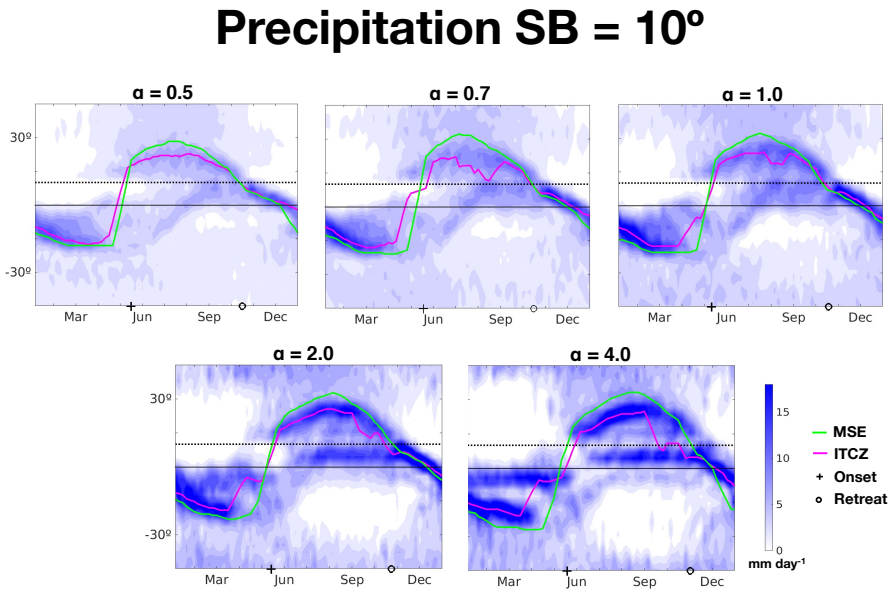

Figure 4.2: Seasonal cycles from simulations with southern boundary of land at 10° (marked by the dotted line). Color contours indicate precipitation (contour interval: 1.5 mm day^{-1}). The maximum in precipitation (green) and low-level (σ = 0.887) MSE (magenta) are marked. Both lines have been smoothed by calculating the moving mean over a sliding window of five pentads centered around the current pentad. The black plus signs and the black circles indicate monsoon onset and retreat as calculated in Walker and Bordoni (2016) and shown in Table 4.1.

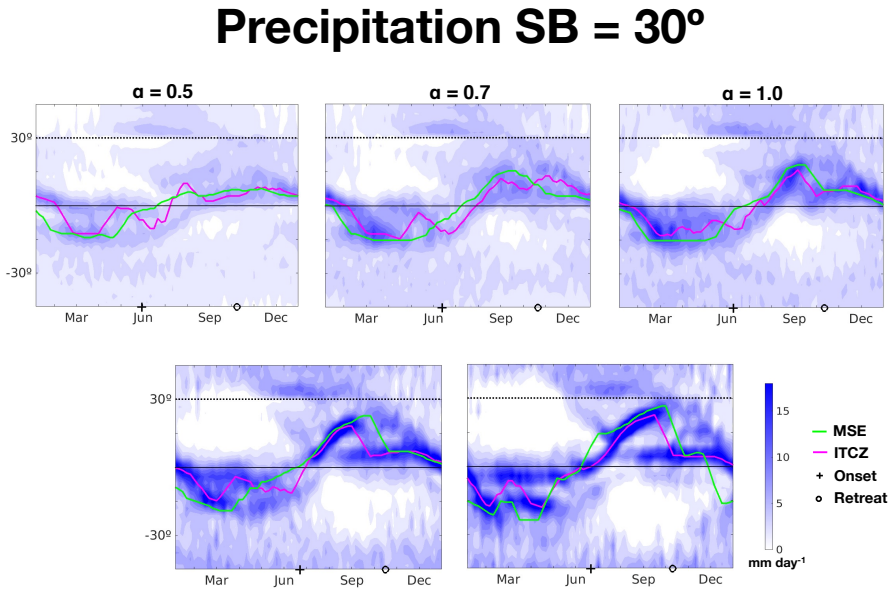

Figure 4.3: Seasonal cycles, as in Fig. 4.2, for simulations with southern boundary of land at 30° (marked by the dotted line).

in Table 4.1. The corresponding precipitation cycles from the simulations with the 10° continent (Fig. 4.2) and the 30° continent (Fig. 4.3) are also shown. In both continental configurations, as the climate warms, an overall increase in precipitation is observed everywhere. Also, within each climate, the simulation with the 10° continent always has a relatively more rapid seasonal transition and earlier monsoon onset than the corresponding simulation with the 30° continent. Additionally, as the climate warms the poleward extent of the summertime excursion of the ITCZ increases, particularly so in the simulations with the 30° continent. In fact, qualitatively, the precipitation seasonal cycles from the simulations with the 30° continent appear to be more affected by a warming climate than those with the 10° continent. This is also observed in the changes in monsoon onset timing with warming. In the simulations with the 10° continent, as the climate warms from colder than the current climate to warmer, we observe little change in the monsoon onset timing. On the other hand, in the simulations with the 30° continent, the monsoon onset delays from the coldest climate (α = 0.5) to the warmest climate (α = 4.0) by three weeks. In both continental configurations little change is observed in the retreat timing. A preliminary analysis of the seasonal cycles of the terms in the upper-level momentum budget (not provided here, but similar to the analysis in Figs. 2.9 and 3.9) shows little changes with climate warming among the 10° simulations. However, for the 30° simulations, it appears that as the climate warms, although the monsoon onset delays, the circulations are able to reach a more AMC monsoon dynamical regime. Indeed, within the precipitation seasonal cycles in Fig. 4.3, although a later cross-equatorial transition occurs as the climate warms, the ITCZ moves more rapidly off the equator and the moisture flux convergence appears to be much stronger driven by a broader cross-equatorial cell compared to within the colder climates. These preliminary results could suggest that as the climate warms, even regions with land further from the tropics may experience more monsoon-like seasonal transitions of the tropical circulation and precipitation over the tropical ocean, although relatively delayed and with shorter duration compared to regions with land extending further into the tropics. It will be interesting in future work to investigate further the changes in the monsoon with warming, and especially to examine the associated changes in the MSE budget to try to connect these changes with the dynamical changes we have described.

Studying the response of the monsoon to climate warming within individual monsoon regions is also complicated within comprehensive models. A preliminary analysis of the SAM region within CMIP6 (Eyring et al., 2016) gives varying results

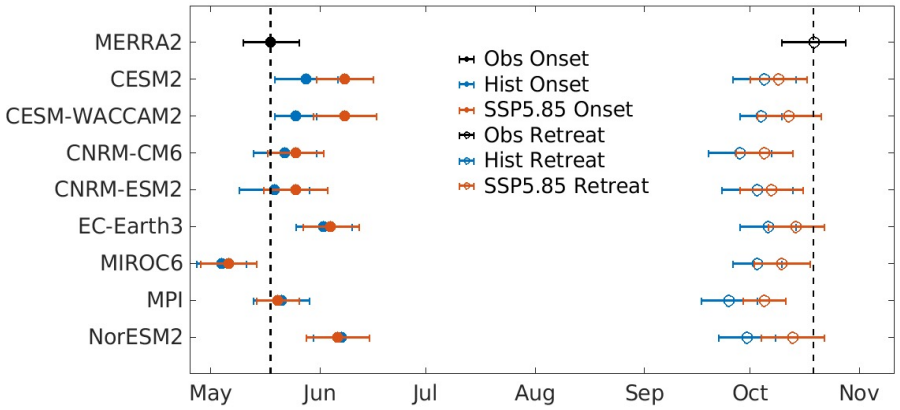

Figure 4.4: A comparison of the calculated monsoon onset (filled circles) and retreat (open circles) within the South Asian monsoon region from eight models from the CMIP6 archive and MERRA-2 (black) observations. The onset and retreat are calculated using the same metric based on the cumulative moisture flux convergence (WB16). The CMIP6 results include results from 15 historical years (2000-2014) (blue) and 15 future years from the SSP5-8.5 scenario (2086-2100) (red).

Table 4.2: The calculated shifts in monsoon onset, retreat, and season length between 15 future years from the SSP5-8.5 warming scenario and 15 historical years (2000-2014) from eight models from the CMIP6 archive.

Model	Onset Shift	Retreat Shift	Length Change
CESM2	11	4	-7
CESM-WACCAM	14	8	-6
CNRM-CM6	3	7	4
CNRM-ESM2	6	4	-2
EC-Earth3	2	8	6
MIROC6	2	7	5
MPI	-1	10	11
NorESM2	-1	13	14

in onset and retreat timing and their changes with warming (Fig. 4.4 and Table 4.2). We compare the calculated onset and retreat metrics from eight models between 15 historical years (2000-2014) and 15 future years from the SSP5-8.5 warming scenario (2086-2100). One advantage of our monsoon onset metric is that we also can calculate the retreat, so in addition to calculating shifts in the onset and retreat timing with warming, we also calculate changes in the monsoon season length. Most of the models project an onset delay with warming in the SAM region. The projected changes in the monsoon retreat and season length are more varied though.

While the results differ, it would be interesting to analyze the changes in the MSE budget with warming within each model. Perhaps differences in the change in the energy storage during the spring could help explain the model spread in the results.

Although highly idealized, our work contributes to deepening our fundamental understanding of the underlying mechanisms that set the monsoon in the current climate and the future response to climate warming. Our work highlights the importance of a careful consideration of the surface, in both its physical conditions and energy balance. Our work especially emphasizes the impact of not only the increase in magnitude, but also the changes in the seasonality of the atmospheric energy storage, on the shifts in timing of the future monsoon. Our improved understanding of this mechanism informs future analysis of the monsoon in both idealized and comprehensive cases, to focus on the seasonal changes in both the total and surface energy budgets. Expanding the model hierarchy to add more real-world features to idealized models one at a time will prove helpful in furthering our understanding of the diverse monsoon systems in the real world and how they respond to global warming.

BIBLIOGRAPHY

Adam, O., Bischoff, T., & T. Schneider, 2. (2016). Seasonal and interannual variations of the energy flux equator and ITCZ. Part II: Zonally varying shifts of the ITCZ. *J. Climate*, *29*, 7281–7293.

Adler, R. F., Huffman, G. J., Chang, A., Ferraro, R., Xie, P.-P., Janowiak, J., Rudolf, B., Schneider, U., Curtis, S., Bolvin, D., Gruber, A., Susskind, J., Arkin, P., & Nelkin, E. (2003). The version-2 global precipitation climatology project (gpcp) monthly precipitation analysis (1979–present). *Journal of Hydrometeorology*, *4*(6), 1147–1167. https://doi.org/10.1175/1525-7541(2003)004<1147:TVGPCP>2.0.CO;2

Biasutti, M., & Sobel, A. H. (2009). Delayed Sahel rainfall and global seasonal cycle in a warmer climate. *Geophys. Res. Lett.*, *36*(23).

Biasutti, M., Voight, A., Boos, W. R., Braconnot, P., Hargreaves, J. C., Harrison, S. P., Kang, S. M., Mapes, B., Scheff, J., Schumacher, C., Sobel, A. H., & Xie, S. P. (2018). Global energetics and local physics as drivers of past, present and future monsoons. *Nature Geoscience*, *11*, 392–400.

Bischoff, T., & Schneider, T. (2014). Energetic constraints of the position of the intertropical convergence zone. *J. Climate*, *27*, 4937–4951.

Bombardi, R., Moron, V., & Goodnight, J. (2019). Detection, variability, and predictability of monsoon onset and withdrawal dates: A review. *International Journal of Climatology*, *40*, 641–667. https://doi.org/10.1002/joc.6264

Boos, W. R., & Korty, R. L. (2016a). Regional energy budget control of the Intertropical Convergence Zone and application to mid-Holocene rainfall. *Nature Geoscience*, *9*, 892–897.

Boos, W. R., & Korty, R. L. (2016b). Regional energy budget control of the Intertropical Convergence Zone and application to mid-Holocene rainfall. *Nature Geoscience*, *9*, 892–897.

Boos, W. R., & Kuang, Z. (2010). Dominant control of the South Asian monsoon by orographic insulation versus plateau heating. *Nature*, *9*, 218–222.

Bordoni, S., & Schneider, T. (2008). Monsoons as eddy-mediated regime transitions of the tropical overturning circulation. *Nature Geoscience*, *1*, 515–519.

Byrne, M. P., & Zanna, L. (2020). Radiative effects of clouds and water vapor on an axisymmetric monsoon. *Journal of Climate*, *33*(20), 8789–8811.

Charney, J. (1969). A further note on large-scale motions in the tropics. *J. Atmos. Sci.*, *26*, 182–185.

Chou, C., & Lan, C.-W. (2012). Changes in the annual range of precipitation under global warming. *Journal of Climate*, *25*(1), 222–235.

Chou, C., Neelin, J. D., & Su, H. (2001). Ocean-atmosphere-land feedbacks in an idealized monsoon. *Quart. J. Roy. Meteor. Soc.*, *127*, 1869–1891.

Chou, C., Tu, J.-Y., & Tan, P.-H. (2007). Asymmetry of tropical precipitation change under global warming. *Geophys. Res. Lett.*, *34*(17).

Chou, C., & Neelin, J. D. (2004). Mechanisms of Global Warming Impacts on Regional Tropical Precipitation. *Journal of Climate*, *17*(13), 2688–2701. https://doi.org/10.1175/1520-0442(2004)017<2688:MOGWIO>2.0.CO;2

Collins, M., Minobe, S., Barreiro, M., Bordoni, S., Kaspi, Y., Kuwano-Yoshida, A., Keenlyside, N., Manzini, E., O'Reilly, C. H., Sutton, R., Xie, S., & Zolina, O. (2018). Challenges and opportunities for improved understanding of regional climate dynamics. *Nature Clim. Change*, *26*, 182–185.

Cook, K. H., & Gnanadesikan, A. (1991). Effects of Saturated and Dry Land Surfaces on the Tropical Circulation and Precipitation in a General Circulation Model. *Journal of Climate*, *4*(9), 873–889.

Dirmeyer, P. A. (1998). Land-sea geometry and its effect on monsoon circulations. *J. Geophys. Res.*, *103*, 11555–11572.

Dwyer, J. G., Biasutti, M., & Sobel, A. H. (2014). The effect of greenhouse gas-induced changes in SST on the annual cycle of zonal mean tropical precipitation. *Journal of Climate*, *27*, 4544–4565.

Emanuel, K. A. (1987). An air-sea interaction model of intraseasonal oscillations in the Tropics. *J. Atmos. Sci.*, *44*, 2324–2340.

Emanuel, K. A. (1995). On thermally direct circulations in moist atmospheres. *J. Atmos. Sci.*, *52*, 1529–1534.

Emanuel, K. A., Neelin, J. D., & Bretherton, C. (1994). On large-scale circulations in convecting atmospheres. *Quart. J. R. Met. Soc.*, *120*, 1111–1143.

Eyring, V., Bony, S., Meehl, G. A., Senior, C. A., Stevens, B., Stouffer, R. J., & Taylor, K. E. (2016). Overview of the coupled model intercomparison project phase 6 (cmip6) experimental design and organization. *Geoscientific Model Development*, *9*(5), 1937–1958. https://doi.org/10.5194/gmd-9-1937-2016

Flohn, H. (1957). Large-scale aspects of the summer monsoon in South and East Asia. *Journal of the Meteorological Society of Japan. Ser. II*, *35A*, 180–186. https://doi.org/10.2151/jmsj1923.35A.0_180

Frierson, D. M. W. (2007). The dynamics of idealized convection schemes and their effect on the zonally averaged tropical circulation. *J. Atmos. Sci.*, *64*, 1959–1976.

Frierson, D. M. W., Held, I. M., & Zurita-Gotor, P. (2006). A gray-radiation aqua-planet moist GCM. Part I: Static stability and eddy scales. *J. Atmos. Sci.*, *63*, 2548–2566.

Frierson, D. M. W., Hwang, Y. T., Fučkar, N., Seager, R., Kang, S. M., Donohoe, A., Maroon, E. A., Liu, X., & Battisti, D. S. (2013). Contribution of ocean overturning circulation to tropical rainfall peak in the northern hemisphere. *Nat. Geosci.*, *6*, 940–944.

Frierson, D. M. W., & Hwang, Y.-T. (2012). Extratropical influence on ITCZ shifts in slab ocean simulations of global warming. *Journal of Climate*, *25*(2), 720–733. https://doi.org/10.1175/JCLI-D-11-00116.1

Geen, R., Bordoni, S., Battisti, D. S., & Hui, K. L. (2020). Monsoons, ITCZs, and the concept of the global monsoon [e2020RG000700 10.1029/2020RG000700]. *Reviews of Geophysics*, *58*(4), e2020RG000700. https://doi.org/https://doi.org/10.1029/2020RG000700.

Geen, R., Lambert, F., & Vallis, G. (2018). Regime change behavior during Asian monsoon onset. *J. Climate*, *31*, 3327–3348.

Geen, R., Lambert, F., & Vallis, G. (2019). Processes and timescales in onset and withdrawal of "aquaplanet monsoons". *J. Climate*, *32*, 2357–2373.

Geng, Y.-F., Xie, S.-P., Zheng, X.-T., & Wang, C.-Y. (2020). Seasonal dependency of tropical precipitation change under global warming. *Journal of Climate*, *33*(18), 7897–7908.

Held, I. M. (2000). The general circulation of the atmosphere. *Program in Geophysical Fluid Dynamics*.

Held, I. M., & Hou, A. Y. (1980). Nonlinear axially symmetric circulations in a nearly inviscid atmosphere. *J. Atmos. Sci.*, *37*, 515–533.

Held, I. M., & Soden, B. J. (2006). Robust responses of the hydrological cycle to global warming. *J. Climate*, *19*(21), 5686–5699. https://doi.org/10.1175/JCLI3990.1

Hill, S. A. (2019). Theories for past and future monsoon rainfall changes. *Curr. Climate Change Reports*, *5*, 160–171.

Huang, P., Xie, S. P., Hu, K., Huang, G., & Huang, R. (2013). Patterns of the seasonal response of tropical rainfall to global warming. *Nature Geoscience*, *6*, 357–361.

Huffman, G. J., Bolvin, D. T., & Adler, R. F. (2016). Gpcp version 1.2 one-degree daily precipitation data set. https://doi.org/10.5065/D6D50K46

Hui, K. L., & Bordoni, S. (2021). Response of monsoon rainfall to changes in the latitude of the equatorward coastline of a zonally symmetric continent. *Journal of the Atmospheric Sciences*, *78*(5), 1429–1444. https://doi.org/10.1175/JAS-D-20-0110.1.

Jeevanjee, N., Hassanzadeh, P., Hill, S., & Sheshadri, A. (2017). A perspective on climate model hierarchies. *J. Adv. Model. Earth Syst.*, *9*, 1760–1771.

Kang, S. M., Frierson, D. M. W., & Held, I. M. (2009). The Tropical Response to Extratropical Thermal Forcing in an Idealized GCM: The Importance of Radiative Feedbacks and Convective Parameterization. *Journal of the Atmospheric Sciences*, *66*(9), 2812–2827. https://doi.org/10.1175/2009JAS2924.1

Kang, S. M., Frierson, D. M. W., & Zhao, M. (2008). The response of the ITCZ to extratropical thermal forcing: Idealized slab-ocean experiments with a GCM. *J. Climate*, *21*, 3521–3532.

Kang, S. M., Shin, Y., & Xie, S.-P. (2018). Extratropical forcing and tropical rainfall distribution: Energetics framework and ocean Ekman advection. *NPJ Climate and Atmos. Sci.*, *1*, 1–10.

Kaspi, Y., & Showman, A. (2015). Atmospheric dynamics of terrestrial exoplanets over a wide range of orbital and atmospheric parameters. *The Astrophysical Journal*, *804*. https://doi.org/10.1088/0004-637X/804/1/60

Kitoh, A., Endo, H., Kumar, K. K., Cavalcanti, I. F. A., Goswami, P., & Zhou, T. (2013). Monsoons in a changing world: A regional perspective in a global context. *Journal of Geophysical Research: Atmospheres*, *118*(8), 3053–3065.

Lan, C.-W., Lo, M.-H., Chen, C.-A., & Yu, J.-Y. (2019). The mechanisms behind changes in the seasonality of global precipitation found in reanalysis products and CMIP5 simulations. *Climate Dynamics*, *53*.

Laraia, A. (2015). *Observations and modeling of tropical planetary atmospheres* (Doctoral dissertation). California Institute of Technology.

Levine, X. J., & Schneider, T. (2011). Response of the Hadley circulation to climate change in an aquaplanet GCM coupled to a simple representation of ocean heat transport. *J. Atmos. Sci.*, *68*, 769–783.

Levine, X. J., & Schneider, T. (2015). Baroclinic eddies and the extent of the hadley circulation: An idealized GCM study. *Journal of the Atmospheric Sciences*, *72*(7), 2744–2761. https://doi.org/10.1175/JAS-D-14-0152.1

Lindzen, S. R., & Hou, A. Y. (1988). Hadley circulations for zonally averaged heating centered off the equator. *J. Atmos. Sci.*, *45*, 2416–2427.

Lobo, A. H., & Bordoni, S. (2020). Atmospheric dynamics of high obliquity planets. *Icarus*, *340*(115391).

Lu, J., Vecchi, G. A., & Reichler, T. (2007). Expansion of the Hadley cell under global warming. *Geophys. Res. Lett.*, *34*(6).

Lutsko, N. J., Marshall, J., & Green, B. (2019). Modulation of monsoon circulations by cross-equatorial ocean heat transport. *J. Climate*, *32*, 3471–3485.

Maroon, E. A., & Frierson, D. M. W. (2016). The impact of a continent's longitudinal extent on tropical precipitation. *Geophys. Res. Lett.*, *43*, 11921–11929.

Maroon, E. A., Frierson, D. M. W., Kang, S. M., & Scheff, J. (2016). The Precipitation Response to an Idealized Subtropical Continent. *Journal of Climate*, *29*(12), 4543–4564.

Merlis, T., Schneider, T., Bordoni, S., & Eisenman, I. (2013a). Hadley circulation response to orbital precession. Part I: Aquaplanets. *J. Climate*, *26*, 740–753.

Merlis, T., Schneider, T., Bordoni, S., & Eisenman, I. (2013b). Hadley circulation response to orbital precession. Part II: Subtropical continent. *J. Climate*, *26*, 754–771.

Molnar, P., Boos, W. R., & Battisti, D. S. (2010). Orographic controls on climate and paleoclimate of Asia: Thermal and mechanical roles for the Tibetan Plateau. *Annu. Rev. Earth Planet. Sci.*, *38*(1), 77–102. https://doi.org/{10.1146/annurev-earth-040809-152456}

Neelin, J. D. (2007). The global circulation of the atmosphere. In T. Schneider & A. Sobel (Eds.). Princeton University Press.

Neelin, J. D., Held, I. M., & Cook, K. H. (1987). Evaporation-wind feedback and low-frequency variability in the tropical atmosphere. *J. Atmos. Sci.*, *44*, 2341–2348.

Neelin, J. D., & Held, I. M. (1987). Modeling Tropical Convergence Based on the Moist Static Energy Budget. *Monthly Weather Review*, *115*(1), 3–12. https://doi.org/10.1175/1520-0493(1987)115<0003:MTCBOT>2.0.CO;2

Neelin, J. D., & Zeng, N. (2000). A quasi-equilibrium tropical circulation model—formulation. *Journal of the Atmospheric Sciences*, *57*(11), 1741–1766.

O'Gorman, P. A., Allan, R. P., Byrne, M. P., & Previdi, M. (2012). Energetic constraints on precipitation under climate change. *Surv. Geophys.*, *30*, 585–608.

O'Gorman, P. A., & Schneider, T. (2008). The hydrological cycle over a wide range of climates simulated with an idealized GCM. *J. Climate*, *21*, 3185–3832.

O'Gorman, P. A., & Schneider, T. (2009). Scaling of precipitation extremes over a wide range of climates simulated with an idealized GCM. *Journal of Climate*, *22*(21), 5676–5685. https://doi.org/10.1175/2009JCLI2701.1

Pauluis, O. (2004). Boundary layer dynamics and cross-equatorial Hadley circulation. *J. Atmos. Sci.*, *61*, 1161–1173.

Pedlosky, J. (1964). The stability of currents in the atmosphere and the ocean: Part I. *J. Atmos. Sci.*, *21*, 201–219.

Peyrillé, P., Lafore, J.-P., & Boone, A. (2016). The annual cycle of the West African monsoon in a two-dimensional model: Mechanisms of the rain-band migration. *Quarterly Journal of the Royal Meteorological Society*, *142*(696), 1473–1489. https://doi.org/10.1002/qj.2750

Plumb, R. A., & Hou, A. Y. (1992). The response of a zonally symmetric atmosphere to subtropical thermal forcing: Threshold behavior. *J. Atmos. Sci.*, *49*, 1790–1799.

Popp, M., & Lutsko, N. J. (2017). Quantifying the zonal-mean structure of tropical precipitation. *Geophys. Res. Lett.*, *44*, 9470–9478.

Privé, N. C., & Plumb, R. A. (2007a). Monsoon dynamics with interactive forcing. Part I: Axisymmetric studies. *J. Atmos. Sci.*, *64*, 1417–1430.

Schneider, T. (2006). The general circulation of the atmosphere. *Annu. Rev. Earth Planet. Sci.*, *34*, 655–688.

Schneider, T., Bischoff, T., & Haug, G. H. (2014). Migrations and dynamics of the intertropical convergence zone. *Nature*, *513*, 45–53.

Schneider, T., & Bordoni, S. (2008). Eddy-mediated regime transitions in the seasonal cycle of a Hadley circulation and implications for monsoon dynamics. *J. Atmos. Sci.*, *65*, 915–934.

Schneider, T., O'Gorman, P. A., & Levine, X. J. (2010). Water vapor and the dynamics of climate changes. *Rev. Geophys.*, *48*, 2009RG000302.

Seidel, D. J., & Randel, W. J. (2007). Recent widening of the tropical belt: Evidence from tropopause observations. *Journal of Geophysical Research: Atmospheres*, *112*(D20).

Seth, A., Rauscher, S. A., Biasutti, M., Giannini, A., Camargo, S. J., & Rojas, M. (2013). CMIP5 projected changes in the annual cycle of precipitation in monsoon regions. *J. Climate*, *26*, 7328–7351.

Siler, N., Roe, G. H., Armour, K. C., & Feldl, N. (2019). Revisitng the surface-energy-flux perspective on the sensitivity of global precipitation to climate change. *Climate Dynamics*, *52*, 3983–3995.

Song, F., Leung, L. R., & Lu, J. (2018). Seasonally dependent responses of subtropical highs and tropical rainfall to anthropogenic warming. *Nature Clim. Change*, *6*, 787–792.

Song, F., Leung, L. R., Lu, J., Dong, L., Zhou, W., Harrop, B., & Qian, Y. (2021). Emergence of seasonal delay of tropical rainfall during 1979–2019. *Nature Climate Change*, *11*(7), 605–612.

Song, F., Lu, J., Leung, L. R., & Liu, F. (2020). Contrasting phase changes of precipitation annual cycle between land and ocean under global warming [e2020GL090327 2020GL090327]. *Geophysical Research Letters*, *47*(20), e2020GL090327. https://doi.org/https://doi.org/10.1029/2020GL090327

Staten, P. W., Lu, J., Grise, K. M., Davis, S. M., & Birner, T. (2018). Re-examining tropical expansion. *Nature Clim. Change*, *8*, 768–775.

Su, H., Jiang, J., Shen, J. N. T. J., Zhai, C., Yue, Q., Wang, Z., Huang, L., Choi, Y.-S., Stephens, G. L., & Yung, Y. L. (2017). Tightening of tropical ascent and high clouds key to precipitation change in a warmer climate. *Nature Commun.*, *8*.

Voigt, A., Biasutti, M., Scheff, J., Bader, J., Bordoni, S., Codron, F., Dixon, R. D., Jonas, J., Kang, S. M., Klingaman, N. P., Leung, R., Lu, J., Mapes, B., Maroon, E. A., McDermid, S., Park, J., Roehrig, R., Rose, B. E. J., Russell, G. L., . . . Zeppetello, L. R. V. (2016). The tropical rain belts with an annual cycle and a continent model intercomparison project: TRACMIP. *J. Adv. Model. Earth Syst.*, *8*, 1868–1891.

Walker. (2017). *Seasonal and interannual variability in South Asian monsoon dynamics* (Doctoral dissertation). California Institute of Technology.

Walker, & Bordoni, S. (2016). Onset and withdrawal of the large-scale south asian monsoon: A dynamical definition using change point detection. *Geophysical Research Letters*, *43*(22), 11, 815–11, 822.

Walker, C., & Schneider, T. (2006). Eddy influences on Hadley circulations: Simulations with an idealized GCM. *J. Atmos. Sci.*, *63*, 3333–3350.

Wang, B., Yim, S. Y., Liu, J. Y. L. J., & Ha, K.-J. (2014). Future change of Asian-Australian monsoon under RCP 4.5 anthropogenic warming scenario. *Clim. Dyn.*, *42*, 83–100.

Webster, P., & Holton, J. (1982). Cross-equatorial response to middle-latitude forcing in a zonally varying basic state. *J. Atmos. Sci.*, *39*, 722–733.

Xie, S., & Saiki, N. (1999). Abrupt onset and slow seasonal evolution of summer monsoon in an idealized GCM simulation. *J. Meteor. Soc. Japan.*, *77*, 949–968.

Xie, S.-P., Deser, C., Vecchi, G. A., Ma, J., Teng, H., & Wittenberg, A. T. (2010). Global warming pattern formation: Sea surface temperature and rainfall. *Journal of Climate*, *23*(4), 966–986.

Zhou, W., & Xie, S.-P. (2018). A hierarchy of idealized monsoons in an intermediate GCM. *J. Climate*, *31*, 9021–9036.